

Adjustable nanoporous polymers based on smectic liquid crystals

Citation for published version (APA):

Mulder, D. J. (2017). *Adjustable nanoporous polymers based on smectic liquid crystals*. [Phd Thesis 1 (Research TU/e / Graduation TU/e), Mechanical Engineering]. Technische Universiteit Eindhoven.

Document status and date:

Published: 24/10/2017

Document Version:

Publisher's PDF, also known as Version of Record (includes final page, issue and volume numbers)

Please check the document version of this publication:

- A submitted manuscript is the version of the article upon submission and before peer-review. There can be important differences between the submitted version and the official published version of record. People interested in the research are advised to contact the author for the final version of the publication, or visit the DOI to the publisher's website.
- The final author version and the galley proof are versions of the publication after peer review.
- The final published version features the final layout of the paper including the volume, issue and page numbers.

[Link to publication](#)

General rights

Copyright and moral rights for the publications made accessible in the public portal are retained by the authors and/or other copyright owners and it is a condition of accessing publications that users recognise and abide by the legal requirements associated with these rights.

- Users may download and print one copy of any publication from the public portal for the purpose of private study or research.
- You may not further distribute the material or use it for any profit-making activity or commercial gain
- You may freely distribute the URL identifying the publication in the public portal.

If the publication is distributed under the terms of Article 25fa of the Dutch Copyright Act, indicated by the "Taverne" license above, please follow below link for the End User Agreement:

www.tue.nl/taverne

Take down policy

If you believe that this document breaches copyright please contact us at:

openaccess@tue.nl

providing details and we will investigate your claim.

Adjustable nanoporous polymers based on smectic liquid crystals

PROEFSCHRIFT

ter verkrijging van de graad van doctor
aan de Technische Universiteit Eindhoven,
op gezag van de Rector Magnificus, prof.dr.ir. F.P.T. Baaijens
voor een commissie aangewezen door het College voor Promoties
in het openbaar te verdedigen
op dinsdag 24 oktober 2017 om 14.00 uur

door

Dirk Jan Mulder

geboren te Littenseradiel

Dit proefschrift is goedgekeurd door de promotoren en de samenstelling van de promotiecommissie is als volgt:

voorzitter: prof.dr.ir. E.J.M. Hensen
1^e promotor: prof.dr. A.P.H.J. Schenning
2^e promotor: prof.dr. D.J. Broer
leden: prof.dr. J.P.F. Lagerwall (Université du Luxembourg)
prof.dr. J.L. Serrano (Universidad de Zaragoza)
prof.dr.ir. D.C. Nijmeijer
prof.dr. R.P. Sijbesma
adviseur: dr. G. Portale (Rijksuniversiteit Groningen)

Het onderzoek of onderwerp dat in dit proefschrift wordt beschreven is uitgevoerd in overeenstemming met de TU/e Gedragscode Wetenschapsbeoefening.

Foar Heit en Mem

A catalogue record is available from the Eindhoven University of Technology Library.

ISBN: 978-94-629-5717-6

Copyright © 2017 by Dirk Jan Mulder.

This thesis was prepared with the \LaTeX documentation system.

Cover Design: Dirk Jan Mulder

Reproduction: ProefschriftMaken || www.proefschriftmaken.nl

This research is supported by the Dutch Polymer
Institute (DPI), project number 776n.
Dutch Polymer Institute, P.O. Box 902,
5600 AX Eindhoven, The Netherlands



Contents

1	Introduction	1
1.1	Introduction	2
1.2	Nanoporous materials based on liquid crystals	4
1.2.1	Columnar and hexagonal mesophases (1D pores)	8
1.2.2	Bicontinuous and cubic mesophases (3D pores)	11
1.2.3	Smectic and lamellar mesophases (2D pores)	12
1.3	Aim and outline of this thesis	17
1.4	References	18
2	Adjustable nanoporous materials based on dynamic covalent chemistry	23
2.1	Introduction	24
2.2	Results and discussion	25
2.2.1	Synthesis and phase behavior of the monomers	25
2.2.2	Fabrication of the nanoporous LCN	26
2.2.3	Chemical post-modification	29
2.2.4	Dye adsorption and release	33
2.3	Conclusion	34
2.4	Experimental section	34
2.4.1	Materials	34
2.4.2	Characterization	35
2.4.3	Synthesis	35
2.4.4	Methods	36
2.5	References	38
2.A	Phase behavior of the pure compounds 1 and 2	41
2.B	FTIR spectra of films after the transimination reaction (<i>iii</i>)	42
3	Pyridyl-functional nanoporous LCNs based on H-bonded Heterodimers	43
3.1	Introduction	44
3.2	Results and discussion	45
3.2.1	Synthesis and thermal properties of the monomers	45

3.2.2	Preparation and characterization of LCNs	48
3.2.3	Template removal	51
3.2.4	Anhydrous proton conduction	54
3.3	Conclusion	58
3.4	Experimental section	58
3.4.1	Materials	58
3.4.2	Characterization	59
3.4.3	Synthesis	60
3.4.4	Methods	61
3.5	References	62
4	The formation of gold nanoparticles inside 2D nanoporous materials	65
4.1	Introduction	66
4.2	Results and Discussion	67
4.2.1	Infiltration of the Au precursor	67
4.2.2	Synthesis of gold nanoparticles	70
4.3	Conclusion	76
4.4	Experimental section	77
4.4.1	Materials	77
4.4.2	Characterization	77
4.4.3	Methods	78
4.5	References	78
5	Semipermeable thermal responsive liquid crystalline elastomer shells	81
5.1	Introduction	82
5.2	Results and Discussion	83
5.2.1	Synthesis and characterization of the reactive mesogenic oligo- mer	83
5.2.2	Thermo-responsive properties of free standing LCE films	85
5.2.3	Preparation of LCE shells by glass capillary microfluidics	87
5.2.4	Thermal actuation by the LCE Shells	88
5.3	Conclusion	90
5.4	Experimental section	91

5.4.1	Materials	91
5.4.2	Characterization	91
5.4.3	Synthesis	92
5.4.4	Methods	93
5.5	References	93
6	Technology assessment	95
6.1	Introduction	96
6.2	Structure and rigidity	96
6.3	Scalability and geometry	99
6.4	Conclusion	103
6.5	References	103
	Summary	105
	Acknowledgements	109
	Curriculum Vitae	111
	Publications	113

Chapter 1

Introduction

1.1 Introduction

A nanoporous material can be defined by a few key parameters; *i*) the pore size, *ii*) the pore structure, *iii*) the porosity and *iv*) the composition of the material itself. According to the International Union of Pure and Applied Chemistry (IUPAC), nanoporous materials can be divided into macroporous, mesoporous, and microporous materials having pore sizes of 50–1000 nm, 2–50 nm, and 0.2–2 nm, respectively.[1] The pore structure can be described by the geometrical tortuosity (τ_g); defined as the average length of the pores $\langle L_g \rangle$ divided by the shortest straight-line length across the medium, *i.e.* thickness of the material itself L_s , ($\tau_g = \langle L_g \rangle / L_s$).[2] Today's processing methods offer a precise control over these parameters which render them attractive for industrial applications. For instance, a well-known challenge in public health is the accessibility to potable water.[3] The growing population and the contamination of waterbodies trigger this demand, and consequently the development of, for example, nanoporous materials for water purification seems to be an answer to this problem. Yet, the field continues to expand, and polymer membranes are being developed also for other specific applications such as energy generation, industrial filtration processes, catalysis, adsorption, ion-diffusion and conduction, drug delivery, and fuel cells. Essentially, nanoporous membranes are involved in many recent technological developments. The types, dimensions, and chemical characteristics of a membrane vary largely with the final application. While biological membranes have evolved over millions of years to specifically transport species in living matter, the development of synthetic, manmade, membranes started back in 1907. The first prototypes were made of nitrocellulose.[4, 5] Since then, the field has constantly gained interest from scientists but also from industries. A more extensive historical background and early developments in the field of polymer membranes is provided by Baker.[6]

Polymer membranes can be subdivided into two main categories; dense membranes and porous membranes. The mechanism driving the transport of moieties over the membrane is consequently very different. Porous membranes are applied in micro- and ultra-filtrations where the pore size can vary from 100 nm – 10 μ m and 10 nm – 100 nm, respectively. In dense polymer membranes, there is no defined pore size, and the permeability is determined by the membrane material's chemical properties like free volume,

polarity, and the presence of charges. Consequently, the separation occurs based on the solubility and diffusivity of species through the membrane matrix. Examples of applications of dense membranes are (reverse) osmosis and gas filtration.

The scope of this thesis, and the major part of this introduction, is focused on the fabrication of nanoporous polymer materials at the boundary of porous and dense, exhibiting pore sizes of approximately 1 nm. Another important feature is the pore chemistry. The type of interaction between the membrane and the moiety to filter can be ionic, acid/base, or van der Waals. The chemistry can be tuned to either enhance or selectively prevent the diffusion of species throughout the membrane. Finally, the size selectivity and flux over porous materials can be greatly improved by controlling the pore orientation, size distribution, and tortuosity. Therefore considerable attention has been directed towards creating straight pores of controlled size. While using a top down approach (such as track etching) can be seen as an easy solution to reach such specifications; however, it becomes more challenging when aiming at pore size below 10 nm.[7]

Scientists have been developing a method based on the microphase separation of block copolymers as a tool for the fabrication of nanoporous materials.[8, 9] This method relies on the immiscibility of two polymers that are covalently bonded. The first attempts gave access to microporous polymers obtained from micro-phase separation and was published by Lee *et al.*[10] In this work, a lamellar segregated structure was designed and subsequently the porosity was obtained by oxidative decomposition of one of the copolymer blocks, resulting in a porous polymer having randomly oriented lamellar pores. Only ten years later, porous polymers possessing aligned pores were prepared.[11, 12] Since then, the field has grown impressively as has the level of control over the design of the pores using block copolymers.[13–30] For instance, an asymmetry through the thickness of the material[31] has been implemented, and even stimuli responsive pores have been developed.[9, 32, 33]

While block copolymers offer many advantages over traditional polymers, phase separation becomes a challenge when reducing the segment length of each block. In order to reduce the pore size, an elegant approach to obtain well aligned nano sized pores relies on the self-assembly of liquid crystals. Back in the early 90's, the idea of using the self-assembly of lyotropic liquid crystal was already recognized in the formation of in-

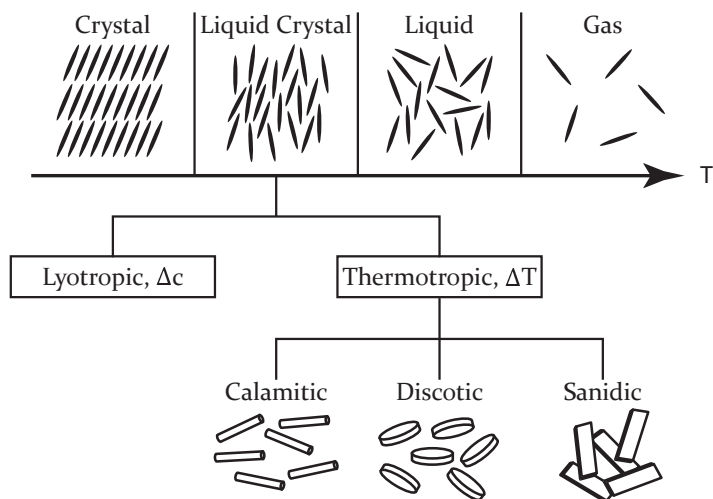


Figure 1.1: Overview of the phases of matter. Liquid crystals take their place between isotropic liquids and crystalline solids. Thermotropic phases are further classified according to the structure of the mesogen: rodlike (calamitic), disk-like (discotic), and lath-like (sanidic). Reproduced from [37] with permission of John Wiley & Sons, Inc.

organic nanoporous materials.[34–36] At the beginning of this century, many groups started to investigate the use of liquid crystals for the fabrication of nanoporous polymer membranes.

1.2 Nanoporous materials based on liquid crystals

In the liquid crystal state, molecules (mesogens) possess a degree of order that is somewhere in between the long-range positional and orientational order that is found in solid crystals and the absence of any order found in isotropic liquids, while maintaining the liquid consistency (Figure 1.1). Different types of liquid crystals have been identified; lyotropic and thermotropic liquid crystals are the best known.

Lyotropic LCs are generally amphiphilic molecules that self-assemble by the addition of a solvent. Examples of lyotropic LCs are fatty acids, phospholipids, and amphiphilic molecules in detergents. Depending on the structure of the mesogen, the temperature, and the amount of solvent added, various self-assembled geometries can be obtained, such as micelles, cubic phases, hexagonal phases, bicontinuous cubic phase, and lamellar phases. On the other hand, in thermotropic liquid crystals the mesophases are observed as an intermediate state of matter between the low temperature solid crystalline and the higher

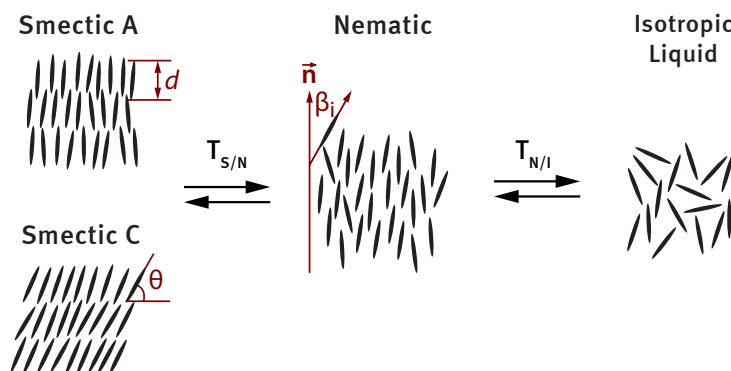


Figure 1.2: Mesophases of a calamitic liquid crystal.

temperature liquid state, by solely heating or cooling the pure compound. Thermotropic liquid crystals can further be divided in subclasses based on the anisotropic shape of the mesogen, being sanidic (lath shaped), discotic (disk shaped), and calamitic (rod shaped) (Figure 1.1).

The chemical structure of calamitic liquid crystals is often a rigid core segment consisting of multiple linearly linked aromatic rings with one or two flexible endgroups on the extremities. Cooling such a compound down from the isotropic melt, various organizations of the rod shaped mesogens can be obtained (Figure 1.2). The simplest possible organization (1D) is found in the nematic (N) mesophase, where the mesogens have an orientational order along the long axis of the molecules, having a common molecular director \vec{n} and the individual deviation from this director described by the angle β_i . Besides this order, the centers of mass of the mesogens are still distributed isotropically in 3D. Smectic A (SmA) and smectic C (SmC) mesophases can sometimes be found at temperatures below the nematic mesophase. Smectic mesophases exhibit, next to the orientational order, a positional order of the centers of mass over the long axis, resulting in the formation of layers with a discrete spacing d . In contrast to SmA, the SmC mesophase displays an additional tilt (θ) of the mesogens in the smectic layers. The tilt angle θ is strongly influenced by temperature. At the higher temperature end of the mesophase θ is close to 0° , and at the lower temperature end, θ is found to be between 25° and 35° .^[37] In some extreme cases tilt angles of almost 45° have been observed.^[38] The layer spacing (d -spacing) is determined by the length of the mesogen L , the conformational disorder, the amount of interdigitation, and the tilt (θ) of the mesogens.^[39] Generally,

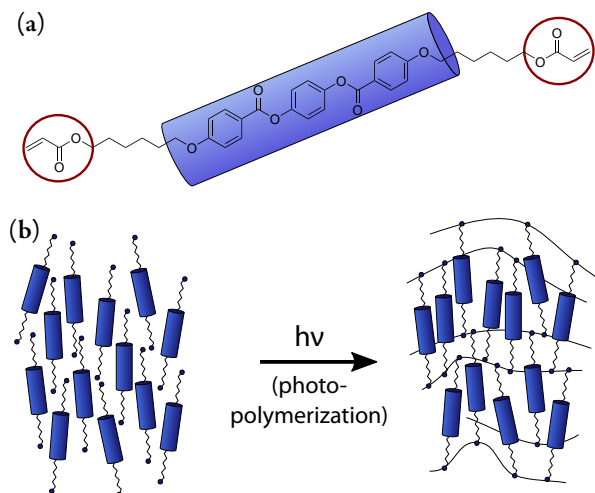


Figure 1.3: Preparation of liquid crystal networks. (a) A typical structure of a reactive liquid crystal. A rigid core segment consisting of multiple linearly linked aromatic rings bearing flexible endgroups containing polymerizable on the extremities. (b) Schematic representation of the photopolymerization of reactive liquid crystals in the nematic mesophase.

the d -spacing lies between $L/\sqrt{2}$ (extreme tilt angle) and $2L$ (double layer structure).

Materials possessing the properties discussed above can exhibit a high order and anisotropic properties, but they are not yet suitable for the fabrication of nanoporous polymers. No stable films or coatings can be prepared from the material since it is, although sometimes highly viscous, still fluid. By equipping the mesogens with reactive groups on their extremities (Figure 1.3a), the order can be locked-in by photopolymerization (Figure 1.3b). Various reactive groups have been reported, including alkenes and thiols,[40–42] dienes,[43] (meth)acrylates[44], and oxetanes and epoxides.[45] Among the various types, the acrylic reactive LCs the most abundant since their synthesis is relatively straight forward, stability is decent, and their polymerization is robust and well understood. After the *in situ* polymerization of these self-organized reactive mesogens, highly cross-linked networks that can no longer undergo phase transitions are obtained. Although this implies by definition that these anisotropic networks are not liquid crystalline anymore, they retain the label liquid crystal networks (LCNs).

An elegant and appealing bottom-up approach of fabricating nanoporous polymers is by using the self-organization of (reactive) liquid crystals (LCs) that can be (photo)polymerized. Liquid crystals can organize in large and ordered assemblies at the molecular

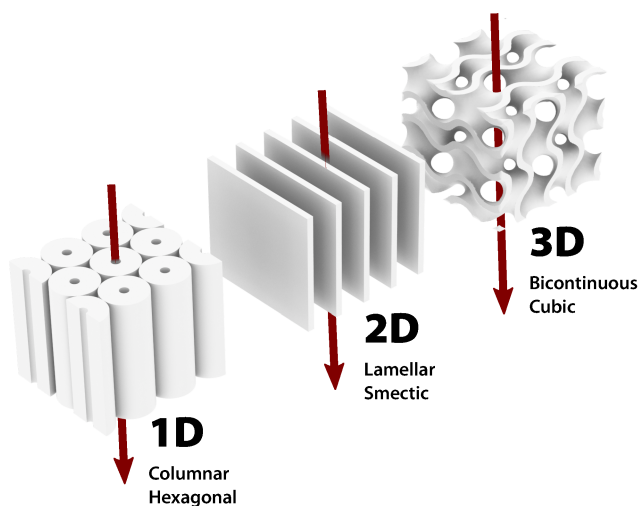


Figure 1.4: Nanoporous liquid crystal networks can be produced having various geometries. Columnar and hexagonal mesophases yield 1D pores, lamellar or smectic mesophases yield 2D pores, and bicontinuous cubic mesophases give a 3D pore geometry.

length-scale. After polymerization, highly anisotropic thermal, optical, and mechanical properties are obtained in these polymers. These unique properties have been translated to diverse application in *e.g.* sensors,[46] optical elements,[47, 48] and actuators.[49–51] By blueprinting the nanoporosity in the liquid crystalline building blocks, aligned pores of which the size can be reduced to 1 nm and below can be obtained (*vide infra*).

The polymerization of both lyotropic liquid crystals and thermotropic liquid crystals for the fabrication of nanoporous polymers have been reported. In the case of lyotropic LCs, the size of the pores in the polymerized network is determined by the amount of water (solvent) present in the organized mesophase. The general approach to create nanoporous LCNs based on thermotropic LCs involves the use of hydrogen-bonds in the core of the mesogen. Either by breaking the hydrogen bonds, that is, deprotonation of hydrogen bonded carboxylic acid moieties, or removal of a hydrogen bonded template, nanoporosity is obtained.

The morphology of the nanopores obtained can be controlled by the choice of mesogen and mesophase (Figure 1.4). One dimensional pores can be obtained by, as examples, hexagonal or columnar mesophases in lyotropic LCs or thermotropic discotic LCs.[52, 53] Lamellar (2D) morphologies can be obtained using thermotropic calamitic LCs po-

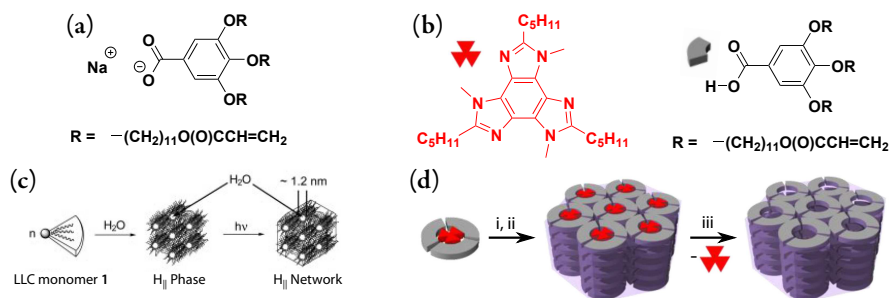


Figure 1.5: The fabrication of nanoporous hexagonal and columnar liquid crystal networks. (a) Chemical structure of the lyotropic galate moiety used by Zhou et al. (b) The chemical structures of the template and gallic acid derivative used by Lee et al. (c) Procedure for the fabrication of the nanoporous hexagonal polymer. (d) Procedure for the fabrication nanoporous columnar polymer, including the self-assembly, polymerization, and removal of the template moiety. Partly reproduced from [55, 57].

lymerized in the smectic mesophase. Polymer networks containing tortuous three dimensional pores have been prepared by polymerizing lyotropic liquid crystals in the bi-continuous cubic mesophase. In the sections below, the recent developments related to each type of morphology will be discussed.

1.2.1 Columnar and hexagonal mesophases (1D pores)

By using monomeric mesogens exhibiting columnar or hexagonal mesophases, nanoporous materials containing straight one dimensional pores can be obtained.[52, 53] Two main approaches, both involving a wedge-shaped gallic acid derived monomer, are widely followed in the production of this kind of material (Figure 1.5). The first is based on the deprotonation of the acid to yield the gallate salt (Figure 1.5a). The salt can be used either as a thermotropic[54] or lyotropic[55, 56] liquid crystal. Polymerization of the lyotropic mesogen in the inverted hexagonal phase resulted in cylindrical aqueous channels (Figure 1.5c). When coated on a porous support, such a material can potentially be used as selective layer for nanofiltration.[55]

The other approach uses a hydrogen bonded template that can form a thermotropic columnar mesophase when bonded to the gallic acid derived monomer (Figure 1.5b).[57] After polymerization and subsequent removal of the template moiety, a nanoporous material was obtained (Figure 1.5d). Ishida *et al.* showed that smaller molecules (2-amino alcohols) also can be used as templates.[58–61] In a later publication they showed that after template removal from the columnar network, all order was erased. By

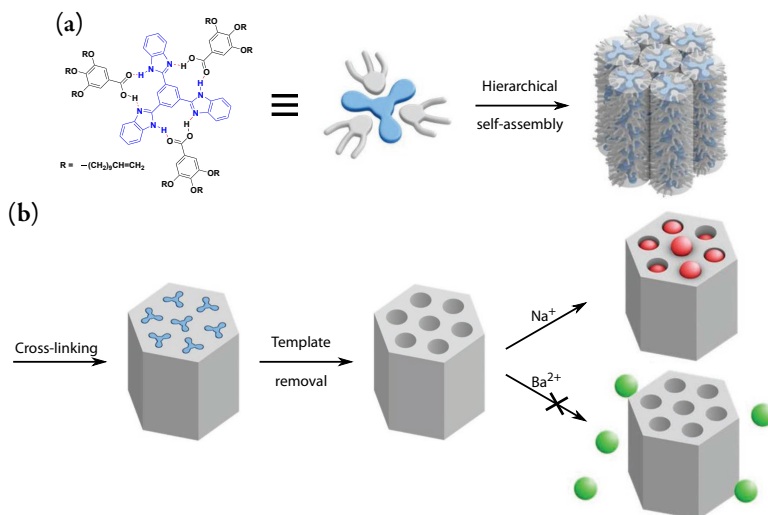


Figure 1.6: Nanoporous polymers using a gallic acid derived monomer and trisbenzimidazole template. (a) Hierarchical self-assembly of the monomers. (b) Synthesis of the nanoporous polymer and size selective adsorption. Adapted from [62].

subsequently reabsorbing the template molecule, the order could be restored.[59] By using a chiral 2-amino alcohol template and aligning the liquid crystals in a magnetic field, Li *et al.* showed that the chirality of the template was translated to the polymer host, and helical pores were obtained.[61] Still later it was shown that the amount of order retained after template removal could be improved by altering the reactive groups from acrylates to alkenes.[60] Using a similar template-approach, Bögels *et al.* prepared a nanoporous polymer based on the hydrogen bonded trisbenzimidazole—gallic acid mesogens (Figure 1.6a).[62] Using an acyclic diene metathesis reaction, the reactive gallic acid derivatives were cross-linked. After the subsequent removal of the benzimidazole porogen, a nanoporous material was obtained. The small sized anionic nanopores could discriminate monovalent metal ions from multivalent metal ions by ion-exchange.

Using natural unsaturated fatty acids together with the previously mentioned benzimidazole template, Feng *et al.* prepared nanoporous polymers with pores a diameter of 1.2 – 1.5 nm.[63] The hydrogen bonded fatty acid/template complex formed a hexagonal mesophase that was copolymerized with additional bifunctional monomers to obtain a crosslinked network (Figure 1.7a–d). The benzimidazole template was washed out under alkaline conditions in DMSO to obtain anionic nanopores (Figure 1.7e).

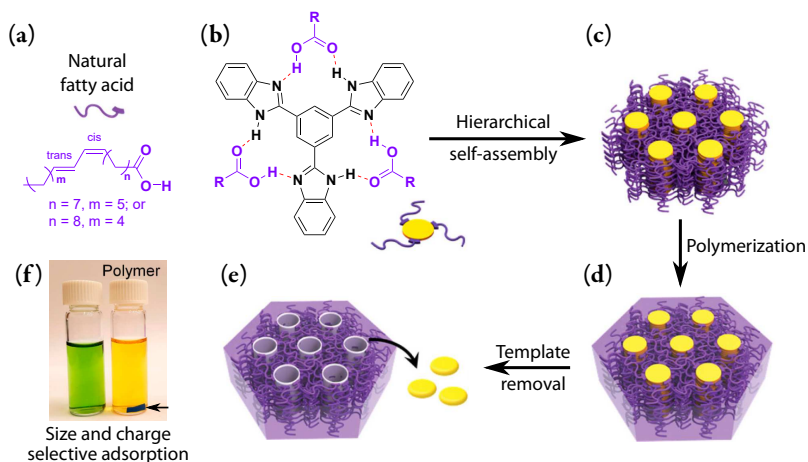


Figure 1.7: Natural fatty acids have been used for the fabrication of columnar nanoporous liquid crystal networks. (a) The chemical structure of the fatty acid monomer. (b–c) The supramolecular discotic complex formed by fatty acids and the template molecule and its self-assembled columnar mesophase, respectively. (d) An ordered polymeric network is obtained by radical cross-linking of the columnar mesophase. (e) A nanoporous polymer was obtained after removing the template molecules. Reused from [63] under ACS AuthorChoice License.

The anionic pore interior was used to adsorb a variety of dyes, revealing size and charge selectivity; only cationic dyes of less than 1.8 nm in size were adsorbed. The pores in the material were permanent as long the material was kept in an aqueous environment. Complete drying of the material led to irreversible collapse.

Recently, many more examples were presented using new pre-mesogens and templates [64], a nanoporous superlattice [65] and adjustable chemistry. [66] Other approaches have been developed by, for instance, using metallo-mesogens and azobenzene towards the fabrication of light responsive nano-gates or nano-valves. [67]

So far, the chemical versatility of 1D nanoporous polymer materials looks promising. However, one of the greatest challenges remains the alignment of the columnar or hexagonal mesophases. In order to obtain well-defined continuous pores from the top to the bottom of the polymer membrane, the initial columns in the mesophase must be aligned orthogonal to the surface (homeotropic). Any deviation from this would lead to dead-ends of the pores. Various examples have been shown to tackle this challenge. For example, Yoshio *et al.* prepared ion conducting membranes, by altering the surface chemistry of the substrate to align the columns. [68] The ion conductivity in the homeo-

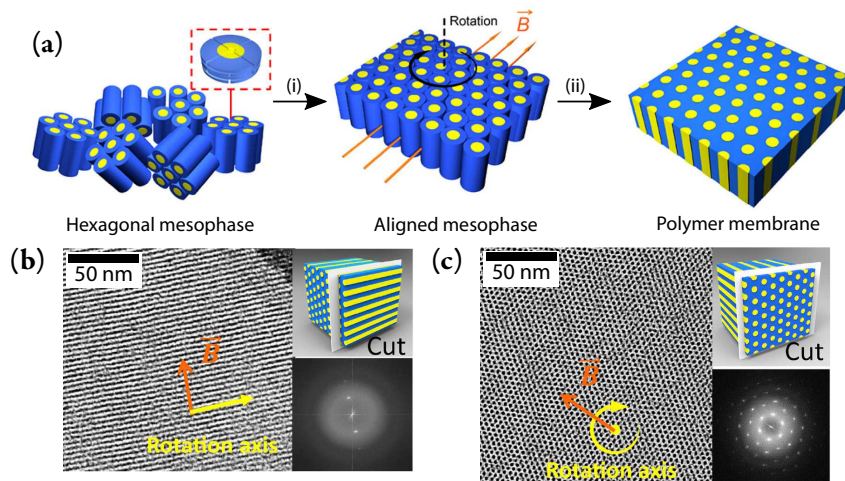


Figure 1.8: The alignment of hexagonal ordered liquid crystals in a magnetic field (a) Schematic representation of the alignment procedure. i) Alignment in magnetic field, ii) cross-linking using UV irradiation. (b,c) Transmission Electron microscopy images of the aligned material microtomed along (b) and perpendicular (c) to the columns. Adapted from [54] under ACS AuthorChoice License.

tropic aligned columns was 3 orders of magnitude higher than the initial planar aligned columns, showing the importance of alignment. The alignment in a magnetic field has emerged as a powerful method to reach well organized nanopores in lyotropic and thermotropic based columnar porous material (Figure 1.8a).[54, 61, 63, 69] Highly aligned monodomains were obtained by rotating the film inside the magnetic field as illustrated by transmission electron microscopy (Figure 1.8b). Very recently, less technically demanding alignment methods like soft confinement have been presented to obtain continuous homeotropic aligned pores.[70]

1.2.2 Bicontinuous and cubic mesophases (3D pores)

Despite the high degree of order currently achievable using hexagonal columnar phases, the alignment over large scale (>microns) has for a long time been limiting their processing applicability. An alternative is to use the bicontinuous mesophase that present the advantage of easy processability, and continuous channels from top to bottom of the membrane. There exists a broad range of examples using monomeric lyotropic liquid crystals for the preparation of nanoporous polymer networks with a 3D geometry. An example of an application for this material is the size discrimination based on the dia-

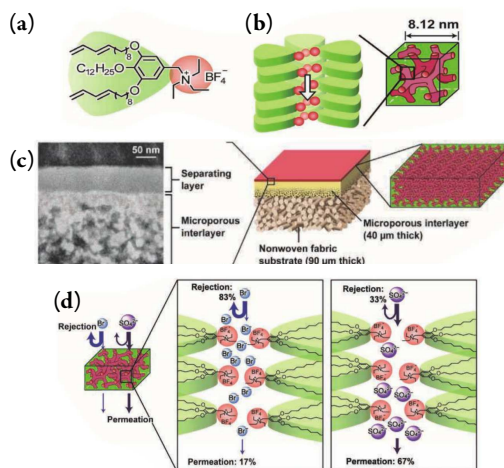


Figure 1.9: A thin separating layer based on a bicontinuous cubic polymer network. (a) Chemical structure of the wedge-shaped liquid crystalline monomer. (b) Self-assembled bicontinuous cubic LC phase forming ionic nanochannels. (c) Polymer membrane containing the polymerized liquid crystal network as a separating layer. (d) Schematic representation of selective rejection of anions through the membrane. Figure reproduced from [75] with permission from WILEY-VCH Verlag GmbH & Co. KGaA.

meter of the channels.[71] Such an approach also find function in breathable protective materials[72] or desalination.[73] Other examples describe the use of bicontinuous nanoporous networks that are able to remove viruses from water.[74] Recently, Henmi *et al.* presented the development of a thin separating layer based on a bicontinuous cubic polymer network (Figure 1.9a,b).[75] The material was constructed from a wedge shaped amphiphilic monomer having a cationic triethylammonium head. An approximately 50 nm thick coating layer was applied on a microporous support membrane to form a selective layer(Figure 1.9c). This work demonstrated materials with interesting salt-rejecting properties; small bromine anions were rejected and larger sulphate ions were passed through (Figure 1.9d).

1.2.3 Smectic and lamellar mesophases (2D pores)

Similarly to the nanoporous networks obtained from reactive lyotropic hexagonal and thermotropic columnar liquid crystals, the 2D pores obtained from lamellar or smectic mesophases display extremely low tortuosity. But, where the one dimensional porous materials often suffer from poor alignment, and thus dead-end pores, smectic liquid crystals can be aligned using traditional alignment techniques used in the liquid crystal dis-

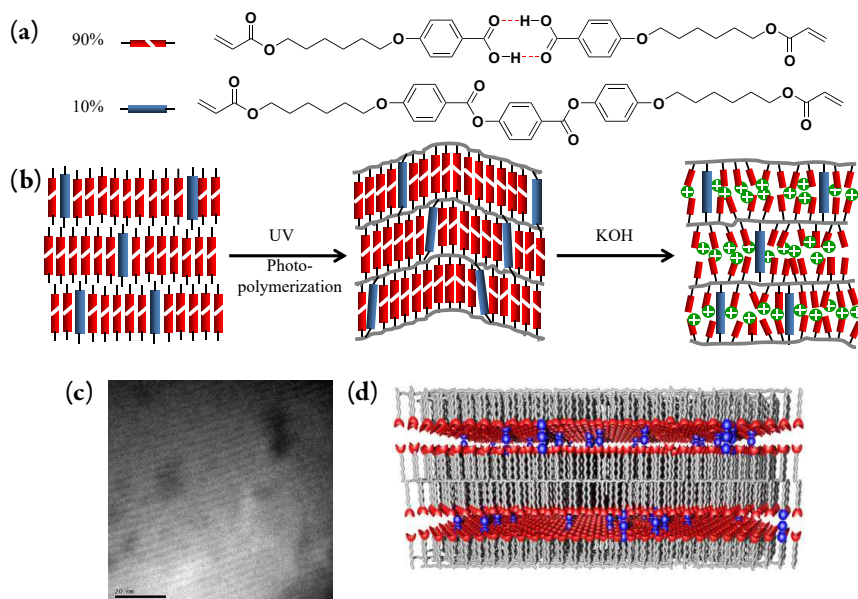


Figure 1.10: Fabrication of a nanoporous polymer having a 2D geometry. (a) Chemical structures of the monomers. Top: The hydrogen bonded liquid crystalline monomer. Bottom: Crosslinker. (b) Schematic overview of the fabrication. (c) Transmission electron micrograph of the 2D nanopores. (d) 3D representation of the lamellar pores. Reproduced from [83].

play industry. Previously, ion conducting materials have been prepared from either low molecular weight smectic liquid crystals[76–80] and polymeric systems.[81, 82] Although, these materials show unique anisotropic ionic conducting properties they are still considered as dense.

By the use of hydrogen bonded reactive mesogens[84], the porosity could be blueprinted in the liquid crystal monomers. After polymerizing the mesogens in the desired mesophase, the hydrogen bonds can be broken to obtain nanoporosity. One can foresee that without using a linking unit between the lamellae, disintegration of the layers would occur once the hydrogen bonds are broken. Kishikawa *et al.* presented an approach where they incorporated reactive “nanopillars” to hold the layers together after removal of a hydrogen bonded template (porogen).[85] A mixture containing the hydrogen bonded smectic LC monomer and the covalent nanopillar monomers was polymerized in the smectic mesophase whereafter the template was washed out using hydrochloric acid solution. By X-ray diffraction they showed that the order was maintained to some degree after the removal of the template. In the same year Gonzalez *et al.* presented a similar ap-

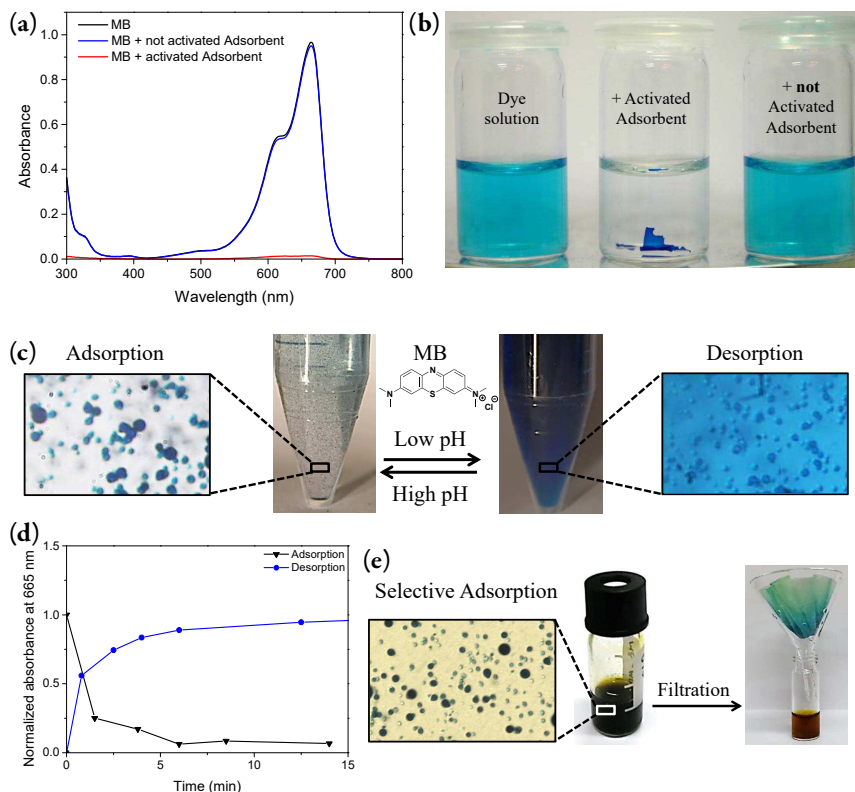


Figure 1.11: 2D nanoporous polymers as adsorbents. (a–b) The adsorption of methylene blue by polymeric films. (c) The adsorption of methylene blue by small nanoporous particles. (d) Profile of the adsorption and desorption kinetics. (e) Separation of a cationic (methylene blue) and anion (methyl orange) dye by the nanoporous LCN particles.

proach using hydrogen bonded benzoic acid derived LC monomers (Figure 1.10a).[83] In this strategy, the nanopores of approximately 1 nm (Figure 1.10c) are formed by breaking the hydrogen bonds using a basic solution. During this treatment, an anisotropic expansion was observed. The material expanded approximately 50% perpendicular to the molecular director, while along the director nearly no change was observed.[86] After alkaline treatment of the hydrogen bonded network, a nanoporous polymer containing two dimensional nanopores with an anionic charge were obtained (Figure 1.10b). It was found that the charged polymer can be used as an efficient adsorbent for cationic species.[87] In a set of adsorption experiments it was demonstrated that small cationic dyes like methylene blue (Figure 1.11a & b) are adsorbed with an occupation level of 100 % (1 gram of dye per gram of material). When an anionic dye (methyl orange) was

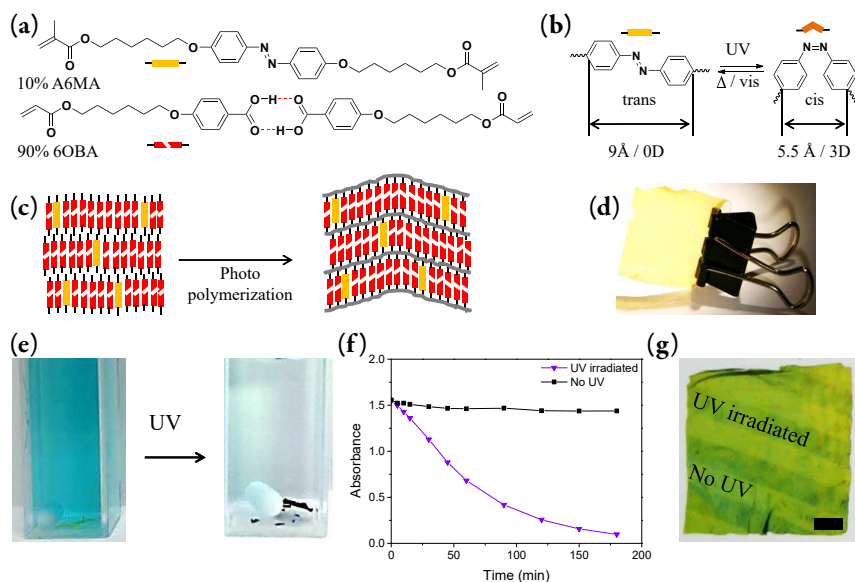


Figure 1.12: A photoresponsive adsorbent. (a) The chemical structures of the monomers. (b) Trans–cis isomerization. (c) Schematic representation of the polymerization. (d) The obtained nanoporous film. (e) Cuvettes containing a methylene blue solution at pH 9.5 and the photoresponsive adsorbent. On the left, the cuvette before UV exposure and right, the cuvette after UV exposure. (f) Kinetic of the photoinduced adsorption. (g) Local patterning of the adsorptive sites.

used, no dye was adsorbed. Similar results were obtained when large cationic dendrimers were used, demonstrating the size and charge selectivity of the material.

So far, the smectic nanoporous polymers were produced in liquid crystal cells. This method limits the scalability of the production. Therefore, a suspension photopolymerization was used to prepare small adsorptive particles from a similar LC monomer mixture.[88] Using this polymerization technique, the production of the adsorbent could be scaled up. The obtained particles were a few micrometers large and had a radial alignment of the molecular director. Consequently, the nanopores were oriented concentric. The swelling of the particles upon alkaline treatment allowed the formation of the pores. At the maximum adsorption capacity (81 % occupation) 887 mg methylene blue was adsorbed per gram particles. The reason the capacity could reach only 81 % was attributed to the alignment of the mesogens in the particle. As a consequence of the radial alignment, the pores are oriented concentrically, which might hamper the adsorption. Nonetheless, the particles show enhanced adsorption kinetics, and the dye was released efficiently at lower pH (Figure 1.11c–e).

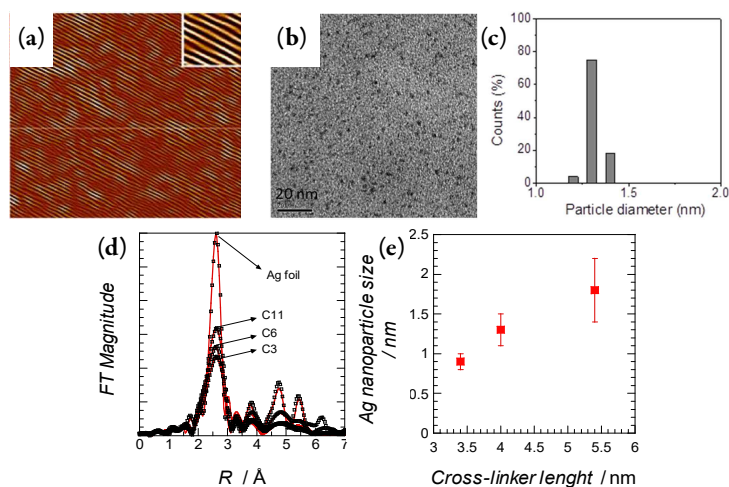


Figure 1.13: The synthesis of silver nanoparticles inside the 2D lamellae of the nanoporous polymer. (a) Atomic force micrograph showing the lamellar structure after nanoparticle synthesis. (b) Transmission electron micrograph (TEM) showing the nanoparticles. (c) Size estimation of the particles based on the TEM observation. (d) Fourier transformed data extracted from the EXAFS measurement. (e) Particle size estimation as function of the cross-linker length based on the EXAFS data.

By substituting the crosslinker by an azobenzene variant (Figure 1.12a), a photoresponsive nanoporous LCN was obtained.[89] Azobenzenes can undergo trans-to-cis isomerization when exposed to UV-light. The isomerization process led to a small change in the lamellar spacing of the nanoporous smectic network, and a change in pKa of the benzoic acid moieties. This change in pKa was caused by the dipole moment that was induced in the azobenzene moieties once isomerized to the cis-form (Figure 1.12b). In this way, the hydrogen bonds could be selectively broken under the influence of light at pH 9.5. Using the same conditions the methylene blue dye could be adsorbed *in situ* (Figure 1.12c–g).

Another application of lamellar nanoporous polymers was presented by Dasgupta *et al.* By using the same hydrogen bonded reactive liquid crystal with a variety of crosslinkers of different lengths, the nano sized pores were used for the synthesis of silver nanoparticles.[90, 91] By varying the length of the crosslinker, the size of the particles could be controlled. The method includes the ion exchange of the potassium for silver ions after formation of the pores. Subsequently, the silver ions were reduced using sodium boro-

hydride. The size of the particles was evaluated by various microscopy techniques and X-ray scattering and spectroscopy techniques. From these results it was concluded that the size of the particles could be influenced by the length of the cross-linker. A longer cross-linker led to a larger space between the layers, allowing the particles to grow larger. A precise control over the size of nanoparticles is desired to tailor the optical and catalytic properties.

1.3 Aim and outline of this thesis

Numerous examples of nanoporous polymers based on liquid crystalline monomers have been studied as can be concluded from this literature overview. However, the post modification of the pore chemistry and material geometries rather than films has been rarely addressed. For example, often the nanoporous films are fabricated using reactive mesogens that exhibit a hydrogen bonded benzoic acid derived core that leads to anionic carboxylate pores after pore formation. The pore character is static and restricted to basic environments and limits the opportunities for further development and functionalization.

The aim of this thesis is to take the concept of nanoporous liquid crystalline polymers a step forward by developing novel nanoporous polymeric materials prepared from smectic liquid crystalline monomers that offer a new pore chemistry. The research is focused on the exploration of new pore functionalities and strategies to prepare the nanoporous materials. Strategies include the use of dynamic covalent chemistry and hydrogen bonded heterodimers, moving away from the traditional benzoate pore surface. The new strategies open doors for post-modifications of the interior of the pores, making the system more versatile. The aforementioned control makes this kind of material of interest for, for instance, filtration, ion-exchange, adsorption, proton conduction, and nanoreactors. In parallel, the fabrication of nanoporous polymeric materials in new geometries is explored for future applications.

Chapter 2 describes a method based on dynamic covalent chemistry to prepare nanoporous smectic LCNs. The concept is based on the use of a (bis)imine liquid crystal monomer. After hydrolysis of the imine bonds a polymer with aldehyde functionalities is obtained which can be post-modified using a variety of amine to tune the size and polarity and crowdedness of the nanopores. The impact of the post-modification is de-

monstrated in the selective sorption of dyes.

In Chapter 3, another new approach to obtain nanoporous polymer networks containing cationic pores is described; hydrogen-bonded heterodimers are utilized to reach a basic pore interior. One part of the heterodimer is a monomeric stilbazole unit and the other part a non-reactive benzoic acid derivative (porogen). After fabrication of the aligned polymer material and the subsequent removal of the non-reactive porogen, a nanoporous liquid crystalline network is obtained. This basic pore interior can interact with various inorganic and organic acids leading to a cationic pore surface. This latter is demonstrated by the adsorption of phosphoric acid, leading to a well performing proton conducting membrane.

The synthesis of gold nanoparticles inside basic pyridyl pores is described in Chapter 4. Gold nanoparticles are formed after infiltration and reduction of a gold precursor. The mechanism, based on diffusion, is elucidated. The new insights pave way for the fabrication of hybrid nanoporous materials for *e.g.* size selective catalysis. The fabrication of responsive nanopores polymeric vesicles that change their properties upon an external trigger are of interest for medicine and heterogeneous catalysis applications.

In Chapter 5, the fabrication and thermal actuation of liquid crystalline elastomers (LCEs) in a shell geometry is presented. The LCEs shells were prepared from reactive liquid crystalline oligomers by capillary microfluidics. The thermomechanical properties of both the LCE and the shells are discussed. The actuation of the elastomeric shells may find one application in micropumps and drug delivery systems.

In the final chapter, Chapter 6, new opportunities for development arising during this project are described. This extends further the range of applications, the versatile chemistry and the various developments worth considering using nanoporous liquid crystalline materials.

1.4 References

- [1] R. L. BURWELL JR. in *Manual of Symbols and Terminology for Physicochemical Quantities and Units—Appendix II*, Pergamon, 1976, pp. 74–86.
- [2] B. Ghanbarian, A. G. Hunt, R. P. Ewing, M. Sahimi, *Soil Sci. Soc. Am. J.* **2013**, *77*, 1461–1477.

-
- [3] WHO | Drinking-Water, <http://www.who.int/mediacentre/factsheets/fs391/en/> (visited on 07/18/2017).
- [4] (L. Cerini), US1719754 A, U.S. Classification 423/181, 210/487, 423/183, 210/649; International Classification C01D1/00, C01D1/38; Cooperative Classification C01D1/38; European Classification C01D1/38, **1929**.
- [5] (L. Cerini), US1815761 A, U.S. Classification 8/115.6, 106/163.1, 210/508, 8/118, 8/125, 106/204.1, 204/296, 8/116.1; International Classification C01D1/38, C01D1/00; Cooperative Classification C01D1/38; European Classification C01D1/38, **1931**.
- [6] R. W. Baker, *Membrane Technology and Applications: Baker/Membrane Technology and Applications*, John Wiley & Sons, Ltd, Chichester, UK, **2012**.
- [7] P. Y. Apel, E. M. Hoek, V. V. Tarabara in *Encyclopedia of Membrane Science and Technology*, John Wiley & Sons, Inc., **2013**.
- [8] O. Ikkala, G. ten Brinke, *Science* **2002**, *295*, 2407–2409.
- [9] S. P. Nunes, *Macromolecules* **2016**, *49*, 2905–2916.
- [10] J. S. Lee, A. Hirao, S. Nakahama, *Macromolecules* **1988**, *21*, 274–276.
- [11] P. Mansky, C. K. Harrison, P. M. Chaikin, R. A. Register, N. Yao, *Appl. Phys. Lett.* **1996**, *68*, 2586–2588.
- [12] P. Mansky, P. Haikin, E. L. Thomas, *J. Mater. Sci.* **1995**, *30*, 1987–1992.
- [13] E. A. Jackson, M. A. Hillmyer, *ACS Nano* **2010**, *4*, 3548–3553.
- [14] P. Paik, A. Gedanken, Y. Mastai, *J. Mater. Chem.* **2010**, *20*, 4085–4093.
- [15] Z. Qiang, Y. Zhang, Y. Wang, S. M. Bhaway, K. A. Cavicchi, B. D. Vogt, *Carbon* **2015**, *82*, 51–59.
- [16] M. W. Matsen, *J. Chem. Phys.* **1997**, *106*, 7781–7791.
- [17] H. P. Huinink, J. C. M. Brokken-Zijp, M. A. van Dijk, G. J. A. Sevink, *J. Chem. Phys.* **2000**, *112*, 2452–2462.
- [18] S. Park, J.-Y. Wang, B. Kim, J. Xu, T. P. Russell, *ACS Nano* **2008**, *2*, 766–772.
- [19] W. Joo, S. Y. Yang, J. K. Kim, H. Jinnai, *Langmuir* **2008**, *24*, 12612–12617.
- [20] M. Li, K. Douki, K. Goto, X. Li, C. Coenjarts, D. M. Smilgies, C. K. Ober, *Chem. Mater.* **2004**, *16*, 3800–3808.
- [21] R. Mäki-Ontto, K. de Moel, W. de Odorico, J. Ruokolainen, M. Stamm, G. ten Brinke, O. Ikkala, *Adv. Mater.* **2001**, *13*, 117–121.
- [22] A. Sidorenko, I. Tokarev, S. Minko, M. Stamm, *J. Am. Chem. Soc.* **2003**, *125*, 12211–12216.
- [23] I. Vukovic, S. Punzhin, Z. Vukovic, P. Onck, J. T. M. De Hosson, G. ten Brinke, K. Loos, *ACS Nano* **2011**, *5*, 6339–6348.
- [24] H. Kosonen, S. Valkama, A. Nykänen, M. Toivanen, G. ten Brinke, J. Ruokolainen, O. Ikkala, *Adv. Mater.* **2006**, *18*, 201–205.
- [25] S. Valkama, A. Nykänen, H. Kosonen, R. Ramani, F. Tuomisto, P. Engelhardt, G. ten Brinke, O. Ikkala, J. Ruokolainen, *Adv. Funct. Mater.* **2007**, *17*, 183–190.

- [26] C. Liang, K. Hong, G. A. Guiochon, J. W. Mays, S. Dai, *Angew. Chem. Int. Ed.* **2004**, *43*, 5785–5789.
- [27] H. Zhang, Y. Fu, D. Wang, L. Wang, Z. Wang, X. Zhang, *Langmuir* **2003**, *19*, 8497–8502.
- [28] Q. Li, J. F. Quinn, F. Caruso, *Adv. Mater.* **2005**, *17*, 2058–2062.
- [29] V. Percec, A. E. Dulcey, V. S. K. Balagurusamy, Y. Miura, J. Smidrkal, M. Peterca, S. Nummelin, U. Edlund, S. D. Hudson, P. A. Heiney, H. Duan, S. N. Magonov, S. A. Vinogradov, *Nature* **2004**, *430*, 764–768.
- [30] M. N. Wadekar, W. F. Jager, E. J. R. Sudhölter, S. J. Picken, *J. Org. Chem.* **2010**, *75*, 6814–6819.
- [31] K.-V. Peinemann, V. Abetz, P. F. W. Simon, *Nat Mater* **2007**, *6*, 992–996.
- [32] P. Madhavan, B. Sutisna, R. Sougrat, S. P. Nunes, *RSC Adv* **2016**, *6*, 75594–75601.
- [33] Q. Zhang, Y. Gu, Y. M. Li, P. A. Beaucage, T. Kao, U. Wiesner, *Chem. Mater.* **2016**, *28*, 3870–3876.
- [34] C. T. Kresge, M. E. Leonowicz, W. J. Roth, J. C. Vartuli, J. S. Beck, *Nature* **1992**, *359*, 710–712.
- [35] D. Venkataraman, S. Lee, J. Zhang, J. S. Moore, *Nature* **1994**, *371*, 591–593.
- [36] K. Na, M. Choi, R. Ryoo, *Microporous Mesoporous Mater.* **2013**, *166*, 3–19.
- [37] I. Dierking, *Textures of Liquid Crystals*, Wiley-VCH Verlag GmbH & Co. KGaA, Weinheim, FRG, **2003**.
- [38] K. D'havé, A. Dahlgren, P. Rudquist, J. P. F. Lagerwall, G. Andersson, M. Matuszczyk, S. T. Lagerwall, R. Dabrowski, W. Drzewinski, *Ferroelectrics* **2000**, *244*, 115–128.
- [39] J. P. F. Lagerwall, F. Giesselmann, *ChemPhysChem* **2006**, *7*, 20–45.
- [40] J. Lub, D. J. Broer, N. van den Broek, *Liebigs Ann./Recl.* **1997**, *1997*, 2281–2288.
- [41] H. T. A. Wilderbeek, M. G. M. van der Meer, M. A. G. Jansen, L. Nelissen, H. R. Fischer, J. J. G. S. van Es, C. W. M. Bastiaansen, J. Lub, D. J. Broer, *Liq. Cryst.* **2003**, *30*, 93–108.
- [42] J. Lub, D. J. Broer, A. M. E. Martinez, G. N. Mol, *Liq. Cryst.* **1998**, *24*, 375–379.
- [43] B. P. Hoag, D. L. Gin, *Macromolecules* **2000**, *33*, 8549–8558.
- [44] D. J. Broer, H. Finkelmann, K. Kondo, *Makromol. Chem.* **1988**, *189*, 185–194.
- [45] J. Lub, V. Recaj, L. Puig, P. Forcén, C. Luengo, *Liq. Cryst.* **2004**, *31*, 1627–1637.
- [46] D. J. Mulder, A. P. H. J. Schenning, C. W. M. Bastiaansen, *J. Mater. Chem. C* **2014**, *2*, 6695–6705.
- [47] D. J. Broer, J. Lub, G. N. Mol, *Nature* **1995**, *378*, 467–469.
- [48] E. Peeters, J. Lub, J. a. M. Steenbakkens, D. J. Broer, *Adv. Mater.* **2006**, *18*, 2412–2417.
- [49] L. T. de Haan, C. Sánchez-Somolinos, C. M. W. Bastiaansen, A. P. H. J. Schenning, D. J. Broer, *Angew. Chem. Int. Ed.* **2012**, *51*, 12469–12472.
- [50] A. H. Gelebart, D. Jan Mulder, M. Varga, A. Konya, G. Vantomme, E. W. Meijer, R. L. B. Selinger, D. J. Broer, *Nature* **2017**, *546*, 632–636.
- [51] C. L. van Oosten, C. W. M. Bastiaansen, D. J. Broer, *Nat Mater* **2009**, *8*, 677–682.
- [52] T. Kato, T. Yasuda, Y. Kamikawa, M. Yoshio, *Chem Commun* **2009**, 729–739.

- [53] Y. Ishida, *Materials* **2011**, *4*, 183–205.
- [54] X. Feng, M. E. Tousley, M. G. Cowan, B. R. Wiesenaue, S. Nejati, Y. Choo, R. D. Noble, M. Elimelech, D. L. Gin, C. O. Osuji, *ACS Nano* **2014**, *8*, 11977–11986.
- [55] M. Zhou, T. J. Kidd, R. D. Noble, D. L. Gin, *Adv. Mater.* **2005**, *17*, 1850–1853.
- [56] R. C. Smith, W. M. Fischer, D. L. Gin, *J. Am. Chem. Soc.* **1997**, *119*, 4092–4093.
- [57] H.-K. Lee, H. Lee, Y. H. Ko, Y. J. Chang, N.-K. Oh, W.-C. Zin, K. Kim, *Angew. Chem. Int. Ed.* **2001**, *40*, 2669–2671.
- [58] Y. Ishida, S. Amano, K. Saigo, *Chem. Commun.* **2003**, *0*, 2338–2339.
- [59] Y. Ishida, S. Amano, N. Iwahashi, K. Saigo, *J. Am. Chem. Soc.* **2006**, *128*, 13068–13069.
- [60] Y. Ishida, H. Sakata, A. S. Achalkumar, K. Yamada, Y. Matsuoka, N. Iwahashi, S. Amano, K. Saigo, *Chem. Eur. J.* **2011**, *17*, 14752–14762.
- [61] C. Li, J. Cho, K. Yamada, D. Hashizume, F. Araoka, H. Takezoe, T. Aida, Y. Ishida, *Nat. Commun.* **2015**, *6*, 8418.
- [62] G. M. Bögels, J. A. M. Lugger, O. J. G. M. Goor, R. P. Sijbesma, *Adv. Funct. Mater.* **2016**, *26*, 8023–8030.
- [63] X. Feng, K. Kawabata, G. Kaufman, M. Elimelech, C. O. Osuji, *ACS Nano* **2017**, *11*, 3911–3921.
- [64] I. Gracia, P. Romero, J. L. Serrano, J. Barberá, A. Omenat, *J. Mater. Chem. C* **2017**, *5*, 2033–2042.
- [65] G. M. Bögels, H. P. C. van Kuringen, I. K. Shishmanova, I. K. Voets, A. P. H. J. Schenning, R. P. Sijbesma, *Adv. Mater. Interfaces* **2015**, *2*, 1500022.
- [66] S. Bhattacharjee, J. A. M. Lugger, R. P. Sijbesma, *Macromolecules* **2017**, *50*, 2777–2783.
- [67] C. S. Pecinovsky, E. S. Hatakeyama, D. L. Gin, *Adv. Mater.* **2008**, *20*, 174–178.
- [68] M. Yoshio, T. Kagata, K. Hoshino, T. Mukai, H. Ohno, T. Kato, *J. Am. Chem. Soc.* **2006**, *128*, 5570–5577.
- [69] M. E. Tousley, X. Feng, M. Elimelech, C. O. Osuji, *ACS Appl. Mater. Interfaces* **2014**, *6*, 19710–19717.
- [70] X. Feng, S. Nejati, M. G. Cowan, M. E. Tousley, B. R. Wiesenaue, R. D. Noble, M. Elimelech, D. L. Gin, C. O. Osuji, *ACS Nano* **2016**, *10*, 150–158.
- [71] M. Zhou, P. R. Nemade, X. Lu, X. Zeng, E. S. Hatakeyama, R. D. Noble, D. L. Gin, *J. Am. Chem. Soc.* **2007**, *129*, 9574–9575.
- [72] X. Lu, V. Nguyen, M. Zhou, X. Zeng, J. Jin, B. J. Elliott, D. L. Gin, *Adv. Mater.* **2006**, *18*, 3294–3298.
- [73] R. L. Kerr, S. A. Miller, R. K. Shoemaker, B. J. Elliott, D. L. Gin, *J. Am. Chem. Soc.* **2009**, *131*, 15972–15973.
- [74] N. Marets, D. Kuo, J. R. Torrey, T. Sakamoto, M. Henmi, H. Katayama, T. Kato, *Adv. Healthc. Mater.* **2017**, 1700252.
- [75] M. Henmi, K. Nakatsuji, T. Ichikawa, H. Tomioka, T. Sakamoto, M. Yoshio, T. Kato, *Adv. Mater.* **2012**, *24*, 2238–2241.

- [76] T. Ohtake, K. Ito, N. Nishina, H. Kihara, H. Ohno, T. Kato, *Polym J* **1999**, *31*, 1155–1158.
- [77] T. Ohtake, M. Ogasawara, K. Ito-Akita, N. Nishina, S. Ujiie, H. Ohno, T. Kato, *Chem. Mater.* **2000**, *12*, 782–789.
- [78] J. H. Lee, K. S. Han, J. S. Lee, A. S. Lee, S. K. Park, S. Y. Hong, J.-C. Lee, K. T. Mueller, S. M. Hong, C. M. Koo, *Adv. Mater.* **2016**, *28*, 9301–9307.
- [79] T. Mukai, M. Yoshio, T. Kato, M. Yoshizawa, H. Ohno, *Chem. Commun.* **2005**, *0*, 1333–1335.
- [80] T. Liang, Y. Wu, S. Tan, X. Yang, B. Wei, *Chem. Phys. Lett.* **2015**, *637*, 22–25.
- [81] K. Kishimoto, M. Yoshio, T. Mukai, M. Yoshizawa, H. Ohno, T. Kato, *J. Am. Chem. Soc.* **2003**, *125*, 3196–3197.
- [82] L. Ramón-Gimenez, R. Storz, J. Haberl, H. Finkelmann, A. Hoffmann, *Macromol. Rapid Commun.* **2012**, *33*, 386–391.
- [83] C. L. Gonzalez, C. W. M. Bastiaansen, J. Lub, J. Loos, K. Lu, H. J. Wondergem, D. J. Broer, *Adv. Mater.* **2008**, *20*, 1246–1252.
- [84] S. J. Rowan, P. T. Mather in *Liquid Crystalline Functional Assemblies and Their Supramolecular Structures*, (Ed.: T. Kato), Structure and Bonding 128, Springer Berlin Heidelberg, **2007**, pp. 119–149.
- [85] K. Kishikawa, A. Hirai, S. Kohmoto, *Chem. Mater.* **2008**, *20*, 1931–1935.
- [86] I. K. Shishmanova, C. W. M. Bastiaansen, A. P. H. J. Schenning, D. J. Broer, **2012**, *48*, 4555–4557.
- [87] H. P. C. van Kuringen, G. M. Eikelboom, I. K. Shishmanova, D. J. Broer, A. P. H. J. Schenning, *Adv. Funct. Mater.* **2014**, *24*, 5045–5051.
- [88] H. P. C. van Kuringen, D. J. Mulder, E. Beltran, D. J. Broer, A. P. H. J. Schenning, **2016**, *7*, 4712–4716.
- [89] H. P. C. van Kuringen, Z. J. W. A. Leijten, A. H. Gelebart, D. J. Mulder, G. Portale, D. J. Broer, A. P. H. J. Schenning, *Macromolecules* **2015**, *48*, 4073–4080.
- [90] D. Dasgupta, I. K. Shishmanova, A. Ruiz-Carretero, K. Lu, M. Verhoeven, H. P. C. van Kuringen, G. Portale, P. Leclère, C. W. M. Bastiaansen, D. J. Broer, A. P. H. J. Schenning, *J. Am. Chem. Soc.* **2013**, *135*, 10922–10925.
- [91] A. Longo, D.-J. Mulder, H. P. C. van Kuringen, D. Hermida-Merino, D. Banerjee, D. Dasgupta, I. K. Shishmanova, A. B. Spoelstra, D. J. Broer, A. P. H. J. Schenning, G. Portale, *Chem. Eur. J.* **2017**, *10.1002/chem.201701493*.

Chapter 2

Adjustable nanoporous materials based on dynamic covalent chemistry

Abstract

In this chapter, a novel approach to obtain nanoporous smectic liquid crystalline polymer networks by dynamic covalent chemistry is presented. Dynamic covalent chemistry displays many advantages such as versatility and adjustability of a given material. A binary mixture of reactive smectic liquid crystalline monomers, of which one contains a bisimine template, is used to fabricate polymer networks. The bisimine is subsequently hydrolyzed leading to the formation of two-dimensional nanopores having an aldehyde functionality. Post modification with a variety of amines is proven to be possible and gives access to tunable pores. The lamellar structure of the post-modified material adapts to the size of the amine. The new interior was locked-in by the reduction of the imine moieties to *sec*-amines. The findings of this research give opportunities to fabricate nanoporous materials with adjustable properties in a facile fashion.

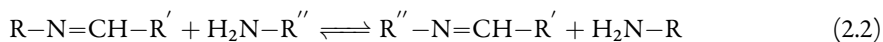
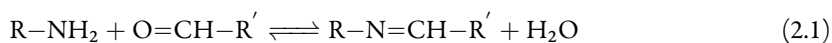
This chapter is partially reproduced from:

Fabrication and Post-Modification of Nanoporous Liquid Crystalline Networks via Dynamic Covalent Chemistry, D. J. Mulder, L. M. W. Scheres, Jingjin Dong, Giuseppe Portale, D. J. Broer, A. P. H. J. Schenning *Chem. Mater.* **2017**, *29*, (16), 6601–6605

2.1 Introduction

In the last decade, self-organized liquid crystalline systems have proven to be useful to prepare porous materials with pore sizes around 1 nm.[1, 2] Both lyotropic and thermotropic liquid crystal polymers have been employed by incorporating polymerizable groups with the liquid crystalline moieties using columnar, lamellar or bicontinuous cubic phases.[3, 4] In lyotropic liquid crystals, pores are created and size controlled by ions and the solvent, *i.e.* water.[5, 6] In thermotropic liquid crystals, nanopores have been created by so-called porogen templates which are initially hydrogen bonded to the polymer network and subsequently washed away to create the pore structures.[7–10] So far, most of the pores that have been made, are based on negatively charged carboxylates[8, 11, 12] but there are some examples of neutral[7] or positively charged[13] pores. These pre-functionalization approaches limit the control over the size and chemical nature of the pores and the set of molecules and ions that can be separated.[11, 12] Therefore the control of pore size and the chemical tunability of the porous material remains a challenge.

In this chapter a facile method to fabricate and post-modify nanoporous liquid crystal polymer materials by using dynamic covalent chemistry is presented. Dynamic covalent bonds can form and break (Equation 2.1), or exchange (Equation 2.2) under an external stimulus, such as the addition of a catalyst[14], a change of environment (solvent)[15, 16], or heat. For this reason, they are appealing to be used as adaptive and self-healing materials, for example.[16, 17]



Here, the photopolymerization of a reactive thermotropic smectic LC monomer containing a bisimine porogen (Figure 2.2a, compound 1) and a reactive crosslinker (compound 2) to yield a polymer film that after acid treatment contains reactive pore surface aldehyde functionalities is described.[12] By post-modification of these moieties with a variety of amines, the size and chemical nature of the pores can be tuned in a facile fashion (Figure 2.1).

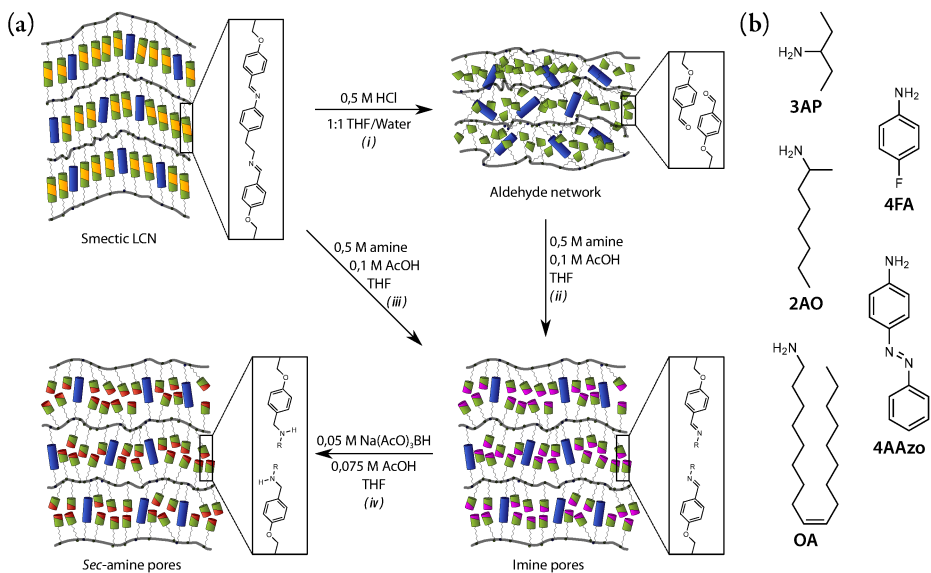


Figure 2.1: Chemical post-modification of the bisimine LCN films. (a) Schematic representation of the various post-modification reactions. *i*; hydrolysis, *ii*; imination, *iii*; transimination, *iv*; reductive amination. (b) Structure of the amines that were used; 3-aminopentane (3AP), 2-amino-octane (2AO), oleylamine (OA), 4-fluoroaniline (4FA), 4-aminoazobenzene (4AAzo).

2.2 Results and discussion

2.2.1 Synthesis and phase behavior of the monomers

The newly developed reactive bisimine **1** was prepared in a 2-step synthesis route starting from 4-(6-hydroxyhexyloxy)benzaldehyde. First, a methacrylate ester was prepared, whereafter **1** was obtained from the condensation reaction of the aldehyde with 4-(2-aminethyl)aniline. A methacrylate was used instead of acrylate to prevent side reactions while synthesizing the bisimine. The bisimine LCN film in this research is based on 4-(2-aminethyl)aniline (compound **1**), and exhibits a smectic phase in a suitable working temperature range ($< 120\text{ }^{\circ}\text{C}$). Fully aromatic diamines were also investigated, but these resulted in compounds exhibiting higher mesophase temperatures, increasing the risk of premature polymerization during further processing. Cross-linker **2**, which has a similar molecular length to bisimine **1**, was prepared analogous to the procedure described in the literature [18, 19]; by the formation of the diazonium salt of 1,2-bis(4-aminophenyl)ethane, and the subsequent hydrolysis of it, 1,2-bis(4-hydroxyphenyl)ethane was obtained. Subsequently, by Steglich esterification of the obtained diol with 4-(6-acryloyloxy-

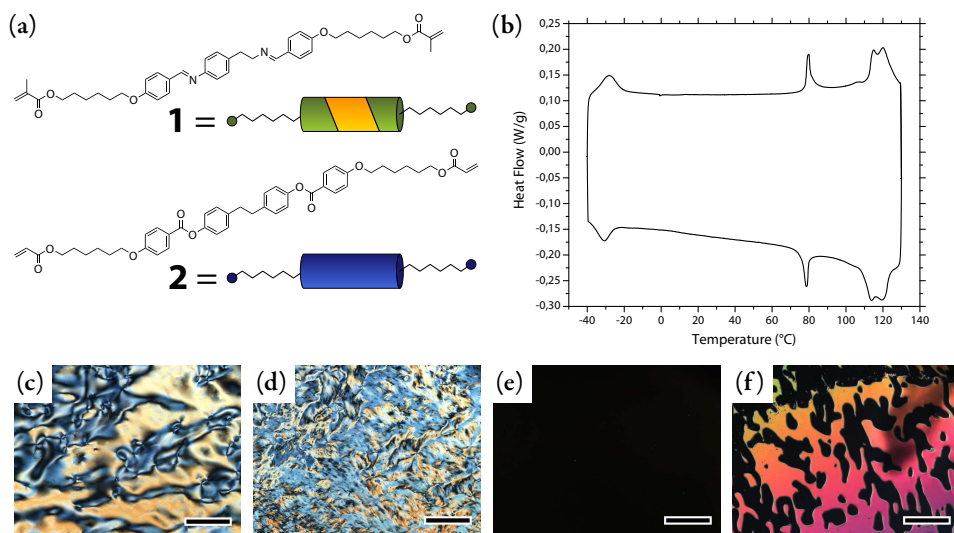


Figure 2.2: Phase behavior of the monomer mixture containing 20 wt% CL. (a) Chemical structures of the liquid crystal monomers. (b) DSC trace of the mixture (exothermal down). (c-f) Polarized light micrographs of the mixture under homeotropic boundary conditions at 30 °C (*SmX*), 90 °C (*SmC*), 115 °C (*SmA*), and 120 °C (*N*, while shearing), respectively. Scale bar = 250 microns.

hexyloxy)benzoic acid, compound 2 was obtained. The thermal characterization of the pure compounds can be found in Figure 2.10 and Figure 2.11 in the appendix.

To prepare the smectic liquid crystalline network, a mixture containing the bisimine **1** and cross-linker **2** was used. Crosslinking is needed to avoid disintegration of the layers when the central units of **1** are removed. It was found that 20 wt% cross-linker was sufficient to keep the layered structure intact after removal of the bisimine template after polymerization (*vide infra*). The phase behavior of the new mixture was studied by DSC and polarized optical microscopy (Figure 2.2). Upon cooling from the isotropic phase a nematic mesophase is observed from 120 °C to 117 °C. The mixture shows a smectic A mesophase from 117 °C to 104 °C while a smectic C mesophase is present from 104 °C to 78 °C. Below this temperature a higher order tilted smectic phase was observed until -32 °C, whereafter crystallization sets in.

2.2.2 Fabrication of the nanoporous LCN

In order to perform the photopolymerization, 1 wt% photoinitiator (Irgacure 819) and 0,5 wt% inhibitor (Butylated hydroxytoluene, BHT) were added to the monomer mix-

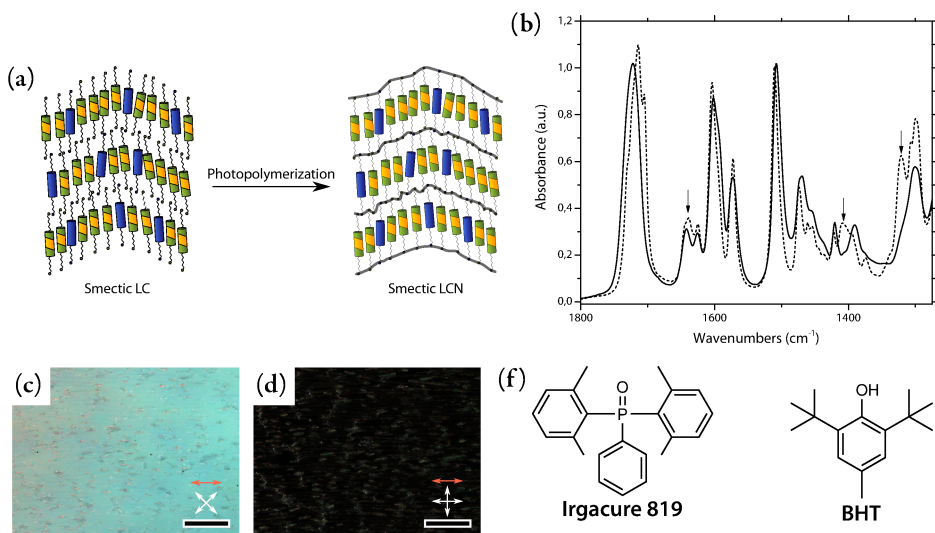


Figure 2.3: Photopolymerization of the smectic LC. (a) Schematic representation of the photopolymerization. (b) ATR FTIR spectra of the monomer mixture (short-dash line) and the LCN (solid line). (c) and (d) Polarized optical micrographs of the LCN between crossed polars at 45° and 0°, respectively. Scale bar = 250 microns. (f) Chemical structures of the photoinitiator (Irgacure 819) and inhibitor (BHT).

ture. The addition of inhibitor was necessary to circumvent premature thermal polymerization at elevated temperatures. The photopolymerization in a planar alignment was carried out in a homemade LC-cell provided with antiparallel rubbed polyimide alignment layer. This is essential for obtaining the pores orthogonal to the surface of the film after the removal of the template. After the photopolymerization in the smectic C mesophase, the LC-cell was opened and the polymeric film was characterized. Infrared spectroscopy confirms the conversion of the (meth)acrylic C=C bonds of the monomers (Figure 2.3b). Polarized light microscopy (Figure 2.3c and 2.3d) shows that the obtained polymer film is highly birefringent indicating a good alignment of the mesogenic moieties. X-ray diffractometry of the polymer film reveals a smectic organization of the molecules in the polymer network (Figure 2.4b). In the small-angle region of this plot, four small lobes can be observed corresponding to a typical smectic C chevron pattern. The spacing of the lamellae is 37 Å with a tilt angle of approximately 30°. Corrected for this tilt angle, a length of 43 Å is obtained, which is in agreement with the molecular length of compound **1** (43,3 Å, obtained by Chem3d minimization in stretched conformation).

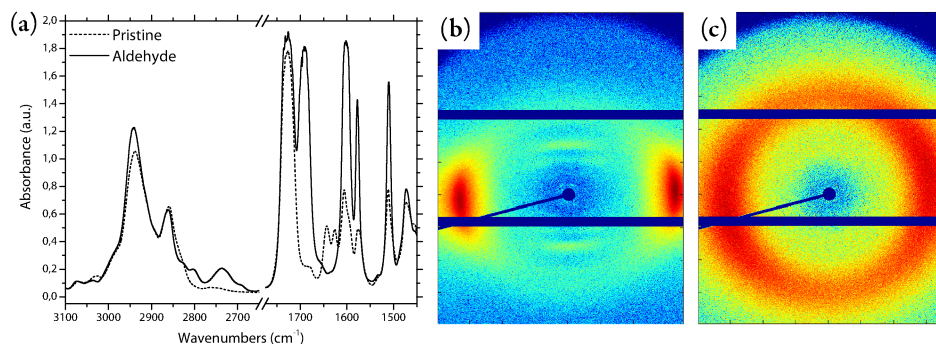


Figure 2.4: Removal of bisimine template by hydrolysis. (a) Transmission FTIR spectra of the pristine bisimine LCN (short-dash line) and the aldehyde functional network (solid line). (b) and (c) 2D x-ray diffractograms of the pristine bisimine LCN film and the aldehyde functional network, respectively.

In order to obtain a porous material with an aldehyde pore surface, the removal of the 4-(2-aminoethyl)aniline template was achieved by exposure of the network to a 0.5 M HCl solution in a 1:1 water/THF mixture overnight. The imine bonds were hydrolyzed and the diamine template was liberated from the polymer network. This was confirmed by transmission FTIR revealing a quantitative conversion of the imine groups to aldehyde functionalities (Figure 2.4a). No hydrolysis of the acrylate backbone was observed. The bisimine materials showed two distinct absorption bands at 1645 cm^{-1} and 1625 cm^{-1} corresponding to the aliphatic and aromatic C=N stretch vibrations, respectively. The two peaks fully disappeared after the hydrolysis and two new peaks appeared at 1690 cm^{-1} and 2740 cm^{-1} . The vibration band at 1690 cm^{-1} was assigned to the C=O stretch vibration of the aldehyde moiety; the product of the hydrolysis reaction, and the second peak originates from the aldehydic C-H stretch vibration, indicating an effective removal of the template and the formation of an aldehyde functional pore surface. X-ray diffraction of the dried films revealed that the lamellar ordered structure is significantly reduced after removal of the bisimine template, while only the orientation of the molecules was maintained to some degree (Figure 2.4c). Macroscopically, in the dried state, $29\pm 1\%$ contraction, and $8\pm 4\%$ expansion is observed along and perpendicular to the molecular director, respectively, indicating the collapse of the lamellar structure and loss of the order of the initially aligned molecules.

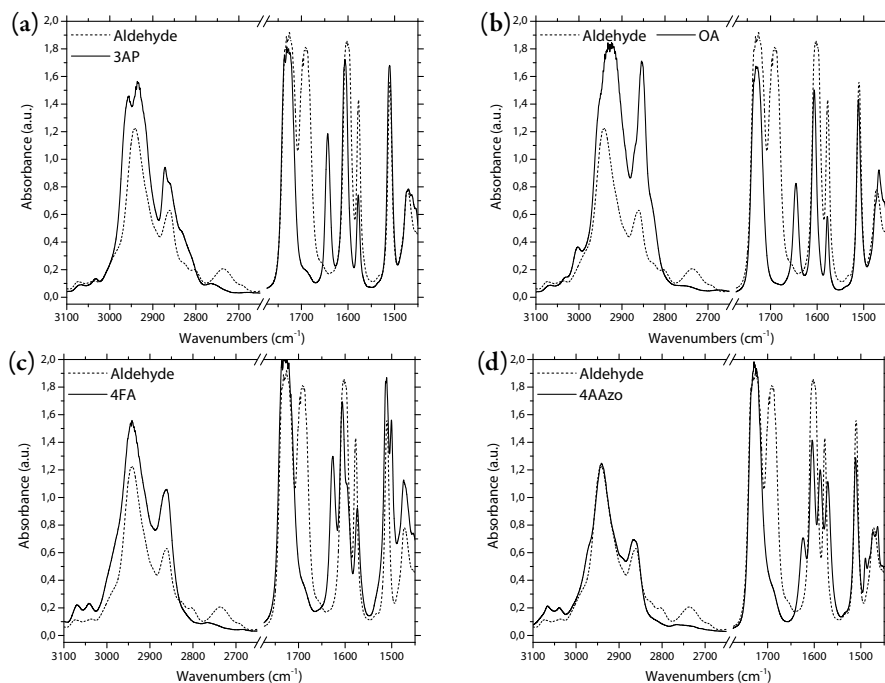


Figure 2.5: Formation of imine functional networks. Transmission FTIR spectra of the aldehyde functional network (short-dash line) and the imine functional products (solid line) of (a) 3-aminopentane (3AP), (b) oleylamine (OA), (c) 4-fluoroaniline (4FA), and (d) 4-aminoazobenzene (4AAzo).

2.2.3 Chemical post-modification

Despite the decrease in order, the aldehyde functional polymer network obtained was exposed to various amines to obtain new imine functionalities. In order to facilitate the reaction a catalytic amount of acetic acid was added to the reaction mixture. Three different aliphatic amines; 3-aminopentane (3AP), 2-aminooctane (2AO), and oleylamine (OA), and two aromatic amines; 4-fluoroaniline (4FA) and 4-aminoazobenzene (4AAzo) were used to study the pore modification (Figure 2.1, route *ii*). Small pieces of the aldehyde functional film were placed in a solution of 500 mM amine and 100 mM acetic acid, and shaken overnight at room temperature. Infrared spectroscopy was performed on the chemically modified films (Figure 2.5). From the FTIR spectra, one can observe a nearly complete disappearance of the aldehydic carbonyl ($\tilde{\nu} = 1690 \text{ cm}^{-1}$) and C-H ($\tilde{\nu} = 2740 \text{ cm}^{-1}$) vibrations. Furthermore, new signals from the formed imine can be observed at either 1645 cm^{-1} or 1625 cm^{-1} for aliphatic (Figure 2.5a and 2.5b) or aromatic (Figure 2.5c and 2.5d) imines, respectively. This result indicates that re-

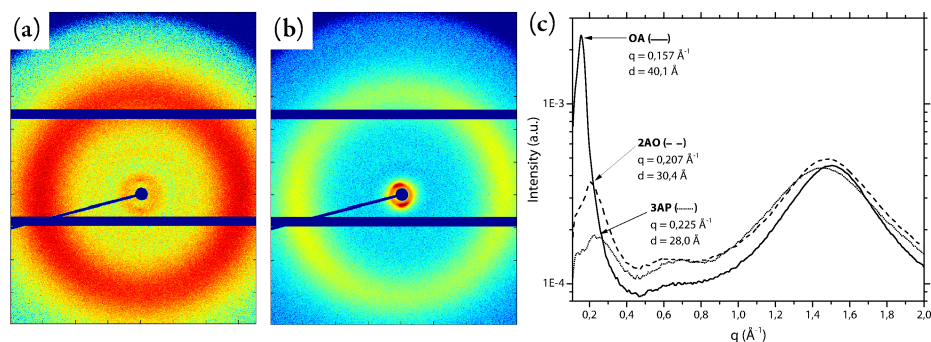


Figure 2.6: X-ray diffraction of the imine functional films. (a) and (b) 2D x-ray diffractograms of 3AP and OA-imine functional films, respectively. (c) Azimuthal integrated profiles of 3AP, 2AO and OA-imine functional films.

Regardless of the type; aliphatic or aromatic, or size, a quantitative functionalization of the aldehyde pores is obtained, and that the network is sufficiently flexible to adapt to the guest molecules which can be up to twice the molecular weight of the initial 4-(2-aminoethyl)aniline template. This latter observation can be explained by considering that the reaction was carried out in THF, in which the network swells. Most remarkably, the lamellar structure was recovered after the imine interior was obtained, and even more interesting, the layered nanostructure adapts to the size of the amine provided. XRD measurement of the dry films demonstrate that a layer spacing of 28 \AA and 30 \AA was observed for the imine interiors of 3AP and 2AO, respectively, while for the much larger OA, with roughly twice the molecular weight of the initial diamine template, a layer spacing of 40 \AA was found. Possibly, the long and flexible aliphatic chains of the interdigitate with the aliphatic side-chains of the mesogenic moieties since a relatively small layer spacing and a significantly higher scattering intensity is observed.

The selectivity of the imine formation to size and reactivity was evaluated by two experiments. In these experiments, an aldehyde functional film was introduced to 10 mL solution of equimolar (250mM) amounts aliphatic and aromatic amines and 100mM acetic acid. In the first experiment, the relatively small 3AP and 4FA were used. In the second experiment 3AP was replaced by the substantially larger OA. The infrared spectra reveal that in both cases the binding of aliphatic amines, regardless of the size, was preferred over aromatic amines indicating that the selectivity is merely based on chemical reactivity (Figure 2.7a and 2.7b). Looking at the chemical differences between aliphatic (3AP

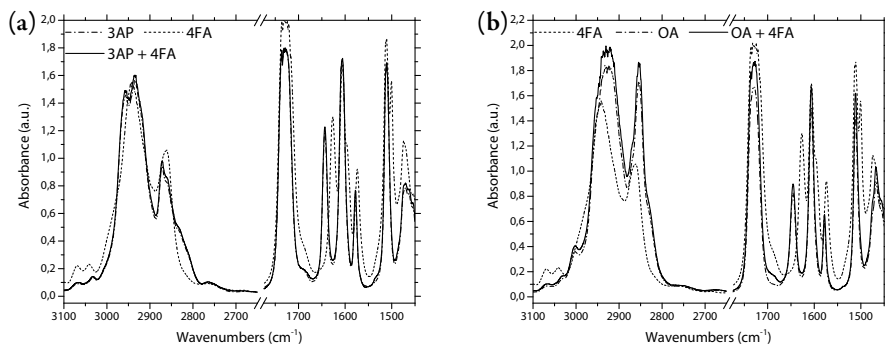


Figure 2.7: Chemical selectivity towards aliphatic amines. (a) Transmission FTIR spectra of a 3AP imine film (dash-dot line), 4FA imine film (short-dash), and a film exposed to equimolar amounts of 3AP and 4FA. (b) Transmission FTIR spectra of a OA imine film (dash-dot line), 4FA imine film (short-dash), and a film exposed to equimolar amounts of OA and 4FA.

and OA) and aromatic (4FA), one can notice that the nucleophilicity (and basicity) of aliphatic amines (pK_a 9–10) is substantially larger than aromatic amines (pK_a 4–5) due to the delocalization of the nitrogen lone pair over the phenyl ring.[20] It is anticipated that under more acidic conditions this equilibrium will shift towards the aromatic species since aliphatic amine will protonate faster than aromatic amines and therefore participating to a lesser extent in the imination reaction.

Another approach to obtain an imine functional interior is by the direct transamination of the bisimine moieties (Appendix, Figure 2.12). This mechanism relies on the exchange of amines without the aldehyde intermediate (Equation 2.2 and Figure 2.1a, route *iii*). In this experiment, identical conditions were used as in route *ii*; small pieces of the bisimine film were placed in a solution of 500 mM amine and 100 mM acetic acid and shaken overnight at room temperature. For all amines, except for 4AAzo, a nearly quantitative conversion of the bisimine moieties to the corresponding mono-imines was obtained. Contrary to the fully converted 4AAzo film that was obtained via route *ii*, which has bright orange color, the color of the obtained 4AAzo film was pale yellow, indicating a low conversion. Indeed, a low conversion was confirmed by FTIR. No significant changes were observed in the spectrum of the 4AAzo-treated film compared to the pristine bisimine film (Appendix, Figure 2.12d). This selectivity can be explained by the fact that the bisimine is fully cross-linked before the reaction and therefore is notably less susceptible to swelling in THF compared to the aldehyde network, making it virtually impossible for the large and rigid 4AAzo moiety to reach the bisimine bonds.

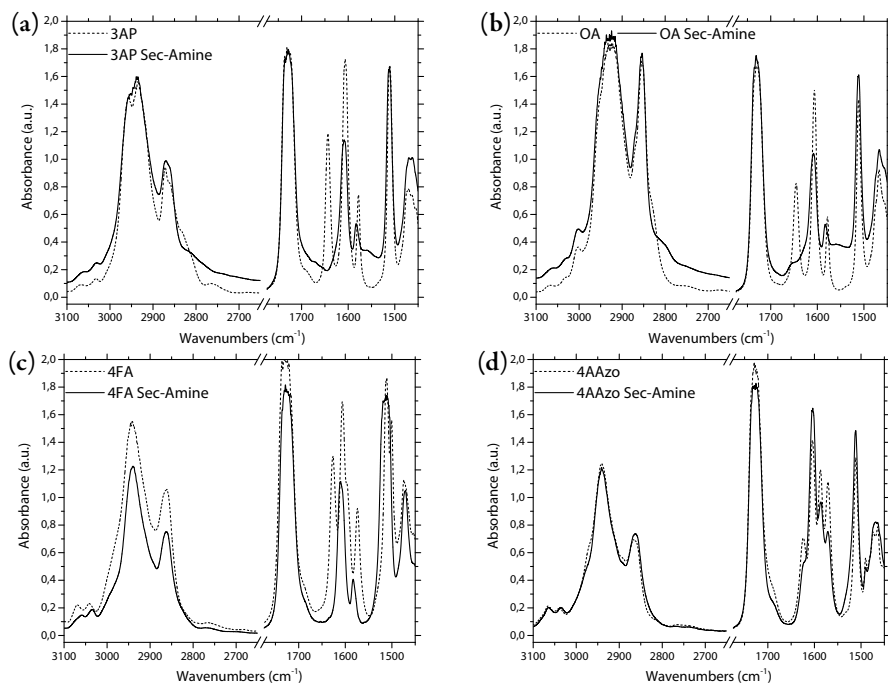


Figure 2.8: Formation of *sec*-amines by reductive amination. (a-d) Transmission FTIR spectra of 3AP, OA, 4FA, and 4AAzo imine films (short-dash line), and its reduced *sec*-amine product (solid line), respectively.

So far, all post-modifications described are dynamic and can still be hydrolyzed or exchanged again, which makes this type of material impractical for the use in an aqueous environment. Therefore, the dynamic imine interior was locked-in by a reductive amination reaction (Figure 2.1a, reaction *iv*). Imines can be reduced to stable secondary amines using sodium triacetoxyborohydride ($\text{NaBH}(\text{AcO})_3$), a milder and less toxic alternative of the commonly used sodium cyanoborohydride (NaBH_3CN).^[21] Small pieces of the imine post-modified films were exposed to a 50 mM sodium triacetoxyborohydride / 75 mM acetic acid solution at room temperature. After 24 hours, the conversion of the imine moieties was measured by infrared spectroscopy (Figure 2.8). By the disappearance of the absorption band at 1645 cm^{-1} (aliphatic imine) or 1625 cm^{-1} (aromatic imine) the conversion of the imine moieties could be confirmed. One can notice that the imines based on 3AP, OA and 4FA could efficiently be converted to secondary amines, while the imine derived from 4AAzo, only reacted partially. This indicates that the reductant could not reach the highly crowded pore surface.

2.2.4 Dye adsorption and release

As a proof of principle, the impact of the post-modification on the materials properties was demonstrated by the release of methyl orange (MO) from the 3AP and OA functionalized polymers. The use of a dye is convenient because of easy visualization. Prior to the desorption experiment, the films were first treated with 0.5 M HCl 1:1 water/THF to create a cationic pore interior by protonation of the *sec*-amine groups. Subsequently, the films containing 3AP and OA based *sec*-amines in their interior, are immersed in a solution containing 1 mg/mL of the MO dye in a 1:1 (v/v) water/THF mixture. The dye concentration is such that there is a large excess when compared to the theoretical maximum capacity of the film to ensure a high level of occupation. The 3AP *sec*-amine film was slightly darker orange compared to the OA film (Figure 2.9b, inset).

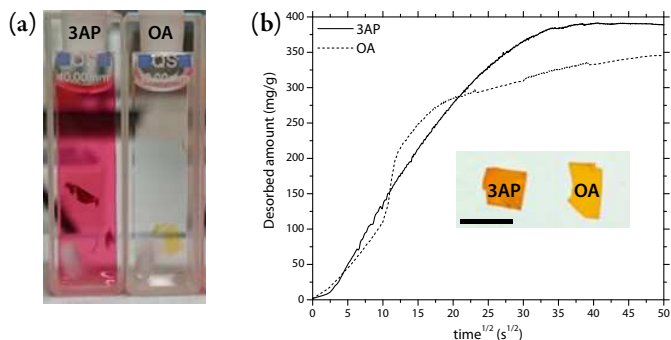


Figure 2.9: Release of MO dye from 3AP and OA *sec*-amine films. (a) Photograph of the release of MO dye in 1 M HCl (aq.). (b) The release of MO from a 3AP film (solid) and OA film (dashed) using 0,5 M HCl 1:1 (v/v) water/THF. Inset: Photograph of the films after dye uptake (Scale bar = 5 mm).

In order to release the dye from the material, the films were placed in cuvettes containing 3 mL 1 M HCl (Figure 2.9a). The film containing the 3AP *sec*-amine directly changed to a dark red color, followed by the release of the dye. The color change of the film indicates that HCl enters the network, protonating the MO dye before it was released. Contrarily, the OA-modified film did not change color and no release was observed. The long and interdigitated aliphatic tails of the oleylamine impede the transport of HCl into the material and accordingly prohibits the release of the dye. However, when 0,5 M HCl in 1:1 (v/v) THF/water was used as the solution, the films swelled and the dye could successfully be released from either of the *sec*-amine networks, although the kinetic profiles of both materials was found to be different (Figure 2.9b). The 3AP film shows a pseudo

Fickian release curve, indicating that the sorption is mainly diffusion controlled, where on the other hand, the OA material shows a two-stage release curve. This behavior is often observed in sorption in glassy polymers where the solvent interacts with the polymer. Such a curve is described as an anomalous transport mechanism where the release is driven by both diffusion and polymer relaxation.[22] The additional disinterdigitation of the aliphatic OA tails inside the lamellae during the swelling in THF/water could be an explanation for this process. These results show that the chemical modification of the nanoporous interior in a polymer can be used to tune release of molecules.

2.3 Conclusion

A facile method to obtain lamellar nanoporous materials with an adjustable pore interior by using dynamic covalent imine chemistry was demonstrated. The reversibility of the chemical bonds makes the system appealing since the pore interior can be tuned on demand by *in situ* chemical modification. The obtained porous material is highly adaptive to the amine that is used to functionalize the pore interior. Indeed, amines with up to double the molecular weight of the initial diamine template could be incorporated. Such results can potentially be used to control the size and chemical nature of the pores and the set of molecules and ions that can be separated by polymers. Finally, the dynamic character of the chemical bond in such polymers gives opportunities to create reusable and cleanable nanoporous materials.

2.4 Experimental section

2.4.1 Materials

4-(6-Hydroxyhexyloxy)benzaldehyde was kindly provided by Philips Research. 4-((6-(Acryloyloxy)hexyl)oxy)benzoic acid was synthesized by Synthron Chemicals GmbH & Co. KG. Methacryloylchloride (97%), 4-(2-aminoethyl)aniline (97%), and 3-pentylamine (97%) were obtained from Sigma Aldrich. Triethylamine (TEA, 99%) was obtained from Acros. All Solvents used were Analytical Grade and obtained from Biosolve. Dry ethanol was prepared by storing it overnight over 3Å molecular sieves (activated in an oven at 600 °C). 1 M HCl (aq.) was freshly prepared from a 37% HCl solution obtained from Sigma Aldrich. All reagents were used as received, without further purification.

2.4.2 Characterization

Magnetic nuclear resonance were performed on a 400 MHz Agilent Technologies 400-MR NMR Spectrometer. Infrared spectroscopy was performed on a Varian 670 IR spectrometer equipped with a microscopy setup over a range of 4000-650 cm^{-1} with a spectral resolution of 4 cm^{-1} and 100 scans per spectrum. Polarized light microscopy was performed on a Leica DM 4 P optical microscope equipped with polarization filters. Linkam TMS 600 hot-stage was used for temperature controlled experiments. Differential scanning calorimetry was performed on a TA Instruments Q1000 calorimeter. The samples were heated and cooled with 5 $^{\circ}\text{C min}^{-1}$ between -40°C and 130°C with a isothermal equilibration of 3 minutes after each heating or cooling ramp. X-ray diffraction experiments were performed on a SAXSLAB GANESHA 300 XL system. UV-Vis spectroscopy experiments were done using a Shimadzu UV-3102 spectrophotometer.

2.4.3 Synthesis

4-(6-methacryloxyhexyloxy)benzaldehyde

6,02 g (27,1 mmol) of 4-(6-hydroxyhexyloxy)benzaldehyde and 9,4 mL of trimethylamine (67.5 mmol, 2.50 eq.) were dissolved in 60 mL of dichloromethane (DCM). Subsequently, the flask was placed in an ice bath to allow contents to cool down to 0°C . 3.10 mL (31.7 mmol, 1.17 eq.) of methacryloylchloride was added dropwise over a time span of 10 minutes. The reaction was allowed to continue for another hour after which the ice bath was removed. The reaction mixture was stirred for 4h at room temperature. The obtained mixture was washed twice with 60 mL of 1 M HCl (aq) solution and subsequently once with 30 ml saturated NaCl solution and dried over MgSO_4 . The product was passed over a short-plug silica column (DCM) before the solvent was removed by rotary evaporation. Yield 6.28 g pale yellow liquid (21.63 mmol, 80.1%). $^1\text{H NMR}$ (400 MHz, CDCl_3): $\delta = 9.88$ (s, 1H), 7.82 (d, $J = 8.80$ Hz, 2H), 6.98 (d, $J = 8.72$ Hz, 2H), 6.09 (s, 1H), 5.54 (s, 1H), 4.16 (t, $J = 6.61$ Hz, 2H), 4.04 (t, $J = 6.41$ Hz, 2H), 1.94 (s, 3H), 1.84 (m, 2H), 1.72 (m, 2H), 1.50 (m, 4H). $^{13}\text{C NMR}$ (100 MHz, CDCl_3): $\delta = 190.74, 167.45, 164.13, 136.44, 131.94, 129.77, 125.20, 114.70, 68.16, 64.53, 28.92, 28.50, 25.72, 25.64, 18.30$. FTIR (ATR): 2940 (m), 2860 (m), 2735 (w), 1714 (s), 1688 (s), 1638 (w), 1600 (s), 1577 (s), 1577 (s), 1509 (m), 1470 (w), 1453 (w), 1430 (w), 1395 (w), 1315 (m), 1297 (m), 1254 (s), 1215 (m), 1156 (s), 1100 (m), 1010

(m), 858 (w), 835 (m), 814 (m), 735 (m), 702 (w).

4-(2-aminoethyl)aniline core diimine (1)

4,02 g (13,84 mmol) 6-(4-formylphenoxy)hexylmethacrylate and 0,82 mL (6,23 mmol) of 4-(2-aminoethyl)aniline were dissolved in 25,5 mL of dry ethanol (3 Å molecular sieves). A small amount of grinded molecular sieves was added to the mixture. The mixture was heated up to the boiling temperature and refluxed for 90 minutes. Subsequently, the mixture was slowly cooled down to room temperature. Where after it cooled down further to $-20\text{ }^{\circ}\text{C}$. The crystals were filtrated and washed with dry and cold ethanol ($-20\text{ }^{\circ}\text{C}$). The residue was recrystallized twice from ethanol. Yield 3.15 g of off-white solid (4.63 mmol, 74.3 %) ^1H NMR (400 MHz, CDCl_3): $\delta = 8.37$ (s, 1H), 8.09 (s, 1H), 7.81 (d, $J = 8.58$ Hz, 2H), 7.63 (d, $J = 8.52$ Hz, 2H), 7.23 (d, $J = 8.12$ Hz, 2H), 7.12 (d, $J = 8.13$ Hz, 2H), 6.95 (d, $J = 8.54$ Hz, 2H), 6.90 (d, $J = 8.53$ Hz, 2H), 6.09 (s, 2H), 5.54 (s, 2H), 4.16 (m, 4H), 4.00 (m, 4H), 3.83 (t, $J = 7.28$ Hz, 2H), 3.00 (t, $J = 7.34$ Hz, 2H), 1.94 (s, 6H), 1.82 (m, 4H), 1.72 (m, 4H), 1.50 (m, 8H). ^{13}C NMR (100 MHz, CDCl_3): $\delta = 167.49, 161.65, 161.07, 160.83, 159.13, 150.33, 137.49, 136.48, 130.38, 129.72, 129.56, 129.20, 129.00, 125.20, 120.81, 114.62, 114.45, 67.93, 67.85, 64.60, 63.16, 37.17, 29.08, 28.55, 25.79, 25.72, 18.33$. IR (ATR) 2939 (m), 2867 (w), 1710 (m), 1640 (w), 1623 (w), 1605 (m), 1571 (m), 1510 (m), 1474 (w), 1460 (w), 1426 (w), 1419 (w), 1375 (w), 1323 (m), 1302 (m), 1242 (s), 1163 (s), 1109 (m), 1074 (w), 1048 (w), 1013 (m), 975 (w), 959 (w), 937 (m), 886 (w), 832 (m), 816 (m), 801 (m), 729 (w).

Ethane-1,2-diylbis(4,1-phenylene) bis(4-((6-(acryloyloxy)hexyl)oxy)benzoate) (2)

^1H NMR (400 MHz, CDCl_3): $\delta 8.14 =$ (d, $J = 8.9$ Hz, 4H), 7.23 (d, $J = 8.5$ Hz, 4H), 7.12 (d, $J = 8.5$ Hz, 4H), 6.96 (d, $J = 9.0$ Hz, 4H), 6.41 (dd, $J = 17.3, 1.5$ Hz, 2H), 6.13 (dd, $J = 17.3, 10.4$ Hz, 2H), 5.82 (dd, $J = 10.4, 1.5$ Hz, 2H), 4.18 (t, $J = 6.6$ Hz, 4H), 4.05 (t, $J = 6.4$ Hz, 4H), 2.95 (s, 4H), 1.84 (p, $J = 6.5$ Hz, 4H), 1.73 (p, $J = 6.8$ Hz, 4H), 1.57 – 1.42 (m, 8H). ^{13}C NMR (100 MHz, CDCl_3): $\delta = 166.32, 165.06, 163.37, 149.26, 138.99, 132.26, 130.58, 129.40, 128.57, 121.76, 121.61, 114.25, 68.07, 64.48, 37.35, 29.01, 28.56, 25.74, 25.72$.

2.4.4 Methods

Preparation of LC Cells

$30 \times 30\text{ mm}^2$ glass slides were first wiped clean using ethanol, sonicated in ethanol for 20 minutes whereafter they were exposed 20 minutes to a UV-Ozone treatment. A thin

layer of polyimide was applied to the glass slides by spincoating. The coated glass slides were precured at 90 °C for 10 minutes whereafter they were cured at 180 °C for half an hour. After curing, the glass plates were rubbed using a velvet cloth to induce a homogeneous alignment direction. Subsequently the glass slides were glued together using a photopolymerizable glue containing 18 μm beads to obtain a well-defined spacing between the glass plates. The glass plates were glued together with their rub-direction antiparallel.

Preparation of LC Networks

A mixture containing **1** (bisimine) and **2** (cross-linker) in an 8:2 weight ratio was used to prepare liquid crystalline networks. 1 wt% photo initiator (Irgacure 819) and 0,5 wt% inhibitor (TBHQ) was added to perform the photopolymerization. All compounds were dissolved in dichloromethane to obtain a homogeneous mixture. The dichloromethane was removed *in vacuo* after mixing. 18 μm thick films were prepared by capillary suction of the LC-monomer mixture in the melt (125 °C) between two accurately spaced glass slides (LC cell). After filling of the cell, the mixture was cooled with 1 °C/min to 80 °C. Subsequently, the polymerization was performed by UV irradiation using a EXFO OmniCure® S2000 spot UV curing lamp for 900 seconds.

Opening of the pores

After the preparation of the LC network films the films were removed from their cells and cut into squares of approximately 5 × 5 mm² and placed in a freshly prepared 0,5 M HCl in a 50 vol% THF/water mixture. After approx. 20 hours at room temperature (20 °C) the films were transferred to pure THF. The films were replaced into pure THF for at least two times to ensure that all diamine was removed from the polymer film.

Preparation of imine functional interiors

An imine modified interior was obtained by immersing an aldehyde–or bisimine functional film to a 1 M amine solution containing 0,1 M acetic acid in THF and allowing it to react for approx. 20 hours at RT. Subsequently, the films were transferred to pure THF. The THF solution was replaced twice to remove remaining reactants.

Preparation of sec-amine functional interiors

The imines in the interior were reduced to *sec*-amines using sodium triacetoxyborohydride (Na(AcO)₃BH). Imine modified membranes were directly transferred from the amine/acetic

acid solution to a solution containing 50 mM Na(AcO)₃BH / 75 mM acetic acid in THF. After approx. 20 hours at R.T. the films were removed from the solution and transferred to pure THF. The THF was replaced at least two times to ensure all reagents were removed.

2.5 References

- [1] J. S. Beck, J. C. Vartuli, W. J. Roth, M. E. Leonowicz, C. T. Kresge, K. D. Schmitt, C. T. W. Chu, D. H. Olson, E. W. Sheppard, S. B. McCullen, J. B. Higgins, J. L. Schlenker, *J. Am. Chem. Soc.* **1992**, *114*, 10834–10843.
- [2] C. T. Kresge, M. E. Leonowicz, W. J. Roth, J. C. Vartuli, J. S. Beck, *Nature* **1992**, *359*, 710–712.
- [3] A. P. H. J. Schenning, Y. C. Gonzalez-Lemus, I. K. Shishmanova, D. J. Broer, *Liq. Cryst.* **2011**, *38*, 1627–1639.
- [4] T. Ichikawa, M. Yoshio, A. Hamasaki, T. Mukai, H. Ohno, T. Kato, *J. Am. Chem. Soc.* **2007**, *129*, 10662–10663.
- [5] M. Zhou, P. R. Nemade, X. Lu, X. Zeng, E. S. Hatakeyama, R. D. Noble, D. L. Gin, *J. Am. Chem. Soc.* **2007**, *129*, 9574–9575.
- [6] D. L. Gin, R. D. Noble, *Science* **2011**, *332*, 674–676.
- [7] I. Gracia, P. Romero, J. L. Serrano, J. Barberá, A. Omenat, *J. Mater. Chem. C* **2017**, *5*, 2033–2042.
- [8] C. Li, J. Cho, K. Yamada, D. Hashizume, F. Araoka, H. Takezoe, T. Aida, Y. Ishida, *Nat. Commun.* **2015**, *6*, 8418.
- [9] K. Kishikawa, A. Hirai, S. Kohmoto, *Chem. Mater.* **2008**, *20*, 1931–1935.
- [10] H.-K. Lee, H. Lee, Y. H. Ko, Y. J. Chang, N.-K. Oh, W.-C. Zin, K. Kim, *Angew. Chem. Int. Ed.* **2001**, *40*, 2669–2671.
- [11] X. Feng, M. E. Tousley, M. G. Cowan, B. R. Wiesenauer, S. Nejati, Y. Choo, R. D. Noble, M. Elimelech, D. L. Gin, C. O. Osuji, *ACS Nano* **2014**, *8*, 11977–11986.
- [12] C. L. Gonzalez, C. W. M. Bastiaansen, J. Lub, J. Loos, K. Lu, H. J. Wondergem, D. J. Broer, *Adv. Mater.* **2008**, *20*, 1246–1252.
- [13] B. R. Wiesenauer, D. L. Gin, *Polym. J.* **2012**, *44*, 461–468.
- [14] N. Giuseppone, J.-M. Lehn, *Chem. Eur. J.* **2006**, *12*, 1715–1722.
- [15] P. N. W. Baxter, R. G. Khoury, J.-M. Lehn, G. Baum, D. Fenske, *Chem. Eur. J.* **2000**, *6*, 4140–4148.
- [16] A. Ciesielski, M. El Garah, S. Haar, P. Kovaříček, J.-M. Lehn, P. Samorì, *Nat. Chem.* **2014**, *6*, 1017–1023.
- [17] N. Roy, B. Bruchmann, J.-M. Lehn, *Chem. Soc. Rev.* **2015**, *44*, 3786–3807.
- [18] R. Piñol, J. Lub, M. P. García, E. Peeters, J. L. Serrano, D. Broer, T. Sierra, *Chem. Mater.* **2008**, *20*, 6076–6086.
- [19] J. Kušerow, F. Boberg, *J. Prakt. Chem.* **1994**, *336*, 613–616.

- [20] W. M. Haynes, D. R. Lide, T. J. Bruno, *CRC Handbook of Chemistry and Physics: A Ready-Reference Book of Chemical and Physical Data*. OCLC: 957751024, **2017**.
- [21] A. F. Abdel-Magid, K. G. Carson, B. D. Harris, C. A. Maryanoff, R. D. Shah, *J. Org. Chem.* **1996**, *61*, 3849–3862.
- [22] D. A. Bond, P. A. Smith, *Appl. Mech. Rev* **2006**, *59*, 249–268.

Appendix

2.A Phase behavior of the pure compounds 1 and 2

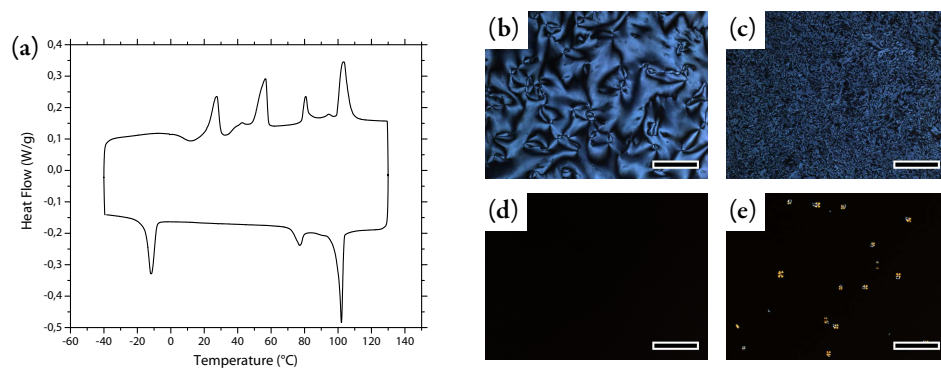


Figure 2.10: Phase behavior of compound 1. (a) DSC thermogram (exothermal down). (b-e) Polarized light micrographs under homeotropic boundary conditions of the mixture at 25 °C (*SmX*), 83 °C (*SmC*), 100 °C (*SmA*), and 116 °C (*I-SmA* transition), respectively. Scale bar = 250 microns.

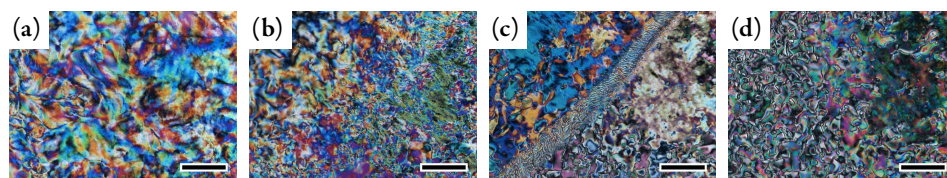


Figure 2.11: Phase behavior of compound 2. (a-d) Polarized light micrographs of the mixture at 80 °C (*Cr*), 125 °C (*SmC-Cr* transition), 155 °C (*N-SmC* transition), and 180 °C (*N*), respectively. Scale bar = 250 microns.

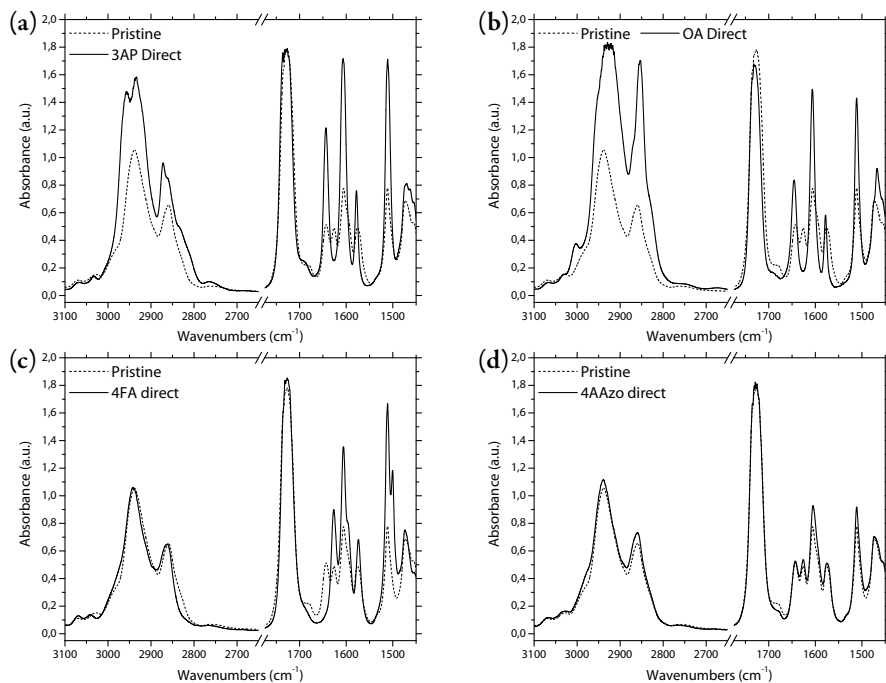
2.B FTIR spectra of films after the transimination reaction (iii)

Figure 2.12: Formation of mono-imines functional films by transimination. (a-d) Transmission FTIR spectra of the pristine bisimine film (short-dash line), and treated 3AP, OA, 4FA, and 4AAzo imine films (solid line), respectively.

Chapter 3

Pyridyl-functional nanoporous LCNs based on H-bonded Heterodimers

Abstract

In this chapter, the development of a nanoporous smectic LCN based on hydrogen bonded heterodimers is presented. This new approach relies on a complex made from a pyridyl moiety hydrogen bonded to a non-reactive benzoic acid porogen. The influence of the crosslink density on the nanostructure of the material was studied during the various steps of the production process. It was found that the lamellar structure was maintained after template removal when 25 wt% or more crosslinker was used. The proton conductivity of the H_3PO_4 -infiltrated nanoporous network was investigated and a high and anisotropic proton conductivity was obtained.

3.1 Introduction

Many of the liquid crystal (LC) derived nanoporous materials are based on hydrogen bonded building blocks (see Chapter 1). Two main approaches are currently used, one based on smectic materials and the second based on columnar LCs. For example, Gonzalez *et al.* described a lamellar (smectic) nanoporous material prepared from dimeric hydrogen bonded benzoic acid derived monomers, where the hydrogen bond themselves act as the porogen.[1] Upon basic treatment, and subsequent cleavage of the hydrogen bonds, the pores are formed. The lamellar structure is maintained by the crosslinker and the pore size is determined by the length of the latter. When working with columnar system a different approach is preferred and, researchers rather privilege the use of a non-reactive hydrogen bonded template. By chemical treatment, the non-reactive part is easily removed and results in straight pores of well-defined dimensions. To date, there is only one known example where this strategy, *i.e.* the use of a porogen template in smectic LCNs, is applied to nanoporous smectic LC materials.[2] But the obtained porous materials was never characterized.

In this Chapter, the development of a chemically adjustable nanoporous LCN based on hydrogen bonded heterodimers is presented. This new approach relies on a complex made from a pyridyl moiety hydrogen bonded to a non-reactive porogen. Upon chemical treatment, the porogen can be removed, resulting in the formation of nanopores. Subsequently, the obtained interior with pyridine groups is exposed, giving more opportunities in term of chemical modifications of the pore interior as compared to previously reported hydrogen bonded systems.[3] Here, the pyridine interior can not only accept hydrogen bonds, but can also be protonated to obtain cationic interior in contrast to the systems based on benzoic acid. Furthermore, this system also allows methylation of the pyridyl nitrogen, which gives access to a permanent charge. This strategy results in a material less sensitive to environmental changes, such as pH. Since the pyridyl pore surface in the nanoporous LCN are basic, phosphoric acid, a popularly used proton conducting material,[4] can be infiltrated into the anisotropic lamellae. The anisotropy of the pore is expected to induce a linear conduction of protons across the thickness of the film.

The approach is inspired by the work of Kato *et al.*, which describes a straightforward method to create hydrogen bonded liquid crystals based on stilbazole chemistry. They

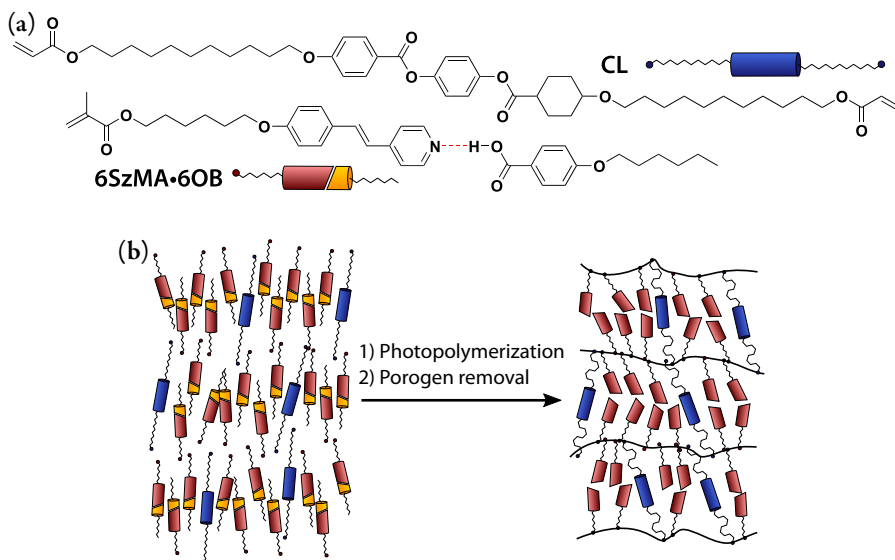


Figure 3.1: The fabrication of the nanoporous smectic LCN from the hydrogen bonded heterodimers. (a) Chemical structures of the monomer mixture containing the hydrogen bonded 6SzMA•6OB monomer and the crosslinker (CL). (b) Schematic representation of the monomer mixture and the nanoporous smectic LCN.

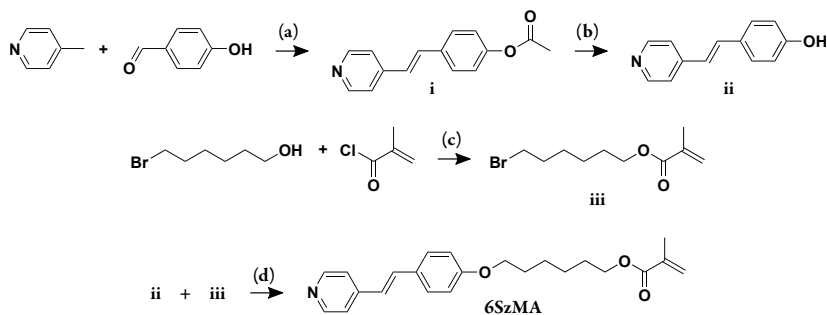
have reported that those complexes induce smectic mesophases, which is of interest in the context of this research.[5] To create a polymeric material, we have equipped the stilbazole moieties with methacrylate reactive end-groups. Yet, to maintain the structure, a cross linker is needed, as discussed in the previous chapter. It is known that the length of the cross linker influences the size of the pores, therefore, a spacer longer than at least two stilbazole units is required to prevent overlapping of the moieties and consequently pores can be obtained (Figure 3.1).

In sections 3.2.1–3.2.3, the design and characterization of the system is explored with an emphasis on the influence of the cross link density on the molecular structure during the various fabrication steps. In section 3.2.4 the use of the nanoporous material for anhydrous proton conduction is investigated.

3.2 Results and discussion

3.2.1 Synthesis and thermal properties of the monomers

The methacrylic 6SzMA monomer was prepared by a 4-step synthesis route (Scheme 3.1). In the first step (a), 4-Acetoxy stilbazole (i) was prepared according to the procedure as



Scheme 3.1: Synthesis of 6SzMA. (a) 4 Å molecular sieves, Ac₂O, reflux 48h, Yield: 79 %. (b) 1,1 eq. KOH, EtOH, reflux 16h, Yield: 77 %. (c) Triethylamine, DCM, -20 °C–r.t. 16h, Yield: 57 %. (d) 3 eq. Cs₂CO₃, 4 Å molecular sieves, DMF, r.t. 24h, Yield: 86 %.

described by Shaw *et al.* and Chiang *et al.*[6, 7] It was found that by adding of a small amount of 4 Å molecular sieves to the reaction mixture, side reactions were reduced and the yield increased to more than 70 %. Subsequently, the acetic acid ester **i** was hydrolyzed by reflux in ethanolic KOH yielding 4-hydroxystilbazole (**ii**, reaction (b)). In parallel, 6-bromohexyloxymethacrylate was prepared by the procedure described by Stumpel *et al.*[8] Finally, 6SzMA was obtained by the Williamson etherification reaction (reaction (d)) of **ii** and **iii** using cesium carbonate (Cs₂CO₃) in anhydrous dimethylformamide at room temperature.

Pure 6SzMA did not show any mesogenic properties, only a crystal to isotropic transition at 77 °C was observed. As previously mentioned, liquid crystalline phases can be induced by supramolecular interactions. Therefore, a hydrogen-bonded complex of 6SzMA and 6-hexyloxybenzoic acid (6OB); 6SzMA•6OB, was prepared by dissolving both compounds in an equimolar ratio in DCM and subsequent evaporation of the solvent (Figure 3.2a). The hydrogen bonded 6SzMA•6OB complex was obtained as a crystalline powder. To study the hydrogen bonding, FTIR spectra were taken from both compounds, and the complex. 6OB displays a broad –OH band at 3000 cm⁻¹ overlapping with the sp³ hybridized C–H bands (2860 and 2930 cm⁻¹). The absence of the broad signal at 3000 cm⁻¹ in the 6SzMA•6OB spectrum, and the presence of two new broad peaks centered at 1900 cm⁻¹ and 2480 cm⁻¹, attributed to hydrogen bonded –OH vibrations, confirm the formation of hydrogen bonds between 6OB and the 6SzMA its pyridyl nitrogen.[9]

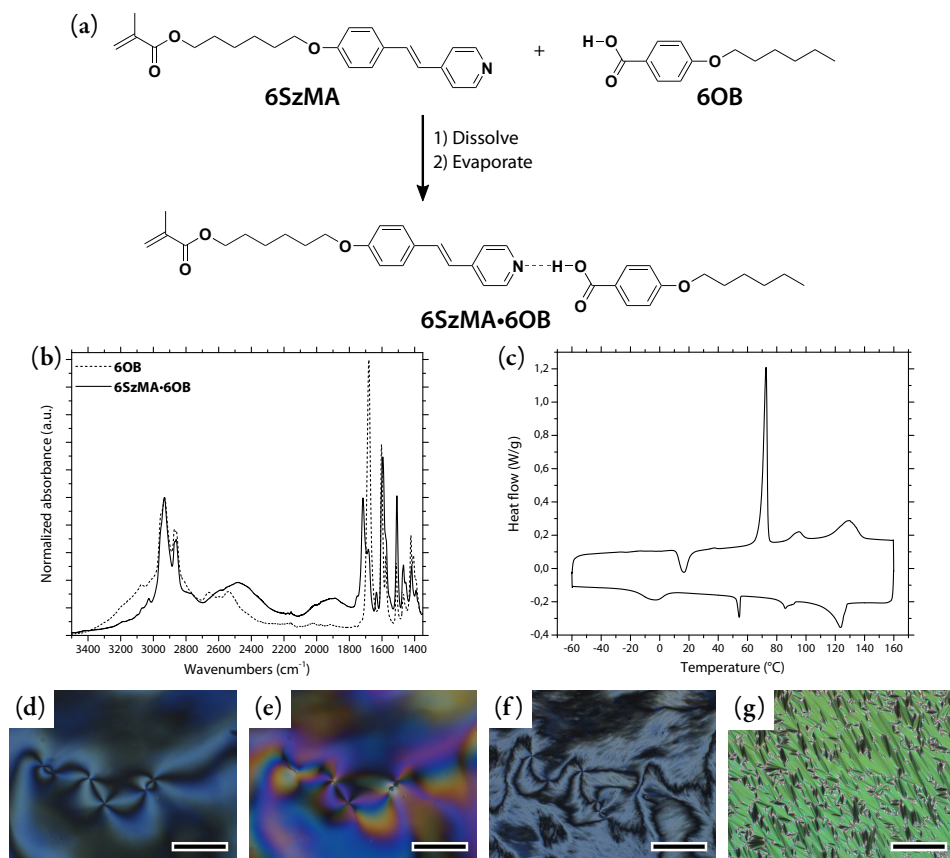


Figure 3.2: Phase behavior of the 6SzMA•6OB complex. (a) The 6SzMA•6OB complex is formed by dissolving 6SzMA and 6OB in DCM and subsequently evaporating the solvent. (b) FTIR spectra of 6OB (short-dash line), and the 6SzMA•6OB complex (solid line). (c) DSC trace of the 6SzMA•6OB complex (exothermal down). (d-g) Polarized light micrographs of the 6SzMA•6OB complex at 30 °C (*SmX*₁), 80 °C (*SmX*₂), and 115 °C (*SmC*) under homeotropic boundary conditions, and 130 °C (*SmA*) under planer boundary conditions, respectively. Scale bar = 250 μm.

Differential scanning calorimetry revealed that 6SzMA•6OB exhibits various liquid crystal transitions (Figure 3.2c). By polarized light microscopy the mesophases were identified by slowly cooling from the isotropic phase (Figure 3.2d–g). The complex forms a SmA mesophase at 140 °C, upon further cooling a SmC mesophase was observed from 119 to 110 °C. Two more higher order tilted smectic mesophases were observed from 80 °C to 62 °C and from 62 °C to –4 °C, whereafter crystallization sets in. Mixtures containing various amounts of crosslinker (CL, Figure 3.1a) were prepared to study the effect of the crosslink density on the order of the porous network in various steps of the

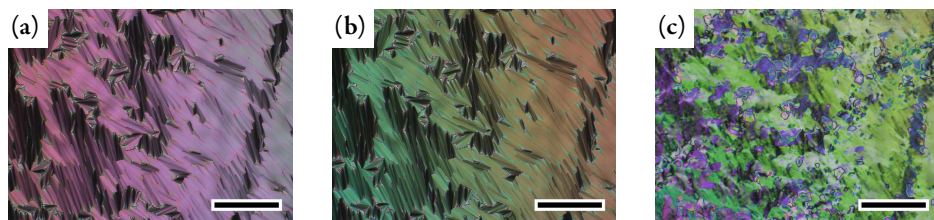


Figure 3.3: Phase behavior of the 6SzMA•6OB complex containing 50 wt% CL. (a-c) Polarized light micrographs of the monomer mixture at 20 °C (SmB), 100 °C (SmA), and 118 °C (N), respectively. Scale bar = 250 μm .

preparation process. The addition of CL led to changes in the phase behavior of the monomer mixture. Increasing the amount of CL resulted in a decreased clearing temperature and the disappearance of tilted smectic mesophases. For example, when 50 wt% CL was used, upon cooling from the isotropic melt, a narrow nematic mesophase was observed at 119 °C—117 °C (Figure 3.3c), a smectic A mesophase from 117 °C to 59 °C (Figure 3.3b), and a smectic B mesophase from 59 °C to -15 °C (Figure 3.3a) indicated by the slightly more homogeneous texture and the observation of transition bands perpendicular to the molecular director at $T_{\text{SmA-SmB}}$ by polarized optical microscopy.

3.2.2 Preparation and characterization of LCNs

Homogeneous planar aligned LCN films with a defined thickness (20 μm) were prepared by photopolymerizing the monomers in home-made LC cells. After UV irradiation for 10 min, the samples were polymerized as was confirmed by the disappearance of the peaks at 1640 cm^{-1} (C=C str. vib.), 1410 cm^{-1} (=CH₂ def. vib.), and 1290 cm^{-1} (=CH rocking vib.) in the FTIR spectrum (Figure 3.4). Furthermore, the alignment of the mesogenic moieties in such material is of eminent importance with regard to the application, since it is anticipated that the initially straight and well defined lamellar structure in the LCN will be directly translated to the subsequent pore structure after the template is removed. The order and alignment of the material was studied by polarized light microscopy and x-ray scattering measurements. From the small angle region of the pristine polymer film x-ray diffractogram, one can see that the smectic layer spacing is strongly influenced by the amount of cross-linker (x_{CL}) present. For films containing 10, 25, and 50 wt% ($x_{\text{CL}} = 8, 20, \text{ and } 42 \text{ mol\%}$) CL, a layer spacing of 4.05, 4.40 and 4.82 nm was found, respectively (Figure 3.5).

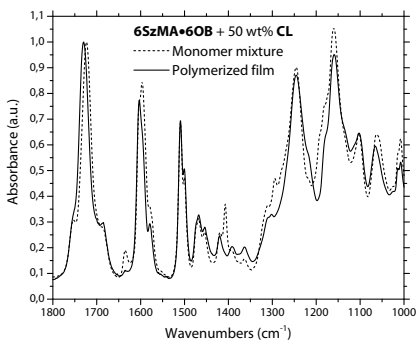


Figure 3.4: Photopolymerization of the mixture containing 6SzMA•6OB and 50 wt% CL. ATR-FTIR spectra of the monomer mixture (short-dash line) and the polymer film (solid line).

In parallel, the molecular length of the monomers in the stretched conformation was estimated by energy minimization using PerkinElmer Chem3D software. A length of 2.26 nm and 3.88 nm was obtained for 6SzMA ($L_{6\text{SzMA}}$) and the hydrogen bonded 6SzMA•6OB ($L_{6\text{SzMA}\cdot 6\text{OB}}$) complex, respectively. Using the same method, the length of CL (L_{CL}) was estimated at 5,44 nm. From literature it is known that the d-spacing of smectic materials, composed a mixture of molecules having different molecular lengths, is directly linked to the d-spacing of the individual compound and their respective amount using Diele's additivity rule.[10–12] The d-spacing of a fluid smectic liquid crystal does not only depend on the molecular length. For example, the conformational disorder and interdigitation of the molecules contribute to a d-spacing that is lower than the molecular length.[13] The Diele's additivity rule is explained by the interdigitation of the mesogen tails, resulting in one average d-spacing. In this system, however, the reactive end-groups of the liquid crystalline monomers are tied together by polymerization, and therefore no interdigitation can occur. It is expected that after the polymerization, the molecules should still exhibit a conformational disorder, and compared to the monomeric state, this disorder can even increase due to polymerization shrinkage.[14] Using this relationship described by Diele *et al.*, and the calculated molecular length of individual molecules (L_i), instead of the d-spacing, the following relation is obtained:

$$d = \sum_{i=1}^n x_i \cdot d_i \approx x_{\text{CL}} \cdot L_{\text{CL}} + x_{6\text{SzMA}\cdot 6\text{OB}} \cdot L_{6\text{SzMA}\cdot 6\text{OB}} \quad (3.1)$$

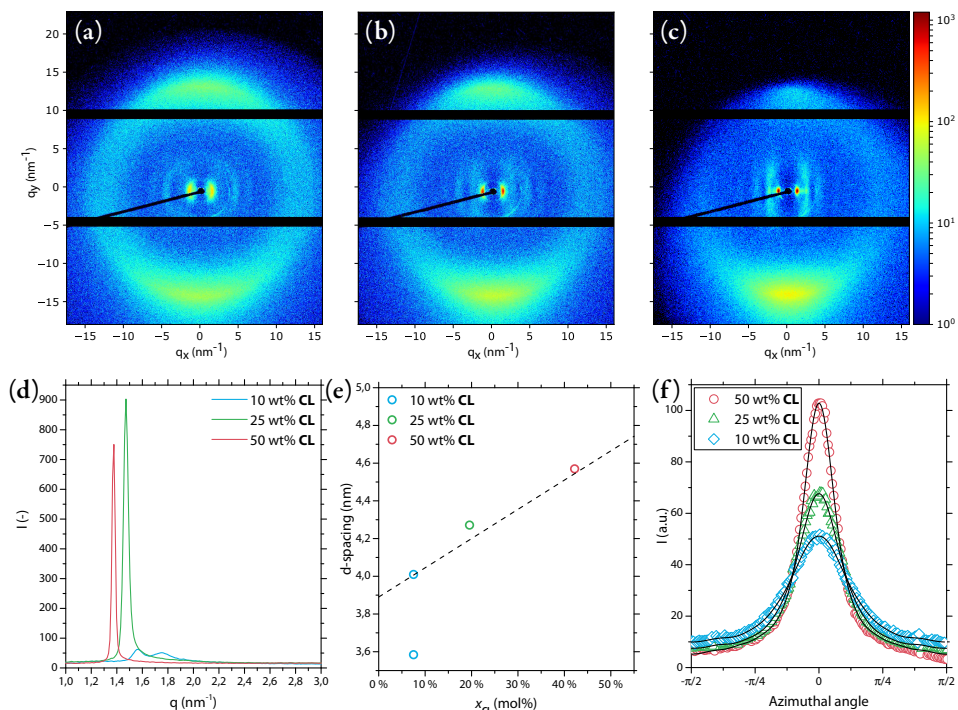


Figure 3.5: Structural characterization of the pristine polymer films. (a–c) 2D x-ray diffractograms of LCNs containing 10, 25, and 50 wt% CL, respectively. N.B. The visible asymmetry and dark region is caused by the partial blocking of the scattered x-rays by the sample holder. (d) Azimuthal integration of the small angle region of the x-ray diffractograms obtained from MAXS measurements. (e) d -spacing as a function of x_{CL} . Dashed line represents $x_{CL} \cdot L_{CL} + x_{6SzM\mathbf{A}\cdot\mathbf{6OB}} \cdot L_{6SzM\mathbf{A}\cdot\mathbf{6OB}}$. (f) Radial integration of the wide angle signal ($q \approx 14 \text{ nm}^{-1}$).

Although this relationship does not include any conformational disorder of the mesogens, one can see that even for crosslinked LCNs this additivity rule holds (Figure 3.5e). It is foreseen that the long and flexible aliphatic spacer of the crosslinker CL can undergo a conformational change to adapt to the 6SzM $\mathbf{A}\cdot\mathbf{6OB}$ molecular length. Remarkably, from the azimuthal integration of the small angle signals at low x_{CL} , the lamellar organization seems very inhomogeneous (Figure 3.5d). The polymer film containing 10 wt% CL displays a weak small angle signal that seems to be split-up and is extremely broad, which might suggest that demixing of 6SzM $\mathbf{A}\cdot\mathbf{6OB}$ and CL occurs. It is anticipated that this is due to the mismatch in the d -spacing and the length of the cross linker, the latter can not undergo the large conformational change necessary to adapt to the lamellar structure.

The effect of the crosslink density on the order of the LCN was then investigated from the wide angle area of the 2D x-ray scattering patterns (Figure 3.5a–c). One can see that the lobes, located at $q \approx 14 \text{ nm}^{-1}$ become narrower and more intense with increasing x_{CL} . This suggests that the orientational order is increasing with increasing CL content and it becomes evident in the radial integration as depicted in Figure 3.5f. In anisotropic soft matter, the orientational order parameter (S_2) describes the tilt deviation of the molecules from the average vector \mathbf{n} . It varies from 1 for perfect orientation and 0 for an isotropic orientation. S_2 can be determined from the scatter intensity by fitting with a series of $\cos^{2i}(\theta)$ using Legendre polynomials as described by Davidson *et al.*[15] The radial integration curves were fitted from $\theta = -0.5\pi$ to 0.5π with the max intensity located at $\theta = 0$ (Figure 3.5f). Using this method, S_2 -values of 0.90, 0.73, and 0.58 were obtained for the LCNs containing 50 wt%, 25 wt%, and 10 wt% CL. Those results are consistent with the expectation that a higher amount of CL helps to maintain alignment and order within the LCN. However, this latter would also mean that there should be an offset between the actual measurements and the molecular length based Diele's additivity rule, since a lower orientational leads to a lower d-spacing.

3.2.3 Template removal

In order to obtain the porous structure, the **6OB** template was removed from the network. In the FTIR spectrum, signals at 2500, 1920, and 1680 cm^{-1} disappeared, indicating the breakage of the hydrogen bonds. Furthermore, the relative decrease in intensity of the $\text{sp}^3 \text{ C-H}$ bands located at 2930 and 2855 cm^{-1} indicate that aliphatic material (**6OB** tail) was removed from the LCN. The quantitative removal of **6OB** was confirmed by weighing small pieces of film before and after the treatment. Indeed, the weight loss measured corresponds to the initial mass of **6OB** added to the mixture, as seen in Figure 3.6c.

Because the amount of **6OB** removed from the system is substantial, one can expect the dimensions of the film to be influenced. Therefore, the macroscopic dimensional changes of the film after removal of **6OB** and drying of the film were monitored. Perpendicular to the molecular director, a small expansion (1,8 – 3,4 %) was observed. However, parallel to the molecular director a more significant contraction of the film was noticed (Figure 3.6d). The contraction is highly dependent on the concentration CL

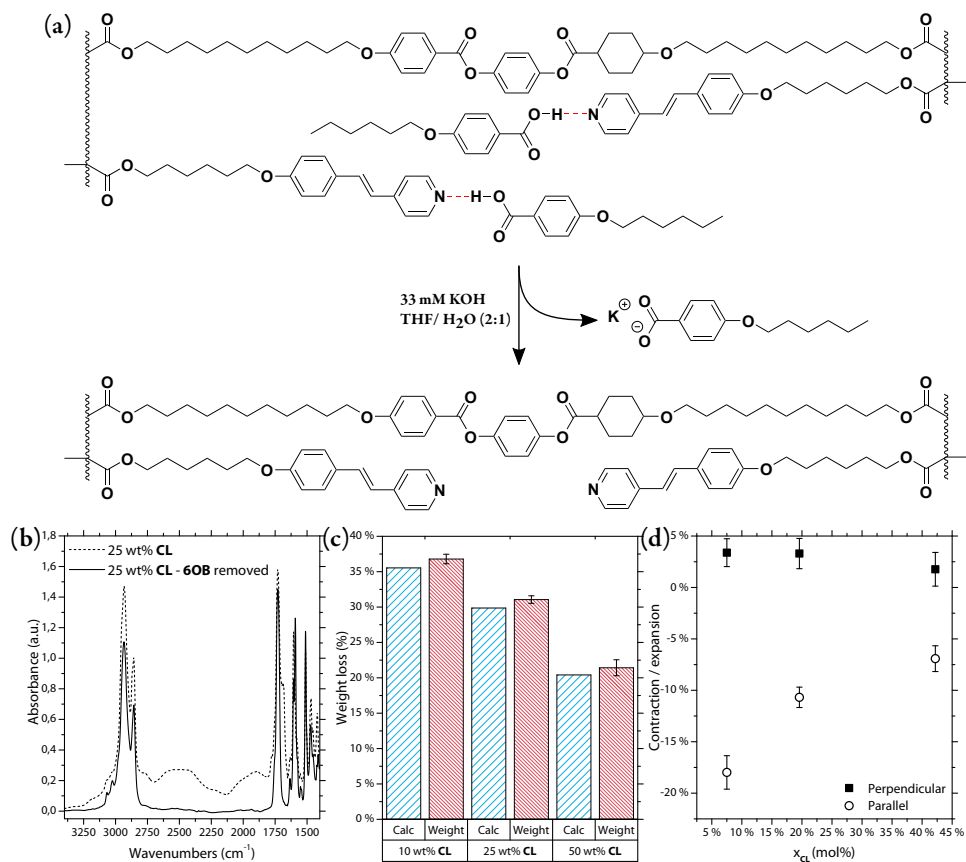


Figure 3.6: Removal of the 6OB template. (a) Reaction scheme of the removal of the 6OB porogen. (b) FTIR spectra of a pristine LCN containing 25 wt% CL (short-dash line) and the same film after removing 6OB template (solid line). (c) Calculated and measured relative weight loss of the samples after removing the 6OB template of samples containing 10, 25, 50 wt% CL. (d) Macroscopic geometrical changes of the samples containing 10, 25, 50 wt% CL, respectively, after removing the 6OB template.

present (x_{CL} , mol%), and for the films containing 10 wt%, 25 wt% and 50 wt% CL a contraction of 18 %, 11 % and 7 % along \mathbf{n} was measured. Considering the estimated molecular length of the individual compounds, this proves the ability of the crosslinker to maintain the structure of the film to a certain extent, even after removal of the template.

XRD measurements were also performed to investigate the impact of the 6OB removal on the microscopic structure of the material. For the sample containing only 10 wt% CL, no layer spacing could be observed indicating that either the lamellar structure within

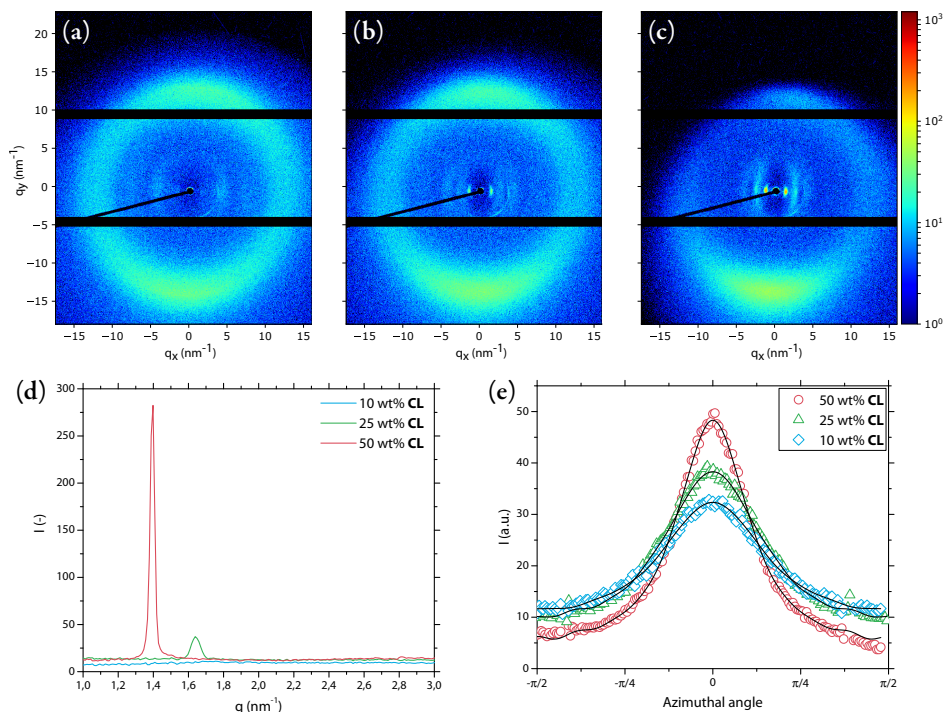


Figure 3.7: Structural characterization of the nanoporous polymer films after 6OB removal. (a-c) 2D x-ray diffractograms of nanoporous LCNs containing 10, 25, and 50 wt% CL, respectively. (d) Azimuthal integration of the small angle region of the x-ray diffractograms. N.B. The visible asymmetry, and dark region is caused by the sample holder blocking the signal partially. (e) Radial integration of the wide angle signal ($q \approx 14 \text{ nm}^{-1}$).

the LCN was lost or that a too weak electron density gradient along the molecular director was obtained due to the collapse of the pores. A d-spacing of 3.98 and 4.47 nm were obtained for the materials consisting of 25 and 50 wt% CL, respectively, corresponding to a decrease in layer spacing of 9.5 and 7.2 %. These numbers indicate that the removal of the 6OB led to a partial collapse of the microscopic lamellar structure. Interestingly, the d-spacing of the film containing 50 wt% CL is roughly twice the length of a 6S_zMA moiety (2.26 nm), indicating a head-to-head organization while the sample containing 25 wt% CL, has a spacing smaller than the length of two 6S_zMA moieties, revealing a slight interdigitation. These results show that for crosslink density above 25 %, the internal lamellar structure can be preserved despite a decrease of the orientational order of the materials after removal of the 6OB moiety. From the radial integration of the wide angle XRD signal (Figure 3.7e), the orientational order parameter S_2 was estimated, and

values of 0.37, 0.48, and 0.78 for 10, 25, and 50 wt% CL, respectively, were obtained.

3.2.4 Anhydrous proton conduction

With the nanoporous material at hand, a potential application as proton conducting material was investigated. There are different approaches to obtain enhanced proton conductivity in polymeric materials.[16–18] This includes the use of hybrid (organic/inorganic) polymers or aligned proton conducting pathways. Such a hybrid membrane can be obtained from the above discussed material by infiltration of an inorganic acid after the 6OB porogen is removed. Since the pyridyl pore surface in the nanoporous LCN is basic, phosphoric acid, a popularly used proton conducting material,[4] can be infiltrated into the anisotropic lamellae. The anisotropy of the pore is expected to induce a high proton conductivity across the thickness of the film.

Before exposing the nanoporous LCNs to the phosphoric acid, the pKa of the pyridine was determined to verify that protonation can occur. To determine the pH at which the pyridine moieties are protonated the films were immersed in buffered 1 M NaCl solutions of pH 1 to 6. Visually, a color change from nearly colorless to bright yellow was observed for the films held in low pH solutions (typically < pH 3), indicating the protonation of the stilbazole.[19] After 16 hours, the films were removed from the solutions and measured by FTIR to obtain quantitative information (Figure 3.8). A broad peak centered at 2600 cm^{-1} (attributed to the N–H bond) appeared and was followed to monitor the protonation.

Materials containing 10 and 25 wt% CL had a similar pKa (~ 3.1), while for the material containing 50 wt% CL, a pKa of roughly 1.8 was estimated. It is known from literature that the monomeric, has a pKa of 4.7. This suggests that the cross-linked network influences the ability to protonate the pyridyl nitrogen. Both films containing 10 wt% and 25 wt% CL are easily protonated and display a high capacity (2.32 and 1.78 mmol g^{-1} , respectively) as compared to the 50 wt% CL sample (1.05 mmol g^{-1}). However, the mechanical (by handling) and structural properties of the nanoporous LCNs film containing 10 wt% CL are poor compared to the 25 wt% CL films. Therefore, based on these results, only the 25 wt% CL films were used for further investigation.

Infiltration of the phosphoric acid in the pores was achieved by exposing the nanoporous LCN films to a 100 mM H_3PO_4 solution in either pure THF or a 1:1 (v/v) THF/water

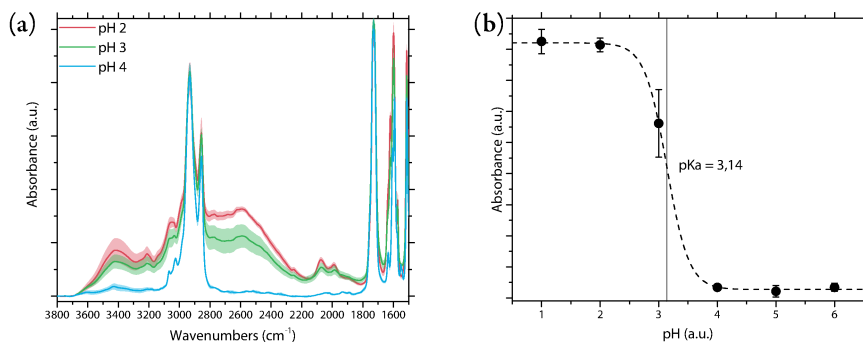


Figure 3.8: pK_a determination of the nanoporous LCN containing 25 wt% CL. (a) FTIR spectra of a nanoporous LCN exposed to 1 M NaCl (aq.) solutions of pH 2 (red line), 3 (green line), and 4 (blue line). (b) Estimation of the pK_a from the absorbance at 2600 cm^{-1} for films exposed to 1 M NaCl (aq.) at various pH values.

mixture. After exposure, the obtained films were examined using transmission FTIR spectroscopy (Figure 3.9a). A broad peak was observed ranging from 3400 cm^{-1} to 2000 cm^{-1} , originating from the stilbazolium $\text{N}^+\text{-H}$ and phosphoric acid -OH vibrations. Furthermore, the films that were infiltrated with phosphoric acid using pure THF as solvent show a higher absorbance than films where a THF/water mixture was used, indicating a higher degree of occupation. From Figure 3.9b one can see that when using pure THF, and assuming only electrostatic interactions (1.78 mmol/g), an occupation level of 2.54 equivalents H_3PO_4 was obtained. It is known that phosphoric acid can form strong intermolecular hydrogen bonds in solution, therefore hydrogen bonded H_3PO_4 clusters could be incorporated, explaining the high degree of occupation. When a 1:1 (v/v) THF/water mixture was used, an occupation level of 1.06 equivalents H_3PO_4 was obtained. This suggests that the addition of water, led to a lower degree of occupation by promoting the dissociation of the hydrogen bonds between H_3PO_4 molecules in solution.

The proton conductivity was measured using electrochemical impedance spectroscopy (EIS). The impedance spectrum resembles the equivalent circuit containing an interfacial capacitance (CPE_1), the sample field capacitance (CPE_2), and the sample resistance (Figure 3.10a). At each given temperature, the resistance (R_b) was estimated from the intersection of the real axis (Z') and the semicircle of the impedance spectrum. The proton conductivities σ (S cm^{-1}) by $\sigma = d/R_b A$, where d (cm) is the thickness of the film, A (cm^2) is the area of the film.

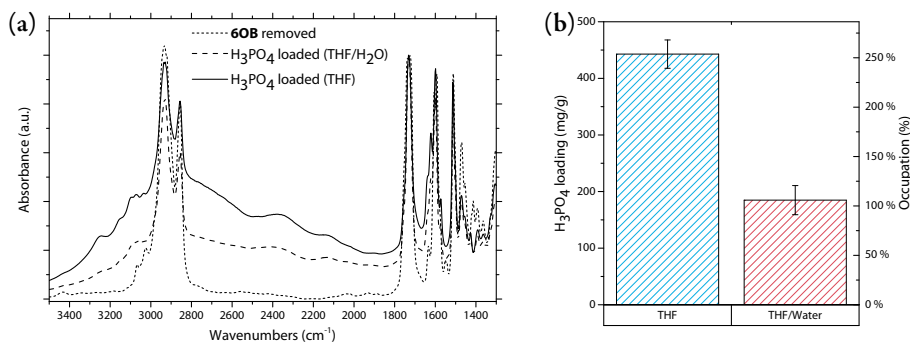


Figure 3.9: Infiltration of H_3PO_4 in a nanoporous film containing 25 wt% CL. (a) FTIR spectra of nanoporous LCN films: Unexposed (short-dash line), 100 mM H_3PO_4 in 1:1 (v/v) THF/Water (dashed line), and 100 mM H_3PO_4 in THF (solid line). (b) Gravimetrically determined H_3PO_4 uptake in films exposed to 100 mM H_3PO_4 in 1:1 (v/v) THF/Water (right column), and 100 mM H_3PO_4 in THF (left column).

The proton conduction of planar aligned LCNs containing 1.06 eq. H_3PO_4 , 2.54 eq. H_3PO_4 , and the initial 6OB porogen (control) are depicted in Figure 3.10b. One can notice that the conductivity increases as the temperature is risen. The Arrhenius behavior (linear on the $\log(\sigma)$ versus T^{-1} (K) scale) of this curve implies that the proton conduction is dominated by the “hopping” (Grotthuss) mechanism.[20] The conductivity of LCNs containing 1.06 eq. and 2.54 eq. H_3PO_4 reaches a maximum of about $3 \times 10^{-5} \text{ S cm}^{-1}$ and $8 \times 10^{-4} \text{ S cm}^{-1}$ at 170 °C, respectively. This is a great enhancement compared to the 6SzMA•6OB LCN, that reached a maximum conductivity of only $2 \times 10^{-8} \text{ S cm}^{-1}$ at the same temperature. The easy dissociation of the triprotic H_3PO_4 , and the strong intermolecular hydrogen-bonding between the acid moieties, enable the efficient proton transport, explaining the enhancement of the proton conductivity. It is anticipated that, besides the enhanced conductivity, the excess of phosphoric acid present in the films containing 2.54 eq. H_3PO_4 gives rise to a higher concentration of readily ionizable protons, since the “non-complexed” phosphoric acid is more acidic ($\text{pK}_a = 2.1$) than the conjugate acid of the 6SzMA moieties inside the porous network containing 25 wt% CL ($\text{pK}_a \approx 3.1$).

To demonstrate that the membrane really benefits from the straight pores through the thickness of the film, homeotropic aligned films were prepared to have the pores oriented parallel to the electrodes. A comparable degree of occupation was achieved using the H_3PO_4 infiltration methods mentioned before. In Figure 3.10c one can see the proton

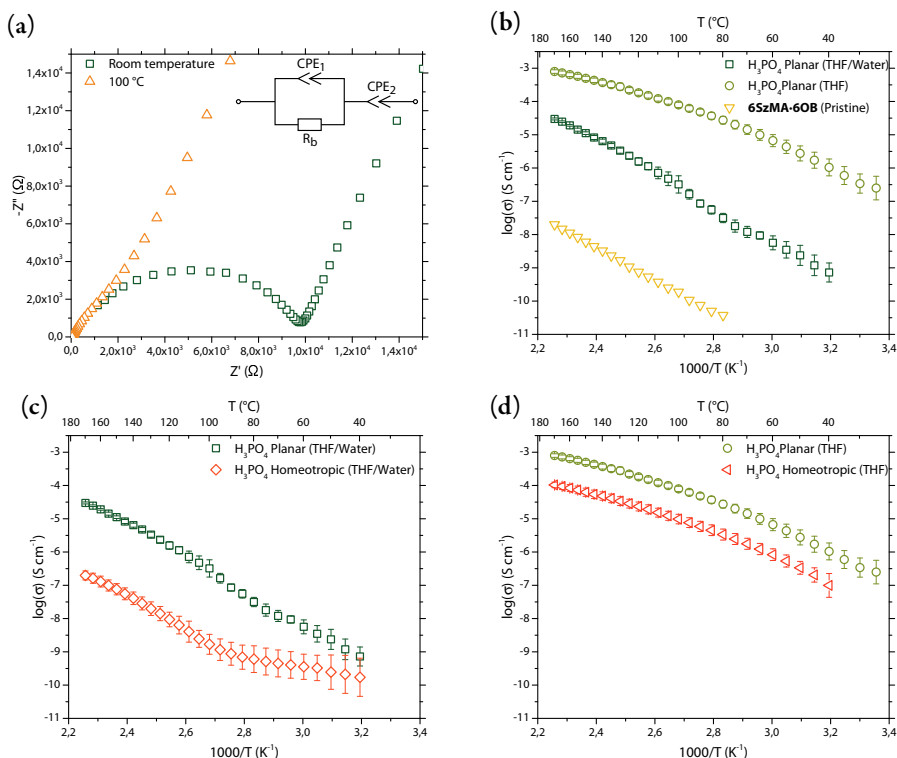


Figure 3.10: Proton conduction of H_3PO_4 infiltrated films containing 25 wt% CL. (a) Nyquist plot of films containing 2.54 eq. H_3PO_4 at room temperature and 100 °C. (b) Anhydrous proton conduction in a planar aligned pristine (6SzMA-6OB) film (yellow open triangles), and planar aligned nanoporous films containing 1.06 eq. H_3PO_4 (dark green open squares), and 2.54 eq. H_3PO_4 (light green open circles), respectively. (c) Anhydrous proton conduction in planar (dark green open squares), and homeotropic aligned (red open diamonds) nanoporous films containing 1.06 eq. H_3PO_4 . (d) Anhydrous proton conduction in planar (light green open squares), and homeotropic aligned (red open triangles) nanoporous films containing 2.54 eq. H_3PO_4 .

conduction in both planar and homeotropic aligned films containing 1.06 equivalents of H_3PO_4 . At high temperatures, the proton conduction in homeotropic aligned films was two orders of magnitude lower than when using planar aligned films, indicating that the orientation of the pores contributes to the high conductivity. This is due to the fact that the pathways in the planar membrane are parallel to the direction of electric field, therefore the protons can travel in a straight line between two electrodes. In contrast, in the homeotropic aligned membranes, the polymer layers act as insulating layers, hindering the traveling protons. Peculiarly, the temperature dependence of the conductivity did not show Arrhenius behavior. At low temperature, only a moderate increase in con-

duction is observed. This is most likely because the protons have to cross the polymeric layers as mentioned above. However, once passed the ~ 100 °C, the protons can more easily cross this barrier. Thereafter, the temperature dependance of the conduction is similar to the planar sample, yet, at lower conductivity. This implies indeed that the transport of protons through straight pores is preferred, as anticipated.

The proton conduction of the homeotropic films containing 2.54 equivalents of H_3PO_4 (Figure 3.10d) was measured too. Despite a higher conductivity for the planar sample, the difference in proton conductivity with the homeotropic aligned films was substantially smaller than when 1.06 equivalents H_3PO_4 were used. In contrast to the films with a lower occupation discussed before, here both films show the same temperature dependence curve with a one order of magnitude difference in conductivity, indicating that the orientation of the anisotropic pores play a less important role. It is expected that the excess of phosphoric acid can cross polymeric layers, facilitating the transport of protons across.

3.3 Conclusion

The fabrication of nanoporous smectic liquid crystal networks containing pyridyl moieties has been described. The influence of the crosslink density on the nanostructure of the material was studied during the various steps of the production process. It was found that the structure was maintained after template removal when 25 wt% or more crosslinker was used. The proton conductivity of the H_3PO_4 -infiltrated nanoporous network was investigated. A high and anisotropic proton conductivity was obtained, and when a large excess of H_3PO_4 was present, the conductivity was even further enhanced.

3.4 Experimental section

3.4.1 Materials

6-Bromohexan-1-ol (> 95 %) was obtained from TCI Europe N.V., triethylamine (99 %) was obtained from Acros. Methacryloyl chloride (97 %), 4-methylpyridine (98 %), 4-hydroxybenzaldehyde (98 %), acetic anhydride (≥ 99 %), and cesium carbonate (99 %) were obtained from Sigma Aldrich. Trans-4-(4-(11-acryloyloxyundecyloxy)cyclohexanecarboxyloxy)phenyl-4-(11-acryloyloxyundecyloxy)benzoate (CL) was obtained from Synthon Chemicals GmbH & Co. KG. All Solvents used were Analytical Grade and

obtained from Biosolve. Dry ethanol was prepared by storing it overnight over 3 Å molecular sieves (activated in an oven at 600 °C). 1 M HCl (aq.) was freshly prepared from a 37 % HCl solution obtained from Sigma Aldrich. All reagents were used as received, without further purification.

3.4.2 Characterization

Magnetic nuclear resonance were performed on a 400 MHz Agilent Technologies 400-MR NMR Spectrometer. Infrared spectroscopy was performed on a Varian 670 IR spectrometer equipped with a microscopy setup over a range of 4000-650 cm^{-1} with a spectral resolution of 4 cm^{-1} and 100 scans per spectrum. Polarized light microscopy was performed on a Leica DM 4 P optical microscope equipped with polarization filters. Linkam TMS 600 hot-stage was used for temperature controlled experiments. Differential scanning calorimetry was performed on a TA Instruments Q1000 calorimeter. The samples were heated and cooled with 5 °C min^{-1} between -40 °C and 130 °C with a isothermal equilibration of 3 minutes after each heating or cooling ramp. X-ray diffraction experiments were performed on a SAXSLAB GANESHA 300 XL system. UV-Vis spectroscopy experiments were done using a Shimadzu UV-3102 spectrophotometer.

Anhydrous proton conduction

Electrochemical impedance spectroscopy (EIS) was recorded on an Autolab potentiostat equipped with a hostage in the frequency range from 1 Hz to 1 MHz (applied voltage: 10 mV). Gold electrodes of a set area (0.28 cm^2) were applied on both sides of the polymeric films. The conductivities were measured as a function of temperature between room temperature (22 °C) and 170 °C with 5 °C intervals. Before the measurements, the polymer films were vacuum dried overnight.

The impedance spectrum can be modeled as an equivalent circuit and divided into imaginary (Z'') and real (Z') components. The resistance (R_b) was estimated from the intersection of the real axis (Z') and the semicircle of the impedance spectrum. The proton conductivities σ (S cm^{-1}) are calculated using the following equation:

$$\sigma = \frac{d}{R_b A} \quad (3.2)$$

Where d (cm) is the thickness of the film, A (cm²) is the area of the film and R_b (Ω) is the resistance of the sample to conduction .

3.4.3 Synthesis

4-hydroxy-4-stilbazole (ii)

The synthesis of the 4'-hydroxy-4-stilbazole has been carried out according a literature procedure.[6, 7] The only change from the procedures was the addition of a small amount of 4 Å molecular sieves to the reaction mixture. Yield: 78.9 %. mp 78–80 °C; ¹H NMR (400 MHz, CDCl₃) δ : 1.50 (m, 4H, CH₂), 1.72 (q, 2H, J = 14.0 Hz), 1.82 (q, 2H, J = 13.8 Hz), 1.95 (s, 3H), 3.99 (t, 2H, J = 6.5 Hz), 4.15 (t, 2H, J = 6.5 Hz), 5.55 (m, 1H), 6.10 (m, 1H) 6.87 (d, 1H, J = 15.4 Hz) 6.90 (d, 2H, J = 8.7 Hz), 7.25 (d, 1H, J = 16.3 Hz), 7.33 (d, 2H, J = 6.1 Hz), 7.47 (d, 2H, J = 8.7 Hz), 8.55 (d, 2H, J = 6.1 Hz). ¹³C NMR (400 MHz, CDCl₃) δ : 167.6, 159.7, 150.3, 150.1, 145.0, 136.6, 132.9, 128.8, 128.5, 128.3, 125.4, 125.2, 120.8, 120.5, 114.9, 114.8, 67.9, 64.7, 29.2, 28.6, 25.9, 25.8; FTIR (cm⁻¹): 3071, 3036, 2943, 2899, 2886, 1701, 1594, 1514, 1169, 1023, 873, 545; MS m/z . 366.13 (M+H⁺) (calculated for C₂₃H₂₇NO₃, 365.20).

6-bromohexyl methacrylate (iii)

6-Bromohexan-1-ol (10.05 g, 55.5 mmol) and triethylamine (17 mL, 122 mmol) were dissolved in dichloromethane under an argon atmosphere and cooled down to -20 °C whilst stirring. Methacryloyl chloride (5.69 mL, 58.28 mmol) was slowly added at this temperature. After stirring at -20 °C for 1 h, the mixture was slowly warmed up to room temperature. After 17 h, the mixture was concentrated and the white solid was filtered off. Column chromatography (10 vol% EtOAc in heptane) yielded 7.9 g (31.6 mmol, 57 %) of **iii** as a colorless oil (NMR experiments revealed that a small portion of the bromide had been substituted by chloride). In order to avoid premature polymerization of the compound, a small amount of tert-butyl hydroquinone (TBHQ) was added. ¹H NMR (400 MHz, CDCl₃): δ = 6.10 (s, 1H), 5.55 (s, 1H), 4.15 (t, J = 7 Hz, 2H), 3.41 (t, J = 7 Hz, 2H), 1.94 (s, 3H), 1.88 (p, J = 7 Hz, 2H), 1.70 (p, J = 7 Hz, 2H), 1.45 (m, 4H). ¹³C NMR (100 MHz, CDCl₃): δ = 167.47, 136.46, 125.24, 64.52, 33.68, 32.62, 28.46, 27.80, 25.23, 18.33. IR (ATR): max = 838, 937, 989, 1011, 1139, 1159, 1248, 1294, 1317, 1404, 1418, 1454, 1498, 1582, 1597, 1636, 1716, 2007, 2863, 2940.

4'-(6-methacyloxyhexyloxy-4-stilbazole) (6SzMA)

Under an inert argon atmosphere, 4.60 g (23.3 mmol) of compound **ii** was dissolved in 50 ml dry dimethylformamide (DMF) containing cesium carbonate (22.78 g, 69.9 mmol, 3 eq.) and powdered 4 Å mol. sieves. 6-bromohexyl methacrylate (**iii**, 6.39 g, 25.6 mmol, 1.1 eq.) was added dropwise at 0 °C and the mixture was stirred for 24h at room temperature. Subsequently, DMF was removed by use of rotary evaporation. The crude mixture purified by column chromatography using 20 vol% EtOAc in heptane to obtain 7.32 g (20.02 mmol) of an off-white solid. Yield: 86 %. ¹H-NMR (400 MHz, CDCl₃) δ: 1.50 (m, 4H), 1.72 (q, 2H, *J* = 14.0 Hz), 1.82 (q, 2H, *J* = 13.8 Hz), 1.95 (s, 3H), 3.99 (t, 2H, *J* = 6.5 Hz), 4.15 (t, 2H, *J* = 6.5 Hz), 5.55 (m, 1H), 6.10 (m, 1H), 6.87 (d, 1H, *J* = 15.4 Hz), 6.90 (d, 2H, *J* = 8.7 Hz), 7.25 (d, 1H, *J* = 16.3 Hz), 7.33 (d, 2H, *J* = 6.1 Hz), 7.47 (d, 2H, *J* = 8.7 Hz), 8.55 (d, 2H, *J* = 6.1 Hz). ¹³C-NMR (400 MHz, CDCl₃) δ: 167.6, 159.7, 150.3, 150.1, 145.0, 136.6, 132.9, 128.8, 128.5, 128.3, 125.4, 125.2, 120.8, 120.5, 114.9, 114.8, 67.9, 64.7, 29.2, 28.6, 25.9, 25.8, 18.4; MS *m/z*. 366.13 (M+H⁺) (calculated for C₂₃H₂₇NO₃, 365.20)

3.4.4 Methods

Preparation of LC Cells

30 × 30 mm glass slides were first wiped clean using ethanol, sonicated in ethanol for 20 minutes where after they were exposed 20 minutes to a UV-Ozone treatment. A thin layer of polyimide was applied to the glass slides by spincoating. The coated glass slides were precured at 90 °C for 10 minutes where after they were cured at 180 °C for half an hour. After curing, the glass plates were rubbed using a velvet cloth to induce a homogeneous alignment direction. Subsequently the glass slides were glued together using a photopolymerizable glue containing 20 μm beads to obtain a well-defined spacing between the glass plates. The glass plates were glued together with their rub-direction anti-parallel.

Preparation of LC Networks

A mixture containing **6SzMA•6OB** and **CL** (cross-linker) in an 1:1 weight ratio was used to prepare liquid crystalline networks. 1 wt% photo initiator (Irgacure 819) and 0,5 wt% inhibitor (BHT) were added to perform the photopolymerization. All compounds were dissolved in dichloromethane to obtain a homogeneous mixture. The dichloromethane was removed *in vacuo* after mixing. 20 μm thick films were prepared by

capillary suction of the LC-monomer mixture in the melt (125 °C) between two accurately spaced glass slides (LC cell). After filling of the cell, the mixture was cooled to 30 °C. Subsequently, the polymerization was performed by UV irradiation using a EXFO OmniCure® S2000 spot UV curing lamp for 600 seconds equipped with a 405 nm cut-off filter.

Removal of the **6OB** template

Small pieces of pristine **6SzMA•6OB** LCN were exposed to a 0.33 mM KOH solution in a 2:1 THF/water mixture overnight under continuous shaking. Subsequently, the films were placed in water to wash off the remaining KOH. The films were dried *in vacuo* prior further use.

Infiltration of H_3PO_4

Nanoporous polymer films (25 % CL, **6OB** removed) were exposed to a freshly made solution of 0.1 M H_3PO_4 (68 μ l in 10 ml solvent) and were shaken for 24 hours. Different H_3PO_4 occupations were obtained by using different solvents. Occupation of 1.06 eq. or 2.54 eq. H_3PO_4 were obtained by using THF/ H_2O (5 ml : 5 ml) or pure THF (10 ml) as solvent, respectively. H_3PO_4 infiltrated films were obtained and subsequently washed with ethanol. The films were vacuum dried before further characterization.

3.5 References

- [1] C. L. Gonzalez, C. W. M. Bastiaansen, J. Lub, J. Loos, K. Lu, H. J. Wondergem, D. J. Broer, *Adv. Mater.* **2008**, *20*, 1246–1252.
- [2] K. Kishikawa, A. Hirai, S. Kohmoto, *Chem. Mater.* **2008**, *20*, 1931–1935.
- [3] H. P. C. van Kuringen, G. M. Eikelboom, I. K. Shishmanova, D. J. Broer, A. P. H. J. Schenning, *Adv. Funct. Mater.* **2014**, *24*, 5045–5051.
- [4] L. Vilčiauskas, M. E. Tuckerman, G. Bester, S. J. Paddison, K.-D. Kreuer, *Nat. Chem.* **2012**, *4*, 461–466.
- [5] T. Kato, N. Mizoshita, K. Kishimoto, *Angew. Chem. Int. Ed.* **2006**, *45*, 38–68.
- [6] B. D. Shaw, E. A. Wagstaff, *J. Chem. Soc. Resumed* **1933**, 77.
- [7] M.-C. Chiang, W. H. Hartung, *J. Org. Chem.* **1945**, *10*, 21–25.
- [8] J. E. Stumpel, D. Liu, D. J. Broer, A. P. H. J. Schenning, *Chem. Eur. J.* **2013**, *19*, 10922–10927.
- [9] T. Kato, J. M. J. Fréchet, T. Uryu, F. Kaneuchi, C. Jin, *Liq. Cryst.* **2006**, *33*, 1429–1437.
- [10] S. Diele, *Berichte Bunsenges. Für Phys. Chem.* **1993**, *97*, 1326–1336.
- [11] N. Kapernaum, C. S. Hartley, J. C. Roberts, R. P. Lemieux, F. Giesselmann, *Beilstein J. Org. Chem.* **2009**, *5*, 65.

- [12] N. Kapernaum, F. Knecht, C. S. Hartley, J. C. Roberts, R. P. Lemieux, F. Giesselmann, *Beilstein J. Org. Chem.* **2012**, *8*, 1118–1125.
- [13] J. P. F. Lagerwall, F. Giesselmann, *ChemPhysChem* **2006**, *7*, 20–45.
- [14] E. Peeters, J. Lub, J. a. M. Steenbakkers, D. J. Broer, *Adv. Mater.* **2006**, *18*, 2412–2417.
- [15] P. Davidson, D. Petermann, A. M. Levelut, *J. Phys. II* **1995**, *5*, 113–131.
- [16] J. J. R. Arias, J. Carlos Dutra, A. d. S. Gomes, *J. Membr. Sci.* **2017**, *537*, 353–361.
- [17] Y. Yin, J. Wang, S. Jiang, X. Yang, X. Zhang, Y. Cao, L. Cao, H. Wu, *RSC Adv.* **2015**, *5*, 75434–75441.
- [18] K. Miyatake, T. Tombe, Y. Chikashige, H. Uchida, M. Watanabe, *Angew. Chem. Int. Ed.* **2007**, *46*, 6646–6649.
- [19] G. Favaro, U. Mazzucato, F. Masetti, *J. Phys. Chem.* **1973**, *77*, 601–604.
- [20] W.-J. Liang, S.-J. Hsieh, C.-Y. Hsu, W.-F. Chen, P.-L. Kuo, *J. Polym. Sci. Part B Polym. Phys.* **2006**, *44*, 2135–2144.

Chapter 4

The formation of gold nanoparticles inside 2D nanoporous materials

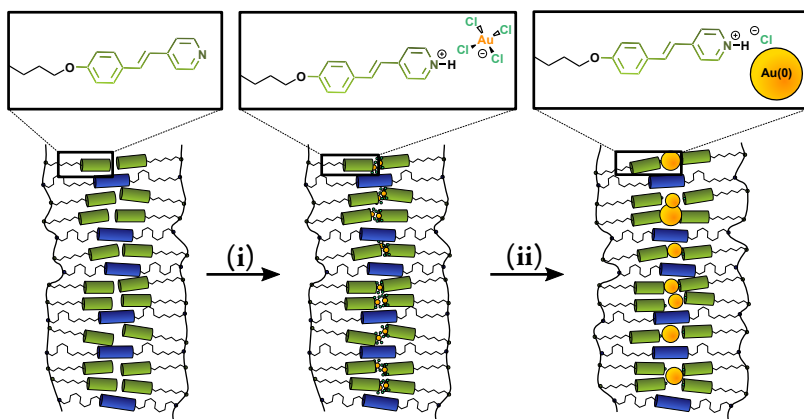
Abstract

Nanoporous hybrid polymers that contain nanoparticles inside their pores are of interest as, for example size selective heterogeneous catalysis. This chapter describes the synthesis and in-depth characterization of gold nanoparticles inside a liquid crystal network (LCN) containing 2D stilbazole nanochannels. A two-step procedure is followed where first the nanopores are infiltrated with a gold precursor, and subsequently the particles are synthesized by chemical reduction. The gold precursor was quantitatively bound to the stilbazole moieties in the 2D lamellae of the smectic LCN without disturbing the molecular organization. During exposure to aqueous NaBH_4 , gold nanoparticles are formed inside the polymer network. It was shown that diffusion of both the reductant and the gold precursor takes place during the reaction, causing the particles to only form in the first few microns of the polymer film. Furthermore, the diffusion and the soft nature of the polymer matrix causes the particles to grow larger than the confined space of the 2D channels.

4.1 Introduction

Hybrid inorganic/organic materials containing metallic nanoparticles are currently receiving a lot of attention due to their potential application in flexible electronics,[1] sensors,[2] photonics,[3] and catalysis.[4] There are several methods available today to fabricate hybrid materials with controlled nanoparticle (NP) dimensions. The production of materials containing nanoparticles smaller than two nanometers remains, however, a challenge. These extremely small sized particles possess unique catalytic properties and their inclusion inside nanoporous materials may find application in future heterogeneous catalysts.[5–7]

Nanoparticles of this size have been synthesized in zeolite-like structures[8] or inside metal organic frameworks.[5] Other studies have shown that by using smectic liquid crystalline polymer networks containing carboxylate functional 2D nanopores, small silver nanoparticles could be synthesized in a controlled fashion.[9, 10] The synthetic procedure involves the deprotonation of benzoic acid moieties, a subsequent ion exchange using AgNO_3 to obtain an Ag^+ -polymer hybrid. The ionic silver was subsequently reduced to metallic $\text{Ag}(0)$ using aqueous sodium borohydride (see Chapter 1).



Scheme 4.1: Approach of making Au NPs using a nanoporous smectic LCN containing basic pyridyl moieties. (i) Infiltration of the acidic gold(III) precursor (HAuCl_4). (ii) Synthesis of Au NPs by reduction using sodium borohydride (NaBH_4).

The smectic material developed in Chapter 3 contains well-defined 2D nanochannels with a basic pyridyl functionality. This basic interior can potentially be used to bind acidic metal precursors such as chloroauric acid (HAuCl_4) to produce gold nanoparti-

cles with the dimensions are controlled by the pore size. In this chapter, the infiltration of HAuCl_4 (step *i*) and the subsequent chemical reduction inside the polymeric matrix (step *ii*) are investigated (Scheme 4.1). The reduction process is studied in detail by various spectroscopy and microscopy techniques to unravel the mechanism of the nanoparticle formation.

4.2 Results and Discussion

4.2.1 Infiltration of the Au precursor

Liquid crystalline networks containing 2D nanopores exhibiting a pyridyl surface were fabricated according to the procedure described in Chapter 3. 20 μm thick planar aligned films were prepared using LC cells containing a polyimide alignment layer. To maintain the lamellar structure after photopolymerizing and the subsequent template removal, 50 wt% crosslinker was used. The obtained polymer films were exposed to a 50 mM chloroauric acid trihydrate ($\text{HAuCl}_4 \cdot 3 \text{H}_2\text{O}$) solution in the dark to incorporate the gold precursor. The exposure to light was avoided as much as possible to prevent any premature reduction of the precursor. Using THF as solvent, the pore interior was efficiently converted to the stilbazolium chloroaurate. Both the swelling of the network and low dissociation of the chloroauric acid in THF assisted in the formation of the complex. After 15 minutes shaking, a strong coloration of the film was observed from nearly transparent to yellow/orange. The solution was shaken for 16 hours before the film was removed, washed with water, and dried *in vacuo*.

FTIR spectroscopy confirmed the formation of the stilbazolium chloroaurate salt in interior, by the presence of $\text{N}^+ - \text{H}$ bands located at $3080 - 3240 \text{ cm}^{-1}$ (Figure 4.1a). The band at 3500 cm^{-1} indicates the presence of water pointing to the formation of a hydrated salt. A vibrational linear dichroism (VLD) measurement at 3288 cm^{-1} reveals an anisotropy of the $\text{N} - \text{H}$ bonds. Along the molecular director (90° and 270°) an absorbance parallel (A_{\parallel}) of 0.58 was obtained and perpendicular (0° and 180° , A_{\perp}) of 0.14 (Figure 4.1b). From the VLD measurements an orientational order parameter ($S = \frac{A_{\parallel} - A_{\perp}}{2A_{\perp} + A_{\parallel}}$) of 0.51 was obtained, indicating the preservation of the liquid crystalline organization after the precursor infiltration.

X-ray photoelectron spectroscopy (XPS) measurements revealed a $\text{Au}4f$ spin-orbit doublet appearing at 84.3 eV ($4f_{7/2}$) and 87.9 eV ($4f_{5/2}$), confirming that the polymer film

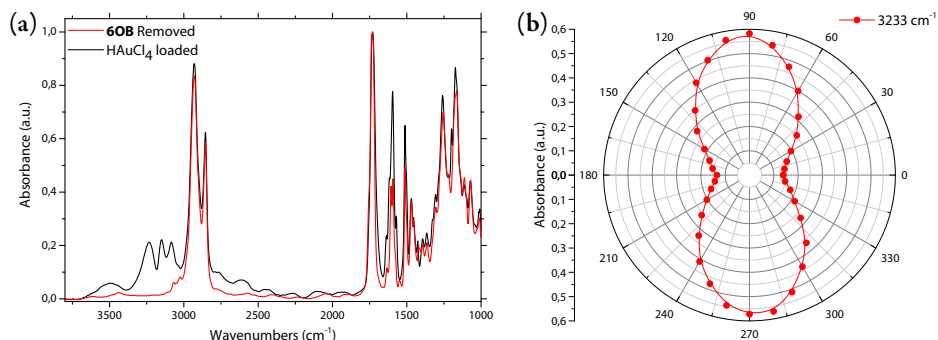


Figure 4.1: Infrared spectroscopy and vibrational linear dichroism of the HAuCl_4 infiltrated polymer film. (a) FTIR spectra of a pyridiyl functional nanoporous polymer (6OB removed, red curve) and the HAuCl_4 infiltrated polymer network (black curve). (b) Polar plot of the polarization scan at 3233 cm^{-1} (N–H band).

contains Au ions (Figure 4.2).[11] However, this value is lower than generally reported for Au(III) ions ($4f_{7/2} \approx 86\text{ eV}$). This could indicate that the precursor is partly reduced to Au(I) or Au(0). An XPS depth-scan was performed by subsequent sputter cycles confirming that the gold was present through the thickness of the polymer film. A slight increase of binding energy (0.2 eV) was observed from the surface to the bulk of the film. It is anticipated that this shift is caused by the change in chemical environment of the gold atoms from the surface to the bulk.

Looking at the atomic ratio $[\text{Au}]/[\text{Cl}]$ present in the film determined from the Au4f and the Cl2p signals, one would expect a 1:4 Au/Cl ratio (AuCl_4^-); however, a 1:1 ratio was found throughout the thickness of the film, confirming the formation of Au(I). It should be noted that cationic gold, and especially Au(III), is known to undergo photo-reduction, and could be reduced during XPS measurements (*vide infra*).[12]

Thermal gravimetric analysis in an air atmosphere was performed on freshly prepared HAuCl_4 loaded polymer films to quantify the amount of gold precursor infiltrated (Figure 4.2c). The degradation occurred in 3 distinct thermal events occurring at 230 °C, 360 °C, and 550 °C, leaving a residual weight percentage of 14.3 % metallic Au(0). After removal of the 6OB template, the polymer film contains approximately 1.05 mmol stilbazole moieties per gram (Chapter 3). Assuming stoichiometric binding of the chloroauric acid (HAuCl_4) to the stilbazole moieties, a residual weight percentage of 14.4–14.6 % is expected, depending on the hydrate content ($4\text{ H}_2\text{O}$ or $3\text{ H}_2\text{O}$, respectively) of the

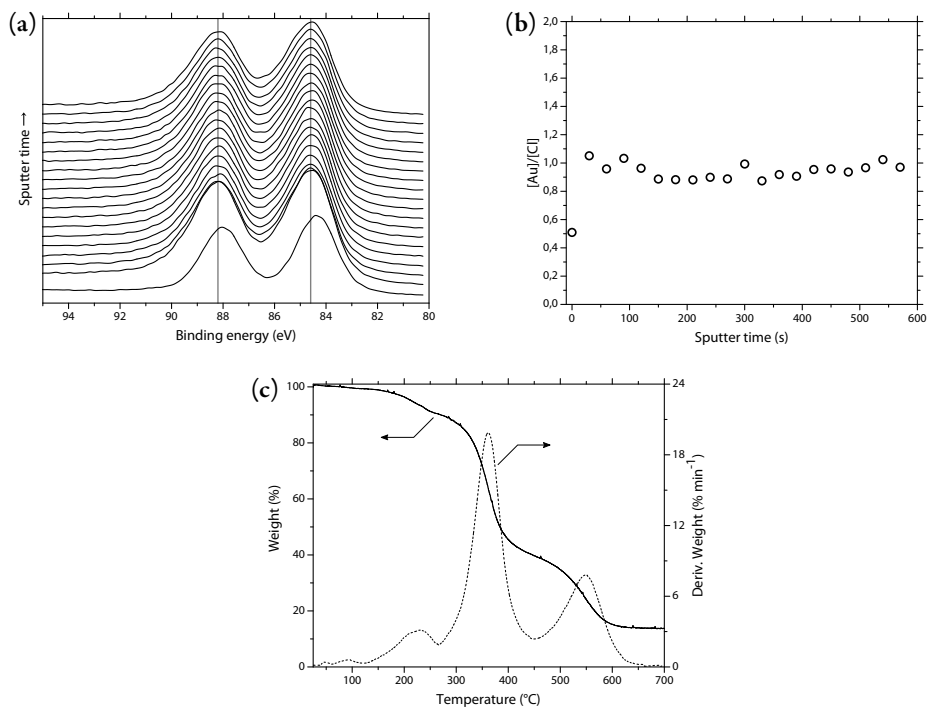


Figure 4.2: X-ray photoelectron spectroscopy and thermal gravimetric analysis of the HAuCl_4 infiltrated polymer film. (a) XPS depth scan at the $\text{Au}4f$ region. (b) Atomic concentration ratio of gold over chlorine ($[\text{Au}]/[\text{Cl}]$) as function of the sputter time. (c) Thermal gravimetric analysis of the HAuCl_4 infiltrated polymer film.

Au(III) salt. This latter measurement confirms that the gold precursor was successfully incorporated with an occupation level of 98–99 %, and indicates that, indeed, photo-reduction has occurred during XPS measurements.

Transmission X-ray diffraction measurements were performed to study the impact of the infiltration of HAuCl_4 on the molecular structure of the polymer network. From the 2D diffractogram of the HAuCl_4 infiltrated film (Figure 4.3c), one can notice a strong increase of scatter intensity from the lamellar spacing (small angle) compared with the pristine $\mathbf{6SzMA}\cdot\mathbf{6OB}$ or the nanoporous ($\mathbf{6OB}$ removed) films. Indeed, from the azimuthal integration, one can see that the intensity is approximately a 4-fold higher than the pristine $\mathbf{6SzMA}\cdot\mathbf{6OB}$ film, indicating that the AuCl_4^- ions are located inside the lamellae. Compared to the porous LCN film, the d-spacing of the gold precursor infiltrated film decreased from 4.47 nm to 4.23 nm. This decrease is expected to be caused by the

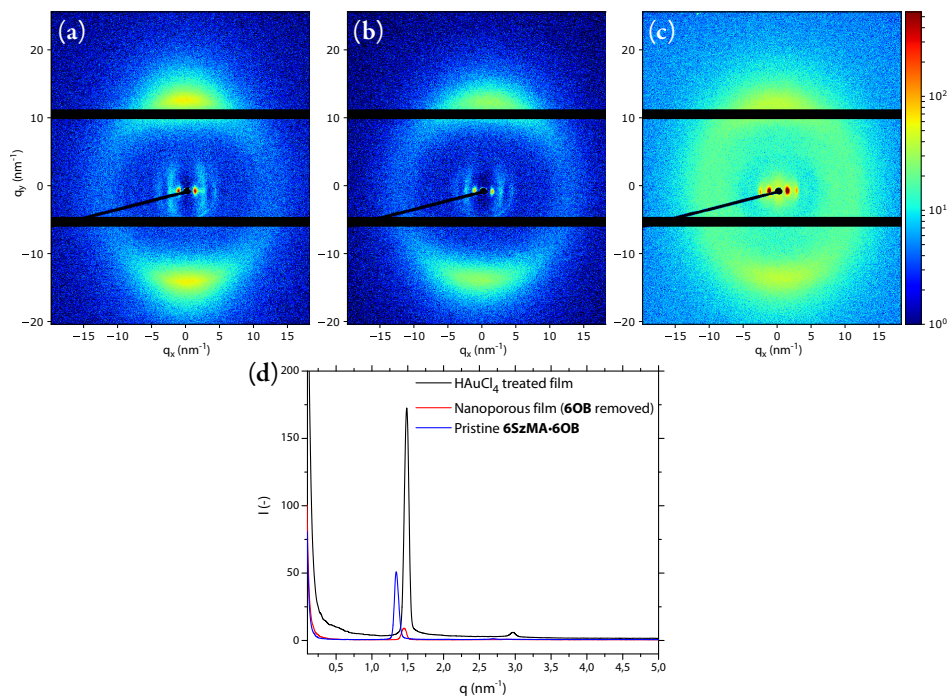


Figure 4.3: Structural characterization of the LCN films before and after HAuCl_4 treatment. (a-c) 2D x-ray diffractograms of the pristine 6SzMA-6OB film, pyridyl functional nanoporous film (6OB removed), and the HAuCl_4 infiltrated film. (d) Azimuthal integration of the small angle region of the x-ray diffractograms obtained from MAXS measurements.

strong electrostatic interactions between the cationic protonated stilbazolium moieties and AuCl_4^- anions. Furthermore, the wide angle signals originating from the intermolecular spacing are still highly anisotropic, agreeing with the VLD data obtained before (Figure 4.1b).

4.2.2 Synthesis of gold nanoparticles

In order to reduce the ionic gold to metallic gold ($\text{Au}(0)$), the polymer films were exposed to a 0.1 M sodium borohydride (NaBH_4) solution overnight. During the reaction the polymer film changed color from yellow/orange to black, suggesting the formation of gold nanoparticles, displaying surface plasmon resonance (Figure 4.4a). XPS measurements were performed on the hybrid Au-polymer films to confirm the reduction to $\text{Au}(0)$. After the sodium borohydride treatment, a chemical shift of approximately -1 eV to 83.1 eV of the binding energy was observed compared with the non-treated films. This negative chemical shift in binding energy is typically caused by a lower coulombic

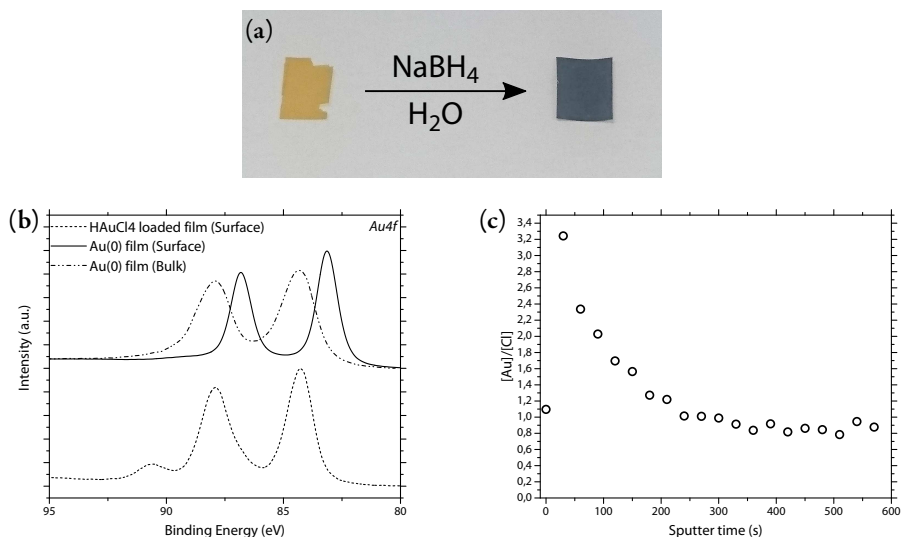


Figure 4.4: Chemical reduction of the Au salt by NaBH_4 treatment. (a) Photograph of a HAuCl_4 loaded (left) and a NaBH_4 treated (right) polymer film. (b) X-ray photoelectron spectroscopy scan at the Au4f region of the NaBH_4 treated film at the surface (solid line) and in the bulk (300s sputtering, dash-dot-dot line). A scan of the HAuCl_4 infiltrated film can be seen in the bottom (short-dash line). (c) Atomic concentration ratio of gold over chlorine ($[\text{Au}]/[\text{Cl}]$) as function of the sputter time.

interaction between the emitted electron and the atom core, due to a lower oxidation state of the atom. This shift agrees with reported values in the literature, and confirms the formation of Au(0).^[13] However, when the sample was remeasured after a 300s of sputtering (etching), it became obvious that ionic gold is still present in the bulk of the film (Figure 4.4b, dash-dot curve). The Au4f signals of the bulk overlap exactly with the measurement of the precursor loaded film (short-dash line). The reaction gradient becomes more clear in Figure 4.4c, where the atomic ratio $[\text{Au}]/[\text{Cl}]$ versus sputter time (depth) is presented. By the high $[\text{Au}]/[\text{Cl}]$, one can see that only under the surface of the film there is an accumulation of Au(0). It is expected that $[\text{Cl}]$ will never reach zero since HCl is produced during the reduction reaction and forms a stilbazolium chloride salt inside the lamellae. In the bulk $[\text{Au}]/[\text{Cl}]$ reaches 1 again as seen previously for the Au(III) loaded film, indicating that the reduction only occurred directly under the surface.

Transmission x-ray diffraction measurements were performed to evaluate the microstructure of the chemically reduced Au-polymer films. At $q = 26.7 \text{ nm}^{-1}$ a new scattering signal was observed originating from the (111) lattice plane of the gold, confirming the

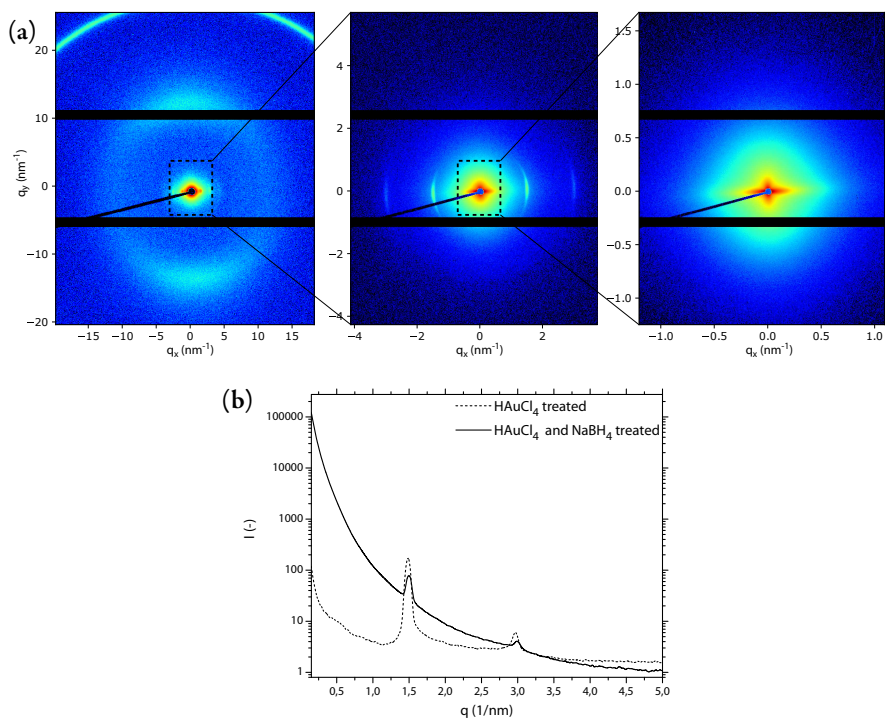


Figure 4.5: Structural characterization of the NaBH_4 treated film. (a) From left to right; wide, medium, and small angle 2D x-ray diffractograms of the NaBH_4 treated film. (d) Azimuthal integration of the small angle region of the x-ray diffractograms obtained from medium angle regions. Short-dash line represents the HAuCl_4 loaded film and the solid line the NaBH_4 treated film.

presence of metallic Au. The chemical reduction step did not disturb the orientational order, since the inter-molecular spacing ($q \approx 14 \text{ nm}^{-1}$) signals show anisotropy. Like the orientational order, the lamellar structure of the material is maintained after the chemical treatment (Figure 4.5a, middle panel). The azimuthal integration of the medium angle region can be found in Figure 4.5b. From this graph, one can see that the position of the signals originating from the lamellar spacing did not shift ($q = 1.50 \text{ nm}^{-1}$, $d = 4.2 \text{ nm}$). However, the background scattering in the small angle region (larger features) increased substantially. The 2D x-ray diffraction of the small angle region (Figure 4.5a, right panel) shows a strong anisotropic scattering, indicating the presence of larger particles or aggregates that are oriented mainly along the molecular director (*vide infra*).

To get a better understanding of the size, shape, and organization of the nanoparticles

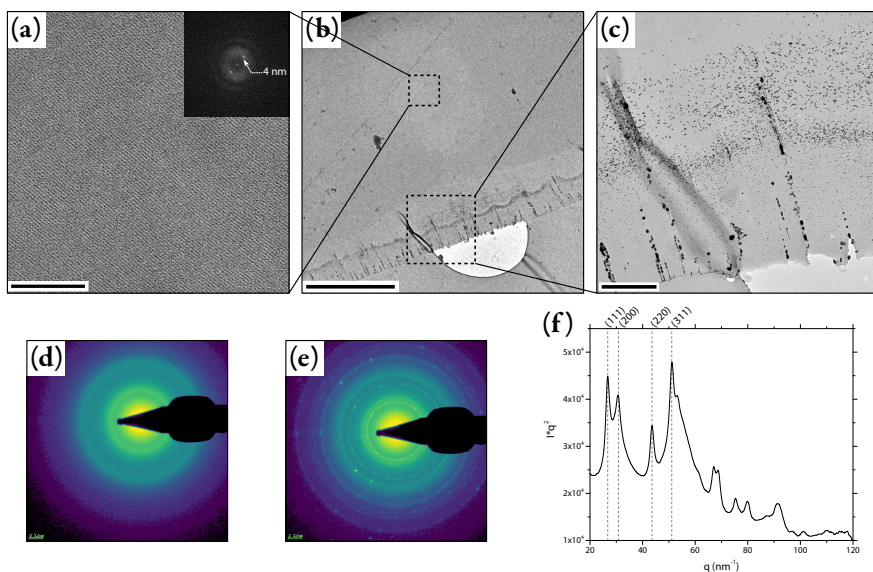


Figure 4.6: Transmission electron microscopy of a ultramicrotomed cross-section of the NaBH_4 treated film. (a) High magnification TEM micrograph of the central area of the film. Scale bar = 100 nm. Inset: FFT of the micrograph. (b) TEM micrograph of the cross-section of the film. Scale bar = 5 μm . (c) TEM micrograph showing the surface region of cross-section of the film. Scale bar = 500 nm. (d) SAED pattern of the central area of the film. (e) SAED pattern of the surface region of cross-section of the film. (f) Azimuthal integration of the electron diffraction pattern of the surface region of the film (panel (e)) confirming the presence of metallic gold.

throughout the thickness of the polymer film, the film was ultramicrotomed perpendicular to the molecular director and ~ 50 nm thick cross-sections were examined by transmission electron microscopy (TEM, Figure 4.6). Figure 4.6a and c are higher magnification micrographs of the bulk and near the surface of the polymer film, respectively. From the overview micrograph one can identify various regions and features. In Figure 4.6c, from the surface of the film toward the bulk, one can see in the first micrometer the formation of dispersed particles ($d < 10$ nm) and strings of larger particles ($d \sim 20$ nm). In the region around 2 μm deep, a high concentration of particles with a diameter of approximately 15 nm is observed. Selected area electron diffraction (SAED) confirmed the presence of metallic gold (Figure 4.6e & f). Various crystal planes could be identified as shown on top of Figure 4.6f. Deeper, no particles were observed, plus the film appears to be lighter gray, indicating the diffusion of gold ions to the reaction site. Looking deeper into the bulk of the film (Figure 4.6a), a very regular structure is observed from the gold ions that are arranged in a lamellar organization. From the FFT-

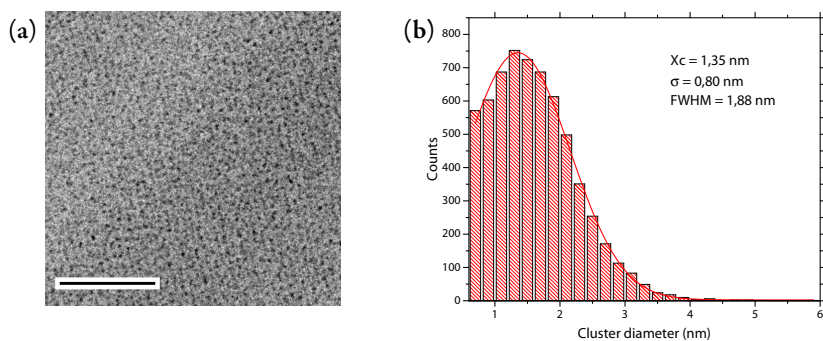
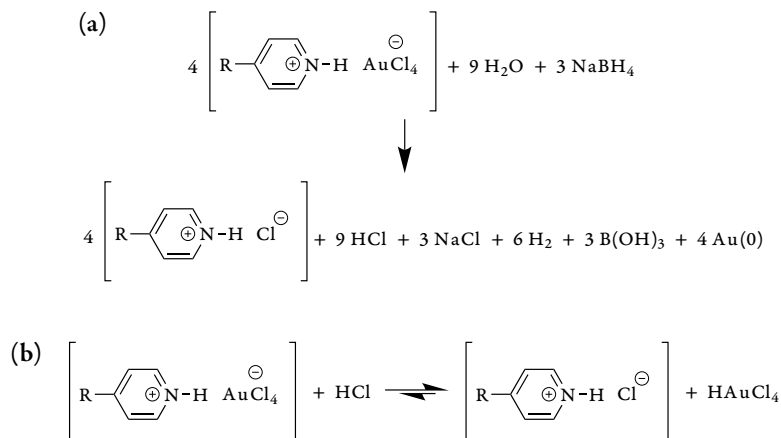


Figure 4.7: Estimation of the ionic gold cluster size. (a) Close-to-focus transmission electron micrograph (500 nm defocus). Scale = 50 nm. (b) Size estimation of the cluster size in a 300×300 nm area.

transformed micrograph (inset) a well-defined spacing of 4 nm was found, which is in agreement with the distance found earlier by x-ray diffraction. SAED was performed on this area to confirm that the lamellae only contain (amorphous) ionic gold species. Figure 4.6d indeed shows an amorphous scattering, confirming the absence of crystalline material. The size of the ionic cluster was determined using TEM (Figure 4.7), and using image analysis, an average cluster diameter of $1.4 \pm 0,80$ nm was estimated.

XPS, XRD, and TEM studies confirmed the formation of gold nanoparticles. However, TEM showed that the particles are not arranged inside the smectic lamellae but rather form a $1 \mu\text{m}$ -wide band beneath film surface. The reductant (NaBH_4) diffuses from the surface into the film, while the infiltrated AuCl_4^- ions diffuse from the bulk to the area where the reduction takes place. It is anticipated that HCl, released by the reduction reaction (Scheme 4.2a), enhances this counter diffusion of AuCl_4^- ions (Scheme 4.2b).

Scanning electron microscopy (SEM) was performed to image the surface of a nanoporous polymer film (6OB removed, Figure 4.8). On the surface of the film macroscopic pores are visible. The shape of pores was anisotropic with the long axis along the molecular director. The pores are formed during the post-synthetic modification steps of the LCN films. The oriented cross-links of the network prohibit the material of expanding along the molecular director, however, perpendicular it is still allowed. Furthermore, this directionality results in a practically non existing cross-link density in the lateral direction, causing macroscopic pores to be formed when strained or swelled. It is anticipated that in these pores, chain-like structures particles can be formed, and the elon-



Scheme 4.2: The reduction of HAuCl_4 by NaBH_3 inside the polymer film. (a) The balanced reaction scheme of the reduction. (b) Ion exchange caused by the excess of HCl released by the reduction reaction.

gated shape of the pores can contribute to the formation of anisotropic aggregates of the gold nanoparticles. This latter would explain the anisotropic x-ray scattering seen in Figure 4.5a.

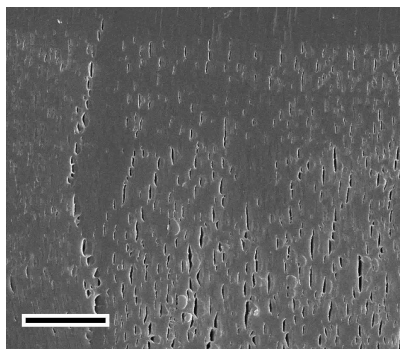
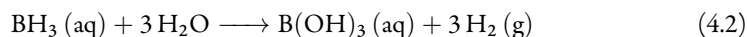
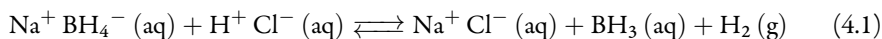


Figure 4.8: Scanning electron microscopy image of the surface of the nanoporous polymer network (6OB removed) before Au precursor infiltration. Macroscopic pores are visible at the film surface. Scale bar = 5 μm .

From the results obtained, a mechanism for the nanoparticle growth can be postulated, as depicted in Figure 4.9. In the first stage of the reduction, the HAuCl_4 loaded film is exposed to an aqueous NaBH_4 solution, the reductant enters the film through the surface and the macroscopic pores (Figure 4.9a, blue arrows). Once the gold at the surface starts to reduce, HCl is formed. Consequently, ion exchange with the AuCl_4^- occurs, resulting in the migration of the ionic gold species from the bulk as indicated by the red

arrows in Figure 4.9a. Furthermore, as shown by the red arrows in Figure 4.9a, more gold ions can reach the surface of the macroscopic pores as compared to the surface of the film. This results in the growth of larger particles inside those pores (Figure 4.9b). Once all gold(III) in the first micron is consumed (faint green color in Figure 4.9b) the reduction continues in a reaction-diffusion fashion towards the bulk. The reductant continues to diffuse towards to bulk, where, due to depletion and exchange with Cl^- , the AuCl_4^- ions diffuse towards the reaction front. This causes the formation of a highly concentrated region of nanoparticles just below the macroscopic pores ($\sim 2 \mu\text{m}$ deep, Figure 4.9c). This results in a AuCl_4^- depleted region (faint green) between the bulk and the nanoparticle rich area. Finally, because of the release of HCl during the reduction of the HAuCl_4 , the borohydride can undergo self-hydrolysis[14];



This self-hydrolysis reduces the effectiveness of the reductant, leading to an incomplete reduction reaction throughout the thickness of the film, as represented by the dark green area in the bottom of Figure 4.9c.

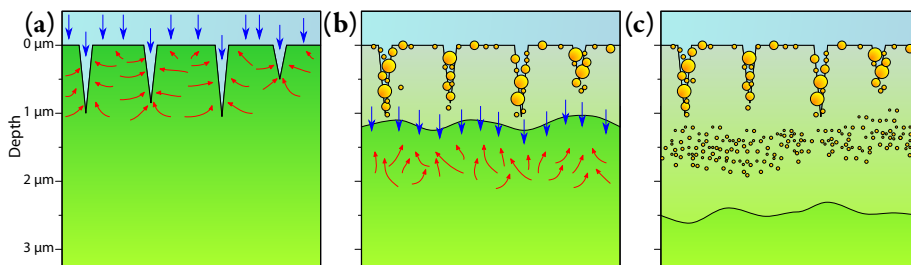


Figure 4.9: Postulated mechanism of the formation of Au NPs inside a nanoporous film by chemical reduction. (a) Begin of the reduction reaction. Reductant (NaBH_4) enters through the surface of the film. Induced by the formation of HCl by reaction, the precursor salts (AuCl_4^-) counter-diffuse towards the surface. (b) Due to the diffusion process, many particles are formed at the interface of the film. (c) After depleting the first micron of the film, the diffusion of the both the reductant and the gold precursor carry on, forming a band of particles.

4.3 Conclusion

This chapter describes the synthesis and in-depth characterization of the formation of gold nanoparticles inside a polymer matrix containing 2D nanochannels by chemical reduction. This reduction mechanism was studied in detail. The acidic HAuCl_4 precur-

sor was quantitatively bound to the stilbazole moieties in the 2D lamellae of the smectic LCN without disturbing the molecular organization. Using aqueous NaBH_4 , gold nanoparticles are formed inside the polymer network near the surface. It has been shown that diffusion of both the reductant and the gold precursor takes place during the reaction. The diffusion and the soft nature of the polymer matrix causes the particles to grow larger than the confined space of the 2D channel, showing that it is very challenging to prepare well-defined hybrid materials via this approach. Nonetheless, the localization of nanoparticles below the surface of a nanoporous polymer material can be of interest for catalytic active membranes, *e.g.* the inclusion of catalytic active platinum nanoparticles at the surface of proton conduction membranes for fuel cells.

4.4 Experimental section

4.4.1 Materials

Sodium borohydride (>96 %) and Gold (III) chloride trihydrate ($\text{HAuCl}_4 \cdot 3 \text{H}_2\text{O}$, ≥ 49.0 % Au basis) were obtained from Sigma Aldrich. All Solvents used were analytical grade and obtained from Biosolve. All reagents were used as received, without further purification.

4.4.2 Characterization

Infrared spectroscopy was performed on a Varian 670 IR spectrometer equipped with a microscopy setup over a range of $4000\text{-}650 \text{ cm}^{-1}$ with a spectral resolution of 4 cm^{-1} and 100 scans per spectrum. X-ray diffraction experiments were performed on a SAXS-LAB GANESHA 300 XL system. UV-Vis spectroscopy experiments were done using a Shimadzu UV-3102 spectrophotometer. Transmission electron microscopy imaging was performed under $2.5 \mu\text{m}$ or 500 nm (close-to-focus image) defocus on a FEI-Titan TEM equipped with a field emission gun (FEG) and operating at 300 kV . Images were recorded using a $2\text{k} \times 2\text{k}$ Gatan CCD camera equipped with a post column Gatan Energy Filter (GIF), with an electron dose of $15.8 \text{ e} \text{ \AA}^{-2}$ per image. The XPS measurements are carried out with a Thermo Scientific K-Alpha, equipped with a monochromatic small-spot X-ray source and a 180° double focusing hemispherical analyzer with a 128-channel detector. Spectra were obtained using an aluminium anode ($\text{Al K}_\alpha = 1486.6 \text{ eV}$) operating at 72 W and a spot size of $400 \mu\text{m}$. Survey scans were measured at a constant pass energy of 200 eV and region scans at 50 eV . The background pressure was 2×10^{-9}

mbar and during measurement 4×10^{-7} mbar argon because of the charge compensation dual beam source. Spectra are referenced to the C1s peak at 284.5eV of the carbon tape. Scanning electron microscope (SEM) studies were performed using a FEI Quanta 3D field emission SEM. The samples were sputter coated with 7 nm thick gold layer before visualization to increase the conductivity.

4.4.3 Methods

Preparation of LC Networks

A mixture containing **6SzMA•6OB** and **CL** (cross-linker) in an 1:1 weight ratio was used to prepare liquid crystalline networks. 1 wt% photo initiator (Irgacure 819) and 0,5 wt% inhibitor (BHT) was added to perform the photopolymerization (Chapter 3). All compounds were dissolved in dichloromethane to obtain a homogeneous mixture. The dichloromethane was removed *in vacuo* after mixing. 20 μm thick films were prepared by capillary suction of LC-monomer mixture in the melt (125 °C) between two accurately spaced glass slides (LC cell). After filling of the cell, the mixture was cooled to 30 °C. Subsequently, the polymerization was performed by UV irradiation using a EXFO OmniCure® S2000 spot UV curing lamp for 600 seconds equipped with a 405 nm cut-off filter.

Removal of the 6OB template

Small pieces of pristine **6SzMA•6OB** LCN were exposed to a 0.33 mM KOH solution in a 2:1 THF/water mixture overnight under continuous shaking. Subsequently, the films were placed in water to wash off the remaining KOH. The films were dried *in vacuo*.

Infiltration of the Au precursor

Small pieces of the nanoporous LCN (**6OB** removed) were exposed to a 50 mM H₂AuCl₄ solution in THF overnight under continuous shaking. Subsequently, the films were placed in water to wash off the excess H₂AuCl₄. The films were dried *in vacuo*.

Synthesis of Au NPs

The precursor infiltrated films were exposed to an aqueous 100 mM NaBH₄ solution overnight under continuous shaking. Subsequently, the films were placed in water to wash off the excess NaBH₄. The films were dried *in vacuo* prior to characterization.

4.5 References

- [1] A. C. Balazs, T. Emrick, T. P. Russell, *Science* **2006**, *314*, 1107–1110.

- [2] F. P. Zamborini, M. C. Leopold, J. F. Hicks, P. J. Kulesza, M. A. Malik, R. W. Murray, *J. Am. Chem. Soc.* **2002**, *124*, 8958–8964.
- [3] J. H. Park, Y. T. Lim, O. O. Park, J. K. Kim, J.-W. Yu, Y. C. Kim, *Chem. Mater.* **2004**, *16*, 688–692.
- [4] A. Corma, H. Garcia, *Chem. Soc. Rev.* **2008**, *37*, 2096–2126.
- [5] A. Corma, H. García, F. X. Llabrés i Xamena, *Chem. Rev.* **2010**, *110*, 4606–4655.
- [6] E. C. Tyo, S. Vajda, *Nat. Nano.* **2015**, *10*, 577–588.
- [7] J. Oliver-Meseguer, J. R. Cabrero-Antonino, I. Domínguez, A. Leyva-Pérez, A. Corma, *Science* **2012**, *338*, 1452–1455.
- [8] D. Esken, S. Turner, O. I. Lebedev, G. van Tendeloo, R. A. Fischer, *Chem. Mater.* **2010**, *22*, 6393–6401.
- [9] D. Dasgupta, I. K. Shishmanova, A. Ruiz-Carretero, K. Lu, M. Verhoeven, H. P. C. van Kuringen, G. Portale, P. Leclère, C. W. M. Bastiaansen, D. J. Broer, A. P. H. J. Schenning, *J. Am. Chem. Soc.* **2013**, *135*, 10922–10925.
- [10] A. Longo, D.-J. Mulder, H. P. C. van Kuringen, D. Hermida-Merino, D. Banerjee, D. Dasgupta, I. K. Shishmanova, A. B. Spoelstra, D. J. Broer, A. P. H. J. Schenning, G. Portale, *Chem. Eur. J.* **2017**, 10.1002/chem.201701493.
- [11] B. V. Crist, *Handbook of Monochromatic XPS Spectra*, Wiley, Chichester, **2000**.
- [12] E. Ozkaraoglu, I. Tunc, S. Suzer, *Surface and Coatings Technology*, SMMIB 2005 **2007**, *201*, 8202–8204.
- [13] L. Wang, Y. Zhu, J.-Q. Wang, F. Liu, J. Huang, X. Meng, J.-M. Basset, Y. Han, F.-S. Xiao, *Nat. Commun.* **2015**, *6*, 6957.
- [14] P. Brack, S. E. Dann, K. G. U. Wijayantha, *Energy Sci Eng* **2015**, *3*, 174–188.

Chapter 5

Semipermeable thermal responsive liquid crystalline elastomer shells

Abstract

The fabrication of semipermeable thermal responsive LCE shell actuators from oligomeric liquid crystalline diacrylates by glass capillary microfluidics is presented. After solvent extraction, osmosis, alignment, and photo-crosslinking homeotropic aligned LCE shells were obtained. The LCE shells show a typical anisotropic expansion when heated, resulting in an increase of the shell surface area. Since the fluid inside the shell expanded significantly less than the shell itself, a dimple is formed to accommodate the excess surface area.

5.1 Introduction

Compartmentalization is one of Nature's cornerstones of existing life. From a living life-form to the organelles inside its cells, it forms physical barriers ensuring biochemical processes can perform efficiently without interference. Scientists have taken this concept to the synthetic level to develop semipermeable vesicles that can display selective transport, enabling the release material on demand or performs selective catalytic reactions inside. In the field of polymer chemistry, some strategies to compartmentalize are well known, such as micellar vesicles and polymersomes from self-assembled block copolymers.[1, 2]

Liquid crystal shells have been a topic of growing interest in the past years, and constitute a stimulating tool for fundamental research in spontaneous ordering of soft matter. Some application opportunities have been proposed, as photonic elements,[3] for generating unclonable security patterns,[4] in sensing[5] and—in case of LCN shells—as soft actuators.[6]

By using a microfluidic set-up to fabricate the shells, their dimensions can be controlled in a very precise way[7].The production method allows for the choice of different inner and outer fluids, which subsequently will determine the director alignment in the shell. Yet, the delicate nature of the fluid-fluid interfaces bounding regular LC shells represents a drawback, limiting their lifetime and preventing their removal from the liquid continuous phase. To circumvent this limitation, some reports have included mesogens with polymerizable end groups, either for polymer stabilization of a shell that remains largely fluid[8] or for turning the shell into a polymeric solid or rubber.[9, 10] So far, only one study was presented with LCN shell actuator.[6] While this provided a proof of concept, the shells were relatively large and thick and the control of alignment was modest, largely because the production procedure locked in the flow-induced alignment during microfluidic production rather than giving the time for the liquid crystalline self-assembly to rearrange into its free-energy-minimizing configuration in the shell.

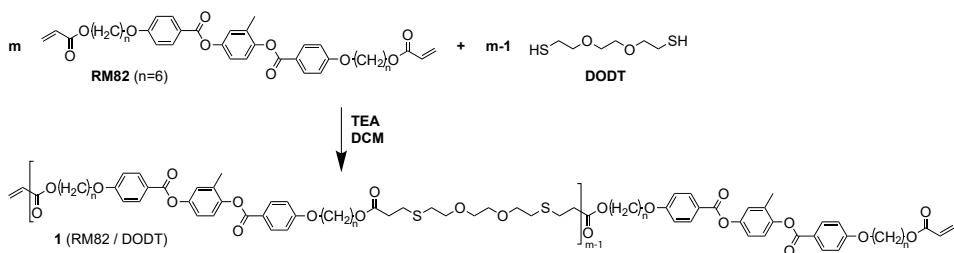
In this chapter, a novel approach to fabricate responsive semipermeable LCE shell is presented. The method involves the cross-linking of oligomeric reactive liquid crystals after the microfluidic shell production. In the microfluidic setup, the aqueous inner and outer fluids that will determine the preferential alignment of the LC are used.

Because of the well-controlled alignment of the mesogenic oligomers in 3D, the contraction and expansion of the shell can be anticipated and large. Main-chain LC oligomers were dissolved in an isotropic solvent for production. The cross-linking takes place after shell formation and solvent extraction, locking the self-assembled order of the oligomers developed in response to the surrounding aqueous fluids. The synthesis of the LC oligomer and their advantages over many conventional reactive mesogens for the formation of the LC shells, such as shifting the processing window of the shell to or close to room temperature are discussed. The (semi)permeability of the LCE shells was tested by an osmosis experiment. The shells obtained using a microfluidic device were thermally actuated, showing reversible buckling upon heating. The actuation is explained by the combination of the incompressible inner volume, the thermal expansion shell surface area due to the homeotropic aligned LCN, and the permeability of the shell.

5.2 Results and Discussion

5.2.1 Synthesis and characterization of the reactive mesogenic oligomer

In order to obtain a viscoelastic nematic reactive mesogen which can be used for the fabrication of shells from solution, a relatively short acrylate main-chain oligomer (< 10 repeating units) was prepared. The main-chain LC oligomer was synthesized by thiol-acrylate addition of the mesogenic diacrylate RM82 and 3,6-dioxa-1,8-octanedithiol (DODT) (Scheme 5.1).[11, 12] RM82 was present in a slight excess (1.1 eq) to obtain an oligomer with acrylate end groups, ensuring crosslinking of the LCE at a later stage. The reaction was performed by an overnight reaction at 35 °C where the diacrylate and dithiol compounds were dissolved in dichloromethane (DCM) in the presence of an amine catalyst. The subsequent extraction against HCl, and evaporation of DCM yielded the diacrylic LC oligomer (yield: ~95 %). The number average molecular weight (M_n) of the resulting oligomer was determined by GPC and found to be approximately 5800 g mol⁻¹ with a polydispersity index (M_w/M_n) of 2.5. It is anticipated that a relatively low molecular weight nematic LC oligomer will have sufficient mobility to allow spontaneous surface alignment and suppress crystallization after shell preparation and solvent extraction. After alignment of the oligomeric mesogens in the shell, the acrylic end-groups can be utilized to obtain LCE shells by photo-crosslinking. The presence of acrylate end-groups was confirmed by ¹H-NMR and FTIR measurements. Based on



the end groups, from $^1\text{H-NMR}$ an M_n of 7400 g mol^{-1} was calculated.

The phase behavior of the obtained oligomer was studied by differential scanning calorimetry (DSC). Oligomer **1** has a clearing point at $87 \text{ }^\circ\text{C}$ and a T_g at $-21 \text{ }^\circ\text{C}$ (Figure 5.1a). Furthermore, one inter-mesophase transition was observed at $49 \text{ }^\circ\text{C}$. Since the spacer length between the mesogenic units in the oligomer is regular, a smectic or semi-crystalline is expected to be formed, the oligomer solidifies to a wax-like form. In order to establish the nature of the mesophases the textures of each phase was studied with polarizing optical microscopy (POM). To this end, the oligomer was spin coated from 25 wt% CHCl_3 solution on polyimide-coated glass substrates and annealed overnight at $75 \text{ }^\circ\text{C}$. At this temperature, and after complete evaporation of the solvent, **1** shows a typical schlieren texture indicating a nematic phase (Figure 5.1d). Interestingly, disclinations of strength ± 1 are found exclusively. Most likely, they are caused by a hybrid alignment as result of the asymmetric boundary conditions; polyimide promoting planar alignment and air promoting homeotropic alignment. The resulting bend within the liquid crystal breaks the sign invariance of the $\mathbf{n}(\mathbf{r})$ projection in the sample plane, thereby prohibiting half-integer defect lines.[13] Upon cooling towards the next mesophase transition temperature, thin lines appear along the molecular director (Figure 5.1c). Once below the phase transition temperature, new lines appear perpendicular to the ones observed before (Figure 5.1b), suggesting a nematic to smectic phase transition. Indeed, the texture sequence resembles that observed for low molar mass liquid crystals in hybrid alignment at a nematic–smectic-A transition[14], the difference in the final state probably being related to the higher viscosity of the oligomer. In fact, the oligomer solidifies below the transition at $49 \text{ }^\circ\text{C}$ in time. It is anticipated that this solidification is caused by crystallization.[15]

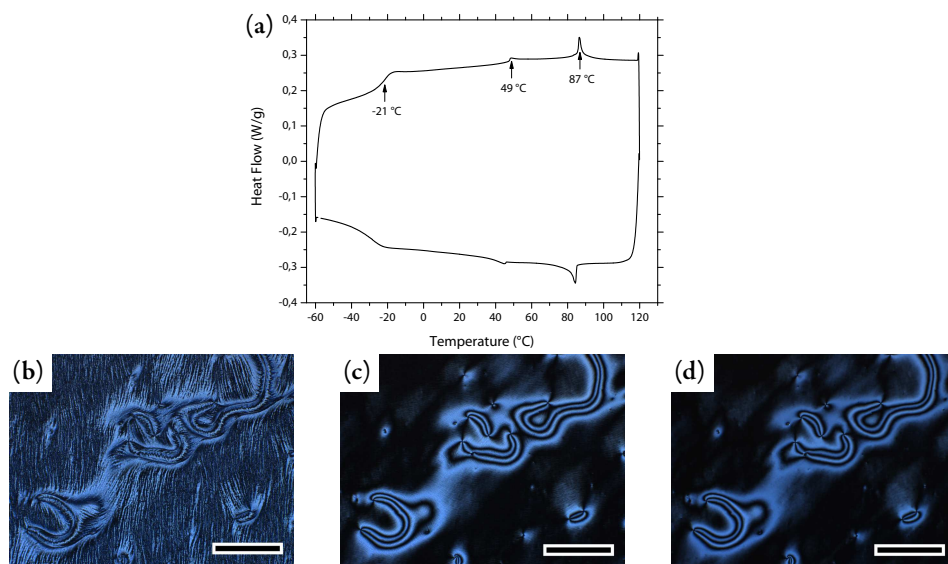


Figure 5.1: Phase behavior of oligomer 1. (a) DSC trace of the oligomer. (b-d) Polarized light micrographs of the oligomer under asymmetric boundary conditions (coating on polyimide substrate) at 25 °C, 55 °C, and 75 °C. Scale bar = 250 μm.

5.2.2 Thermo-responsive properties of free standing LCE films

First, free standing flat polymer films were prepared to study the thermoresponsive properties. Planar aligned LCE films of 50 μm thickness were prepared in LC cells coated with polyimide alignment layers. A small amount of photoinitiator (0,5 wt% Irgacure 819) was added to oligomer 1 for photo-crosslinking. After the photopolymerization, the cell was opened and the nematic LCE film was peeled-off. The thermal behavior of the elastomeric film was studied by DSC. The glass transition temperature was increased to -12 °C after photo-crosslinking compared to the pristine oligomer (Figure 5.2a). In the first heating curve of the elastomer, a very broad peak was observed centered at 68 °C. This might indicate that after crosslinking the polymer slowly crystallizes at room temperature. No other phase transitions were observed indicating that the LC phase was locked in the LCE.

The thermo-mechanical properties were studied by dynamic mechanical thermal analysis (DMTA). A storage modulus (E') plateau at about 2 GPa was found in the glassy state (Figure 5.2c). Heating from the glassy state, a steep drop in E' was observed at the

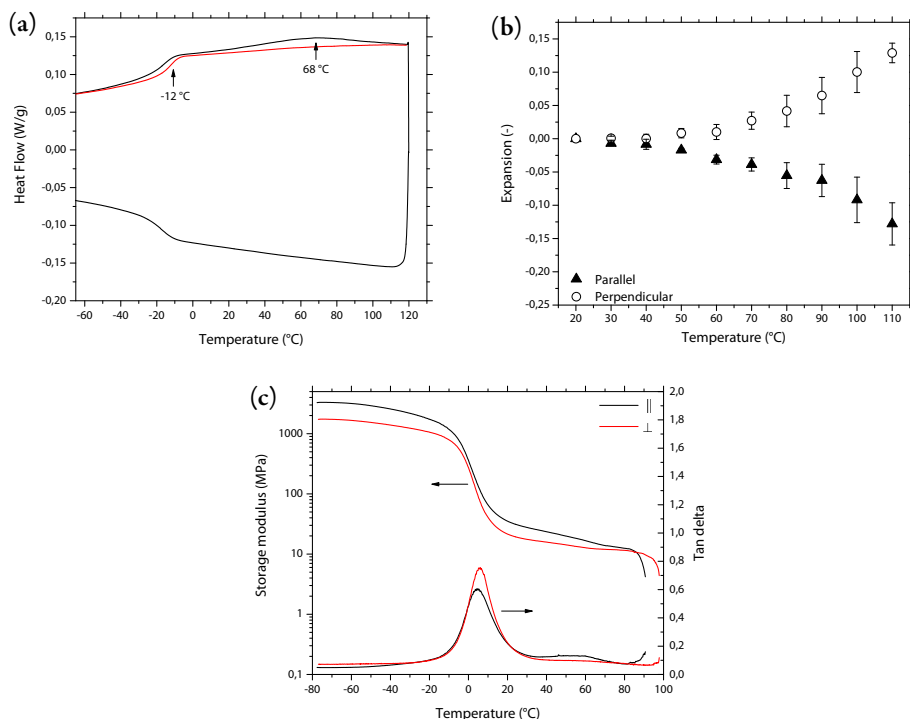


Figure 5.2: Thermal and mechanical properties of surface aligned free standing LCE films. (a) DSC thermogram. The black curve represents the first heating and cooling cycle. The red curve represents the second heating cycle. (b) Anisotropic thermal expansion. Circles: strain perpendicular to \mathbf{n} , triangles: strain parallel to \mathbf{n} . Error bar = Standard deviation over 4 measurements. (c) DMTA thermogram of the LCE. The black and red curves represent the storage modulus and $\tan\delta$ parallel and perpendicular to the director, respectively.

glass transition temperature. Above T_g (from 20 to 90 °C), E' reaches a rubbery plateau at about 10 MPa. The $\tan\delta$ curve suggests another transition at 60°C which might be attributed to the melting of the crystalline parts in the sample. Interestingly, the ratio between storage modulus parallel to \mathbf{n} (E'_{\parallel}) and perpendicular (E'_{\perp}) was found to be 1,9 in the glassy state, and 1,3 in the rubber state (>30 °C). Compared to the anisotropic mechanical properties of strain-aligned LCEs, the ratio $E'_{\parallel}/E'_{\perp}$ obtained is much smaller and is rather comparable to liquid crystalline networks.[16] This can be explained by the fact that the polymer chains themselves are not aligned in the material, merely the mesogen cores within the polymer chain are. Indeed the flexible spacer allows polymer chains to have hairpin-like conformation albeit forming an aligned monodomain film.

The anisotropic thermal expansion of the LCE film was determined using optical microscopy and shows a typical anisotropic strain when heated (Figure 5.2b). Upon heating to 110 °C, a positive expansion of 13 % was observed perpendicular to the molecular director while a contraction of the same magnitude was observed along the director. These large strains show promise to obtain large actuation of shells based on this material when heated (*vide infra*). All things considered, the mechanical characterization revealed that the elastomer shows rubber-like properties and anisotropic thermal expansion that facilitates the thermal actuation of the shell.

5.2.3 Preparation of LCE shells by glass capillary microfluidics

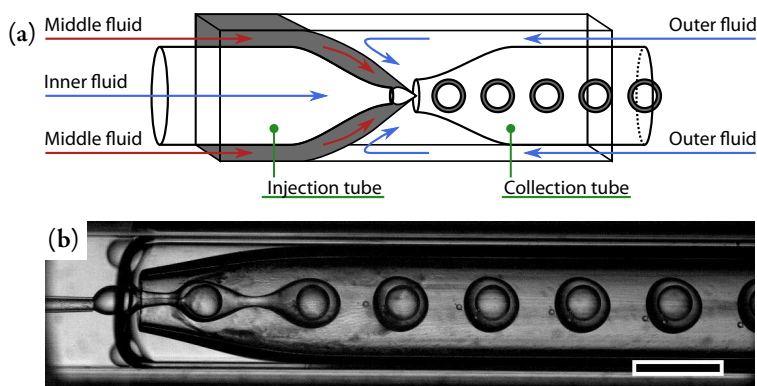


Figure 5.3: Coaxial glass capillary microfluidic device. (a) Schematic representation of the glass capillary microfluidic device. (b) A snapshot of the during microfluidic shell production. Scale bar = 500 μm .

Shells are produced using a coaxial glass capillary microfluidic device, following the basic design principle of Utada *et al.* (Figure 5.3a).[17] Typically, such a device exist of a square outer capillary with two nested round capillaries for injection of the inner fluid and collection of the shells, respectively. The middle fluid (oligomer solution) is pumped through the outer capillary from the left side of Figure 5.3a (red arrows). The inner fluid is pumped through the injection capillary (blue arrow). The outer fluid is, like the middle fluid, pumped through the outer capillary, but from the opposite side (blue arrows on the right side). The flow rates of all three fluids were adjusted such, that the co-flowing oligomer solution and inner fluid are flow-focused by the counter-flowing outer fluid, such that an double emulsion of the desired shells is collected in the second tapered cylindrical collection capillary, extending to the right in Figure 5.3a.

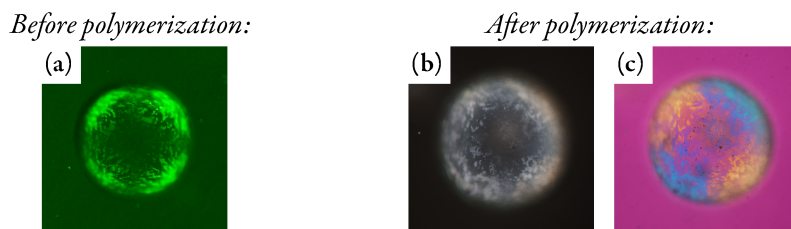


Figure 5.4: Polarized light micrograph of the aligned oligomer shell. (a) Before photo-crosslinking. Green light was used to circumvent the initiation of the polymerization. (b-c) After photo-crosslinking, without and with first order lambda plate, respectively.

A solution containing 20 wt% oligomer and 0,1 wt% photoinitiator (Irgacure 819) in dichloromethane (DCM) was used for the middle fluid. In order to produce shells, the outer and inner fluids should be immiscible with the middle fluid. Therefore, as inner and outer fluid, 5 wt% solutions of polyvinylalcohol (PVA, 13 000–18 000 g mol⁻¹, 87 % hydrolyzed) in 1:1 (v/v) water-glycerol mixture were used.

The produced shells are collected in a volume of 2 mL of demineralized water after production to dilute the double emulsion circumventing aggregation. The solution was refreshed 3 times to ensure complete extraction of the DCM. By heating the shells to the nematic phase (55 °C) and annealing overnight, alignment was obtained, see Figure 5.4a. Surprisingly, POM micrographs (using green light illumination to avoid premature photopolymerization) revealed an radial (homeotropic) organization of the mesogens. Generally, liquid crystals prefer a planar anchoring at the water interface. To date, using the same conditions, no case of homeotropic alignment has been reported. It is anticipated that the oligomer can take a hairpin-like conformation, exposing the more hydrophilic ethylene glycol spacer center to the water interface. This latter is expected to prefer homeotropic anchoring over planar. The annealed shells were cross-linked by UV irradiation ($\lambda = 365$ nm) at 55 °C (Figure 5.4b & 5.4c). When comparing the shells after microfluidic production and polymerization, a large size increase was noticed. This increase indicates that osmosis occurs during the solvent exchange and alignment steps.

5.2.4 Thermal actuation by the LCE Shells

After photo-crosslinking of the oligomers in the homeotropic aligned shells, a reversible thermal actuation was achieved by heating-cooling cycles. To do so, a glass capillary was filled with a PVA-glycerol-water solution in which an LCE shell was suspended, having

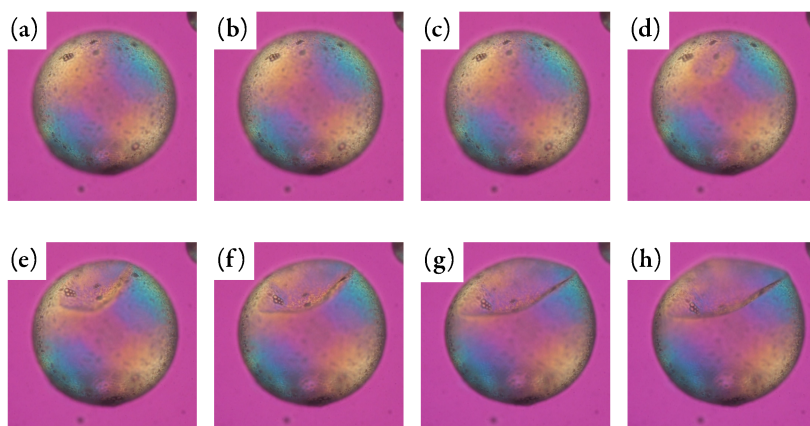


Figure 5.5: Thermal actuation of the homeotropic LCE shells. (a) 40 °C, (b) 45 °C, (c) 50 °C, (d) 55 °C, (e) 60 °C, (f) 65 °C, (g) 70 °C, and (h) 75 °C. Polarized micrographs were taken using a first-order λ plate.

the same PVA-glycerol-water solution in its core, and this was placed on a hotstage on the microscope. Due to the slightly lower density of the LCE compared to the aqueous solutions, the shell rose to the top of the capillary, where they stayed in place. The actuation process was monitored by polarized optical microscopy (Figure 5.5). Upon heating the shells from room temperature up to 50 °C, no change in size or shape was observed. At 55 °C a clear dimple was formed on the surface of the shell and upon further heating, the dimple increased in size. Cooling down to room temperature resulted in the disappearance of the dimple again. This process could be repeated many times without any fatigue. Remarkably, the dimple was formed always at the same location on the shell. From previous studies it was found that due to the density difference between the middle fluid and both inner and outer fluid, there is a displacement of the inner volume, causing an inhomogeneous shell thickness. At a thinner part of the shell it is expected to buckle earlier, biasing the position where the dimple is formed. Similarly to the LCE films, there was only a slight decrease in birefringence over the temperature range at which the actuation was performed (40 °C–75 °C), indicating that only a slight reduction of the molecular order takes place. Heating the shells further to temperatures higher than approximately 85 °C resulted in further growth of the dimple, subsequently, leading to the formation of a sharp fold where the shell wall irreversibly stuck together. Qualitatively, the actuation behavior observed for the shells is in agreement with the deformation re-

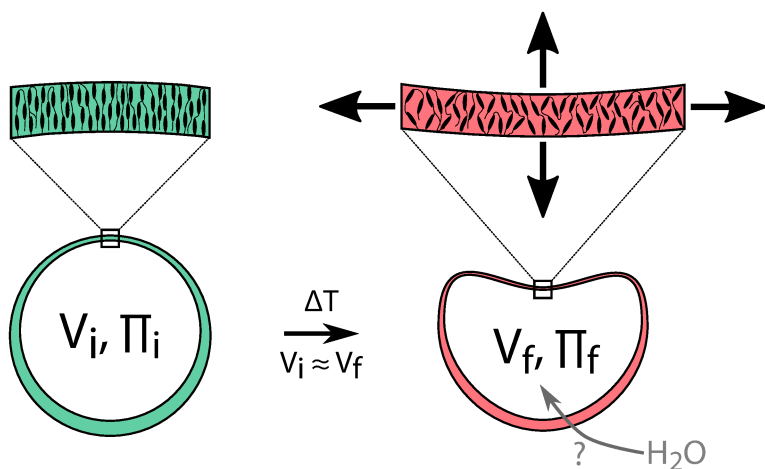


Figure 5.6: *The proposed mechanism for the actuation.*

ported above for thin films. Upon heating, the order of the liquid crystalline moieties is reduced, causing an expansion perpendicular to the director and a contraction perpendicular to the director as depicted in Figure 5.2b. This anisotropic shape change leads in case of a three dimensional homeotropic LCE shell, to an increase of the shell surface area, and thus the diameter. The shell thickness is expected to decrease. Since the fluid inside the shell expands significantly less than the internal volume by the thermal actuation, a dimple is formed to accommodate the excess surface area, as depicted in Figure 5.6. Knowing that the shells are semipermeable, and assuming that the osmotic pressure in the shell remains the same at equilibrium ($\Pi_i = \Pi_f$), an influx of water can be expected. However, no significant change in shell diameter is observed. It is anticipated that upon heating, the volume increase due to osmotic effects is lower (or slower) than the expansion of the shell surface hence the formation of a dimple (Figure 5.6).

5.3 Conclusion

In this chapter, the fabrication of thermal responsive semipermeable LCE shell actuators is presented. The production consists of a 2-step procedure where first a main-chain oligomer was prepared. In the second step shells were produced from the oligomers using microfluidics at room temperature. After solvent extraction, alignment, and photo-crosslinking homeotropic aligned LCE shells were obtained. The LCE shells show a typical anisotropic expansion when heated, resulting in an increase of the shell

surface area. Since the fluid inside the shell expanded significantly less, and the influx of water is significantly less than the increase of surface area of the shell itself, a dimple is formed to accommodate the excess surface area.

All things considered, these results indicate that LCE shells can potentially be used for the fabrication of *e.g.* micro pumps. Incorporation of pore-forming reactive mesogens like discussed in previous chapters of this thesis, can potentially lead to responsive semi-permeable shells for selective uptake & release or size and chemical selective catalytic reactions.

5.4 Experimental section

5.4.1 Materials

RM82 was obtained from Merck KGaA Germany. 3,6-dioxa-1,8-octanedithiol (DODT, 95%) was obtained from Sigma Aldrich. Triethylamine (TEA, 99%) was obtained from Acros. Irgacure 819 was obtained from Ciba Specialty Chemicals. All solvents used were Analytical Grade and obtained from Biosolve. 1.0 M HCl (aq.) was freshly prepared from a 37% HCl solution obtained from Sigma Aldrich. All reagents were used as received, without further purification.

5.4.2 Characterization

Magnetic nuclear resonance measurements were performed on a 400 MHz Agilent Technologies 400-MR NMR Spectrometer. Infrared spectroscopy was performed on a Varian 670IR FTIR spectrometer equipped with a transmission microscopy setup over a range of 4000–650 cm^{-1} with a spectral resolution of 4 cm^{-1} and 100 scans per spectrum. Polarized light microscopy was either performed on a Leica DM2700M Optical microscope equipped with polarization filters and a Linkam TMS 600 hot-stage or a Olympus BX-51 Optical microscope equipped with polarization filters and a λ -waveplate, the temperature controlled by a hot stage (Linkam T95-PE). Differential scanning calorimetry was performed on a TA Instruments Q1000 calorimeter. The samples were heated and cooled with 5 $^{\circ}\text{C min}^{-1}$ between -60°C (-90°C for LCEs) and 120°C with an isothermal equilibration of 3 minutes before each heating or cooling ramp. Dynamic mechanical analysis (DMTA), was performed on a TA instrument-Q800 instrument in a multi-frequency-strain mode at a frequency of 1 Hz.

5.4.3 Synthesis

Oligomer 1

The oligomer was prepared using the methods described by Yakacki *et al.* and Gelebart *et al.* [11, 12] 0.88 mL 3,6-dioxo-1,8-octanedithiol (5.38 mmol, 1 eq.) and 4.02 g RM82 (5.97 mmol, 1,1 eq) were dissolved in 50 mL DCM. 3,75 mL (26.89 mmol, 5 eq.) triethylamine was added to the solution under continuous stirring. The reaction mixture was heated to 35 °C and reacted for 16 hours. After, the reaction mixture was washed 3 times using 1 M HCl and subsequently dried over MgSO₄. ~2 mg BHT was added to the solution before it was concentrated by rotary evaporation, yielding 4,87 gram (97.4 %) oligomer 1. ¹H-NMR (399 MHz, CDCl₃) δ(ppm): 8.15 (dd, *J* = 10.5, 8.8 Hz), 7.21 – 7.04 (m), 7.01 – 6.93 (m), 6.41 (dd, *J* = 17.3, 1.5 Hz), 6.13 (dd, *J* = 17.3, 10.4 Hz), 5.82 (dd, *J* = 10.4, 1.5 Hz), 4.19 (t, *J* = 6.6 Hz), 4.12 (t, *J* = 6.6 Hz), 4.08 – 4.01 (m), 3.69 – 3.59 (m), 2.83 (t, *J* = 7.3 Hz), 2.74 (t, *J* = 6.8 Hz), 2.62 (t, *J* = 7.3 Hz), 2.24 (s), 1.84 (p, *J* = 6.4 Hz), 1.69 (p, *J* = 6.9 Hz), 1.59 – 1.35 (m).

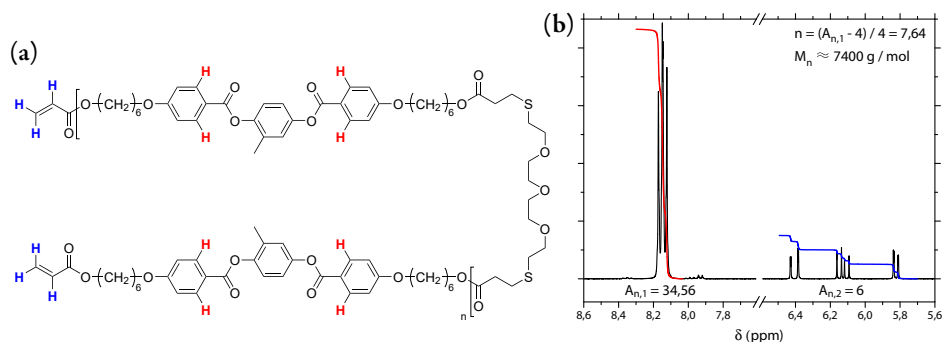


Figure 5.7: ¹H NMR of oligomer 1. (a) Chemical structure of the oligomer with the protons highlighted for the M_n calculation. (b) ¹H NMR spectrum of oligomer 1 showing the peaks from the acrylic end-groups (blue) and the aromatic protons from the mesogenic core (red). The integration of the acrylic groups was set to 6, to match the number of protons on the acrylic end groups.

The number average molecular weight of the oligomer was calculated using the following equations:

$$n = \frac{A_{n,1} - 4 \text{ protons}}{4 \text{ protons}} = 7.64 \quad (5.1)$$

$$M_n = 885.07 \times n + 672.77 = 7434 \text{ g mol}^{-1} \quad (5.2)$$

5.4.4 Methods

Fabrication of the microfluidic device

Fabrication of the microfluidic devices was performed at the University of Luxembourg. The cylindrical capillaries were tapered by a micropipette puller (P-100, Sutter Instrument) and then cut and flame polished using a Micro Forge (Narishige, MF - 900), allowing to set the orifice diameter at 80 μm and 300 μm for the injection and collection capillaries, respectively. Injection capillary is treated with DMOAP (N,N-dimethyl-N-octadecyl-3-aminopropyl-trimethoxysilyl chloride) and the collection capillary and square channel are treated with MAP (N-methyl-3-aminopropyltrimethoxysilane) to avoid LCE precursor wetting the collection and square capillaries.

Shell production

The three fluids (inner and outer fluid: 5 wt% PVA in water/glycerol, middle fluid: 20 wt% oligomer and 0.1 wt% Irgacure 819 in DCM) were pumped using a microfluidic flow control system (Fluigent MFCS-EZ) to different channels. The applied pressures varied from 20 to 200 μbar . The shell production was conducted at room temperature. A high speed camera (NX4-S3, Integrated Design Tools, USA) coupled to an inverted microscope (TS100, Nikon) allowed optical monitoring of the production process. The double emulsion was collected into 2 mL flasks containing 5 wt% PVA in water/glycerol. After collecting the solvent was replaced 3 times to remove residual DCM.

By annealing the solution containing the shells at 55 °C overnight, alignment was obtained. Subsequently, photo-crosslinking was performed at the same temperature using a UVATA LED UV curing system at 365 nm.

5.5 References

- [1] R. J. R. W. Peters, M. Marguet, S. Marais, M. W. Fraaije, J. C. M. van Hest, S. Lecommandoux, *Angew. Chem.* **2014**, *126*, 150–154.
- [2] B. M. Discher, Y.-Y. Won, D. S. Ege, J. C.-M. Lee, F. S. Bates, D. E. Discher, D. A. Hammer, *Science* **1999**, *284*, 1143–1146.
- [3] J. Noh, H.-L. Liang, I. Drevensek-Olenik, J. P. F. Lagerwall, *J. Mater. Chem. C* **2014**, *2*, 806–810.
- [4] Y. Geng, J. Noh, I. Drevensek-Olenik, R. Rupp, G. Lenzini, J. P. F. Lagerwall, *Sci. Rep.* **2016**, *6*, DOI 10.1038/srep26840.
- [5] D. J. Mulder, A. P. H. J. Schenning, C. W. M. Bastiaansen, *J. Mater. Chem. C* **2014**, *2*, 6695–6705.

- [6] E.-K. Fleischmann, H.-L. Liang, N. Kapernaum, F. Giesselmann, J. Lagerwall, R. Zentel, *Nat. Commun.* **2012**, *3*, 1178.
- [7] C. Ohm, N. Kapernaum, D. Nonnenmacher, F. Giesselmann, C. Serra, R. Zentel, *J. Am. Chem. Soc.* **2011**, *133*, 5305–5311.
- [8] J. Noh, B. Henx, J. P. F. Lagerwall, *Adv. Mater.* **2016**, *28*, 10170–10174.
- [9] E.-K. Fleischmann, H.-L. Liang, J. Lagerwall, R. Zentel in, *Vol. 8279*, **2012**.
- [10] S.-Y. Park, M.-H. Park, *Langmuir* **2007**, *23*, 6788–6795.
- [11] C. M. Yakacki, M. Saed, D. P. Nair, T. Gong, S. M. Reed, C. N. Bowman, *RSC Adv.* **2015**, *5*, 18997–19001.
- [12] A. H. Gelebart, M. Mc Bride, A. P. H. J. Schenning, C. N. Bowman, D. J. Broer, *Adv. Funct. Mater.* **2016**, *26*, 5322–5327.
- [13] H.-L. Liang, R. Zentel, P. Rudquist, J. Lagerwall, *Soft Matter* **2012**, *8*, 5443–5450.
- [14] P. E. Cladis, S. Torza, *J. Appl. Phys.* **1975**, *46*, 584–599.
- [15] H. Kim, J. M. Boothby, S. Ramachandran, C. D. Lee, T. H. Ware, *Macromolecules* **2017**, *50*, 4267–4275.
- [16] R. A. M. Hikmet, D. J. Broer, *Polymer* **1991**, *32*, 1627–1632.
- [17] A. S. Utada, E. Lorenceau, D. R. Link, P. D. Kaplan, H. A. Stone, D. A. Weitz, *Science* **2005**, *308*, 537–541.

Chapter 6

Technology assessment

6.1 Introduction

The self-assembly of liquid crystal monomers has proven itself as a powerful tool for the fabrication of well-defined nanoporous polymers. The work described in this thesis shows that porosity can be obtained in various ways of which hydrogen bonded mesogens and dynamic covalent chemistry are two promising strategies. Furthermore, light was shed on the chemical versatility and fabrication of new geometries of nanoporous liquid crystalline polymers. These findings open doors to new potential applications such as proton conduction membranes, ion exchange resins, and nanoreactors. However, in the current state, the materials need to be further improved in order to find their place in real-life applications. In this chapter, two critical points are highlighted and potential solutions are discussed.

6.2 Structure and rigidity

The fabricated nanoporous materials are relatively soft, causing a partial loss of order and rigidity after porosity is obtained. This reduced order often goes paired with dimensional changes of the polymer film due to pore collapse or swelling (Figure 6.1d–f), leading to less-defined pores.[1, 2]

Previously, two main approaches were presented to overcome this problem as depicted in Figure 6.1.[2] In the first approach (*i*) the concentration of the liquid crystalline crosslinker in the smectic LCN was increased. This resulted in reduced order loss and increased the materials rigidity after opening of the pores, but on the other hand, the porosity was affected and the number of binding sites inside the pores was reduced substantially. Consequently, size selectivity was obtained but the rate of adsorption was reduced. The second approach (*ii*) involves the addition of a small aliphatic di- or triacrylate. This crosslinking monomer is small enough to not bridge the smectic layers and therefore only will form crosslinks within the smectic planes (orthogonal to \mathbf{n}). In this way, the binding sites are affected in a lesser extent while the smectic structure is maintained after opening of the pores. Since this “in-plane” crosslinking monomer is not liquid crystalline, it could only be added up to a concentration 8 wt%. When larger amounts were added, poor alignment and phase separation occurred. Furthermore, the addition of 8 wt% of this intralayer crosslinker did not lead to size selective adsorption. This latter is mainly attributed to the concentration of the liquid crystalline (interlayer) crosslinker,

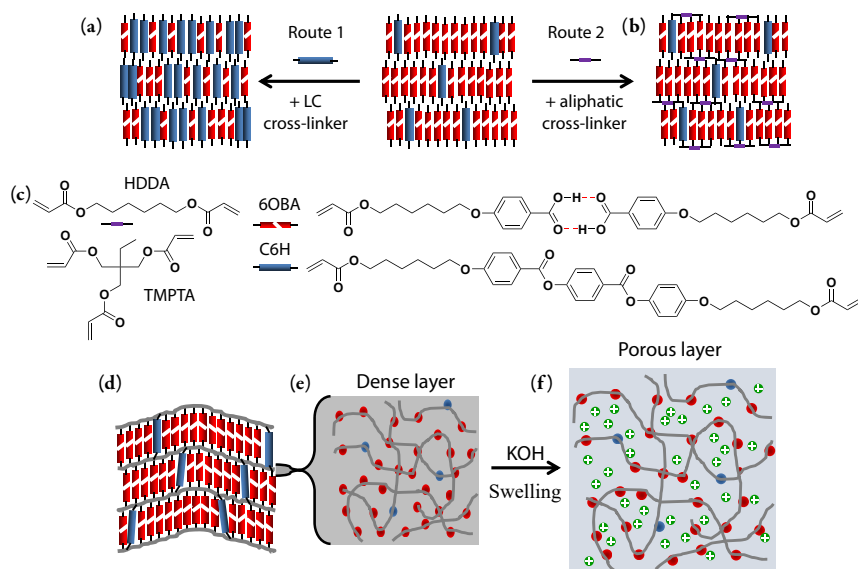
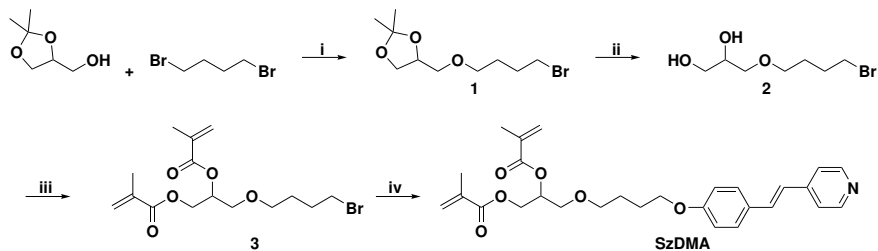


Figure 6.1: Improved rigidity and retained structure by crosslinking (a,b) Two routes to improve the materials properties; 1) increase the LC crosslinker density, 2) addition of a small aliphatic crosslinker. (c) Chemical structures of the monomers. (d) Side view of the smectic planes after photopolymerization. (e) Top view of a smectic plane after photopolymerization. (f) Top view of a smectic plane after pore formation at low cross-link density and absence of aliphatic crosslinker. Swelling occurs orthogonal to \mathbf{n} and additional pores are formed. Adapted from reference [3].

that was kept low, still allowing the material to swell significantly.[2]

It is anticipated that by combining the two approaches, and the design of a new “in-plane” crosslinking liquid crystal monomer (SzDMA, Scheme 6.1), having two methacrylate moieties, will increase both the structural and mechanical integrity of the porous polymers while improving the size selectivity. Since this new “in-plane” crosslinking monomer is liquid crystalline, it is expected that this compound can be present in a high concentration without disrupting the molecular organization. A proposed synthesis route is presented in Scheme 6.1. In the first step ether **1** is formed from 1,4-dibromobutane and 1,2-Isopropylidenediglycerol using phase transfer catalysis. By stirring the product in the presence of water and an acidic ion exchange resin (*e.g.* Amberlyst® 15 or Dowex® 50), the acetonide can quantitatively be hydrolysed to the corresponding diol (**2**, step *ii*). Subsequently, dimethacrylate **3** can be prepared by reacting **2** with two equivalents of methacryloyl chloride in presence of triethylamine in dichloromethane. Finally, by Williamson ether synthesis the intralayer crosslinking liquid crystal can be obtained. In this

last step, the use of cesium carbonate (Cs_2CO_3) in dry DMF at room temperature is preferred over the traditional methods (*e.g.* Na_2CO_3 in acetone or 2-butanone at elevated temperature) to prevent addition reactions to the nitrogen of the pyridine.



Scheme 6.1: *Synthesis of SzDMA* i) Bu_4NBr , NaOH , water/hexane, r.t. 24h, yield: 52 %. ii) Amberlyst® 15, 10 eq. water, DCM, r.t. 24h, yield: 97 %. iii) methacryloyl chloride, TEA, DCM, 0 °C–r.t. 16h, yield: 49 %. iv) 4'-hydroxy-4-stilbazole, 3eq. Cs_2CO_3 , 4 Å molecular sieves, DMF, r.t. 24h.

Furthermore, for the use in certain applications, a chemically robust polymer materials are desired. To date, all reactive smectic liquid crystals that have been used to prepare nanoporous polymers contain ester bonds. These bonds can either be present in the core of the mesogen or in their reactive tails. When the polymeric material is exposed to harsh conditions such as high temperatures or basic or acidic conditions, the ester bonds can be hydrolyzed. By using vinyl(ether), epoxy, or oxetane monomers a more chemically robust polymer backbone can be obtained. These type of reactive groups can be polymerized via a cationic polymerization mechanism. It has been shown that, compared to acrylates, cationic ring-opening polymerization show less polymerization shrinkage and are less sensitive to oxygen inhibition.[4]

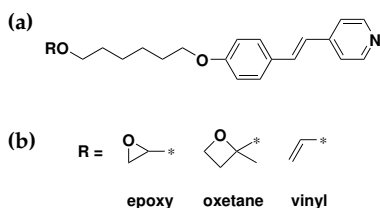


Figure 6.2: *Chemical structure of a more chemically resistant monomer. (a) The mesogenic core. (b) Different reactive end-groups: Epoxy, oxetane, and vinyl(ether).*

6.3 Scalability and geometry

With the view on an improved scalability and enhanced performance small smectic nanoporous LCN particles have been prepared by suspension photopolymerization.[3] The mesogens in the obtained particles had a radial configuration causing the smectic lamellae, and thus the pores, to have a concentric orientation. Nonetheless, adsorption could still take place since the particles were able to swell (Figure 6.3). But as discussed above, to enhance the selectivity and reduce the swelling of the porous materials, the cross-link density of the networks should be increased. Indeed, the latter will have an impact on the performance of the nanoporous LCN particles having pores oriented orthogonal to the surface. To overcome this problem, the orientation of the molecular director of monomers in the particles should be changed in such a way that pores are obtained on the surface.

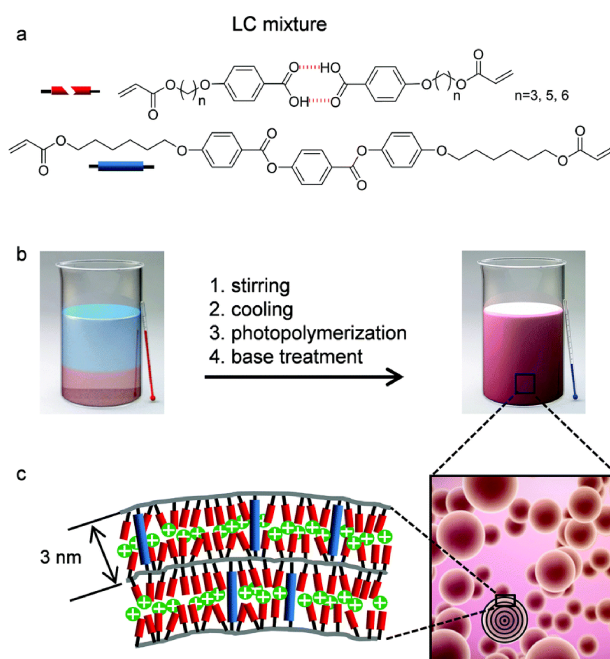


Figure 6.3: Chemical structure of a more chemically resistant monomer (a) LC monomer mixture containing 90 % H-bonded *n*OBA dimers in a 1:1 ratio and 10 % C6H cross-linker. (b) Fabrication scheme of the nanoporous polymer particles. A heterogeneous mixture of the aqueous phase and the LC mixture is homogenized in the nematic phase followed by cooling to the smectic mesophase. The smectic phase is photopolymerized and after a base treatment nanoporous polymer particles with onion-like order are obtained (c). Reproduced from van Kuringen et al.[2]

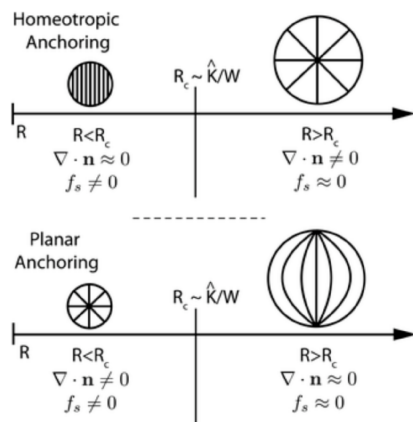


Figure 6.4: Schematic representation of the director configuration in nematic droplets. (top) At homeotropic anchoring conditions, decreasing the droplet size below a critical radius ($R_c \approx K/W$), a transition from a radial to a homogeneous director field is obtained. (bottom) For planar anchoring conditions, decreasing the droplet size induces a transition from a bipolar configuration to a radial director profile. Reproduced from Tomar et al. with permission of The Royal Society of Chemistry.[5]

The morphology of the liquid crystal monomer droplets before polymerization depends on the type of stabilization, size, and mesophase.[5] Generally, when the nematic liquid crystal droplets are stabilized by polymers in aqueous solution, the water at the interface promotes a planar alignment. Typically this leads to a bipolar configuration of the molecular director with two defects on the surface of the droplet. On the other hand, when stabilized using ionic surfactant, a homeotropic alignment is promoted, and a radial configuration of the director is obtained. Liquid crystals droplets have the peculiar properties that when their size is reduced, and the ratio surface area to volume is increased, the bulk properties become more dominant, and interfacial interactions diminish. There is a critical radius (R_c) where the director configuration of the droplets is either determined by the anchoring energy (W) or bulk elasticity (K) of the liquid crystal ($R_c = K/W$, Figure 6.4). So for larger nematic droplets ($R_c > K/W$), the configuration is mainly determined by the anchoring energy, where for smaller droplets ($R_c < K/W$) it is determined by the liquid crystals' elastic energy. For example, nematic droplets under homeotropic anchoring conditions changed configuration from radial to homogeneous with decreasing size. Interestingly, droplets exhibiting planar anchoring conditions change from a typical planar bipolar to a homeotropic radial configuration when their size is reduced.

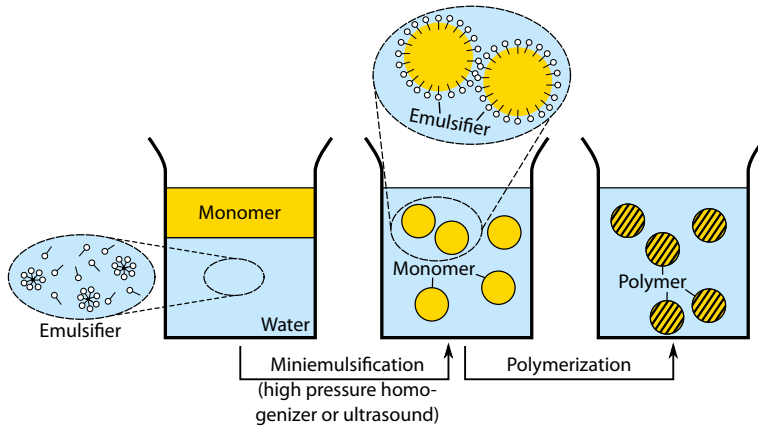


Figure 6.5: Overview of a miniemulsion polymerization.

Next to the size effects, changing from the nematic to the SmA mesophase gives rise to substantial changes of the elastic constants associated to the twist and bend deformations; K_2 and K_3 , while the splay elastic constant K_1 stays relatively unchanged. Twist and bend deformations of a smectic LC will lead to expansion or compression of the smectic planes, and therefore are energetically unfavorable. A splay deformation on the other hand, would only lead to a bend of the planes, and is therefore more favorable. As a result, initial planar bipolar nematic droplets change to a radial configuration after cooling down to the smectic mesophase.

Taking those considerations into account, it is anticipated that by making smaller smectic particles under homeotropic anchoring conditions, a homogeneous alignment can be obtained. This type of alignment will provide pores on the surface of the particles. However, the previously employed suspension technique does not provide the possibility to prepare particles of this size. Therefore, a miniemulsion technique is preferred instead.

Generally, in a (macro)emulsion polymerization, the reaction takes place in various intervals. In the first stage, a radical enters a monomer-swollen micelle. This radical initiates the polymerization and forms a propagating particle that is continuously fed with monomer from larger droplets. In a later stage, the larger monomer droplets start to deplete and the polymerization comes to an end. In a miniemulsion polymerization, on the other hand, the monomer is emulsified in small and stable droplets of 10–500 nm before polymerization. Because of their small size, and large surface area, most surfactant is

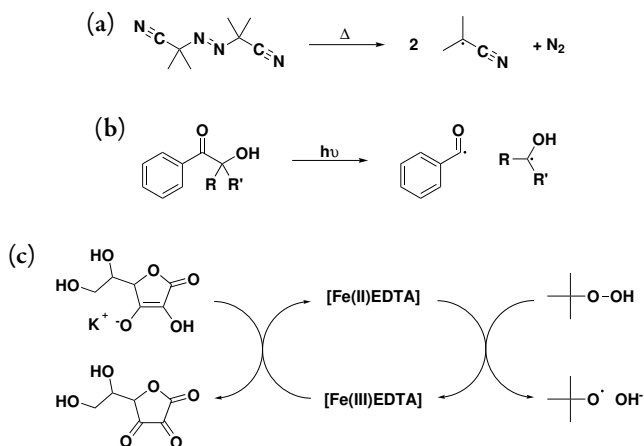


Figure 6.6: Initiation methods. (a) Thermal initiation using AIBN. (b) Photo initiation using a 2-Hydroxyacetophenone. (c) Iron mediated redox initiation of *tert*-butyl hydroperoxide using potassium ascorbate.

adsorbed on the droplets' surface. As a consequence, only a low concentration of free surfactant is present in the water phase, and therefore micelles are absent. Consequently, the initiation will take place by entry of a radical into the monomer droplets. In the ideal case, there is limited or no mass transport of monomer through the continuous phase, and every droplet can be considered a nanoreactor.

Typically, (mini)emulsion polymerizations are initiated using thermal free radical initiators. The rate of radical formation of thermal initiators is highly dependent on the temperature at which the reaction is performed (Figure 6.6a). Since liquid crystals are temperature sensitive compounds, this type of initiation is often impractical. For the fabrication of polymer films, for example, this problem is circumvented by the use of a photoinitiator (Figure 6.6b). In this way, the polymerization can remotely be started even at lower temperatures. For miniemulsion polymerizations, an appealing method is redox-initiation.[6–8] In the example depicted in Figure 6.6c, *tert*-butyl hydroperoxide was reductively dissociated using ferrous (Fe^{2+}) EDTA. The addition of potassium ascorbate leads to the regeneration of Fe^{2+} from Fe^{3+} , allowing the concentration of metal complex to be kept low. Using this approach, the polymerization can be performed isothermally and at a low temperature. Furthermore, the rate of radical formation can be controlled by the addition speed of the potassium ascorbate solution to the emulsion.

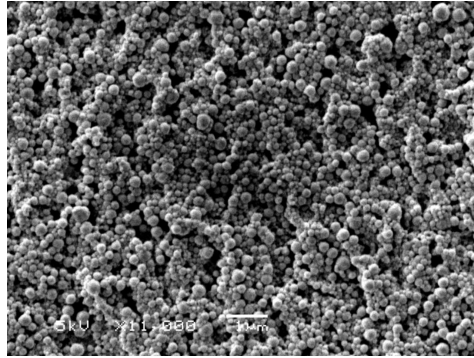


Figure 6.7: Obtained LCN particles from a redox initiated miniemulsion polymerization.

All things considered, by using a redox-initiated miniemulsion polymerization of reactive (smectic) liquid crystals, potentially small nanoporous LCN particles can be obtained having a radius $R_c < K/W$. These particles will ideally have a homogeneous director configuration, and thus pores on the surface of the particles. Preliminary experiments revealed that it is possible to prepare small LCN particles with an average diameter of approximately 200 nm using the same monomer mixture as Kuringen *et al.* (Figure 6.7).[3]

6.4 Conclusion

Liquid crystalline monomers show great potential for the fabrication of nanoporous polymers. In the academic field they are finding their place in a continually increasing number applications. However, towards industrial applications, they still struggle to compete with existing technology. This chapter addressed a number of critical points and potential solutions were discussed. After improvement of the rigidity, retention of structure, and chemical resistance, LC based nanoporous polymers will make a step forward towards commercial applications.

6.5 References

- [1] I. K. Shishmanova, C. W. M. Bastiaansen, A. P. H. J. Schenning, D. J. Broer, **2012**, *48*, 4555–4557.
- [2] H. P. C. van Kuringen, PhD Thesis, Technische Universiteit Eindhoven, Eindhoven, The Netherlands, **2016**, 140 pp.
- [3] H. P. C. van Kuringen, D. J. Mulder, E. Beltran, D. J. Broer, A. P. H. J. Schenning, **2016**, *7*, 4712–4716.
- [4] J. Lub, V. Recaj, L. Puig, P. Forcén, C. Luengo, *Liq. Cryst.* **2004**, *31*, 1627–1637.

- [5] V. Tomar, S. I. Hernández, N. L. Abbott, J. P. Hernández-Ortiz, J. J. de Pablo, *Soft Matter* **2012**, *8*, 8679–8689.
- [6] S. Wang, E. S. Daniels, E. D. Sudol, A. Klein, M. S. El-Aasser, *J. Appl. Polym. Sci.* **2016**, *133*, n/a–n/a.
- [7] N. Kohut-Svelko, R. Pirri, J. M. Asua, J. R. Leiza, *J. Polym. Sci. A Polym. Chem.* **2009**, *47*, 2917–2927.
- [8] Z.-g. Liu, Y. Han, C. Zhou, M.-y. Zhang, W.-m. Li, H.-x. Zhang, F.-q. Liu, W.-J. Liu, *Ind. Eng. Chem. Res.* **2010**, *49*, 7152–7158.

Summary

This thesis describes the development of new nanoporous liquid crystalline networks (LCNs) that are prepared from smectic liquid crystalline monomers. The use of liquid crystalline monomers leads to an unprecedented control of the size, the morphology, and the chemistry of nano-sized pores. This control makes this kind of material of interest for *e.g.* filtration, ion-exchange, adsorption, catalysis, and proton-conduction. Previously, nanoporous polymers based on smectic liquid crystalline networks have been prepared. The reactive mesogens that were typically used had a hydrogen-bonded benzoic acid derivatives core that, after the fabrication of the polymer networks, can be deprotonated to obtain anionic binding sites. The chemistry of the negatively charged nanopores in this system is, however, restricted to a basic environment. The post modification of the pore chemistry and other geometries rather than films have hardly been addressed. The work presented in this dissertation presents new approaches to obtain porous LCNs exhibiting new pore chemistries, applications, and shapes. Furthermore, this research illustrates the chemical versatility of liquid crystalline networks to obtain desired properties and new possible applications.

Dynamic covalent chemistry is an excellent tool to introduce chemical adjustability to nanoporous LCNs. Dynamic covalent bonds can form, break, and exchange under influence of a stimulus. In Chapter 2, a liquid crystalline monomer mixture containing a bisimine monomer is used to fabricate a smectic LCN. By hydrolysis of the imine bonds, an aldehyde functional pore is obtained that subsequently was post modified using a variety of amines to tune the size and polarity of the nanochannels. Selective adsorptive properties of different interiors have been compared in a later stage. These findings give great opportunity to access, in an easy way, the fabrication of polymer materials with chemical and size adjustable pores.

In Chapter 3 the fabrication of a nanoporous LCN with a basic pyridyl interior is presented. The material was prepared using hydrogen-bonded hetero dimers of which one part is a monomeric stilbazole unit and the other part a non-reactive benzoic acid derivative. After fabrication of the aligned polymer material and the subsequent removal of

the non-reactive part, a nanoporous liquid crystalline network is obtained with a basic pyridyl pore surface. A diacrylic crosslinker was added to ensure mechanical and structural integrity of the porous material after removal of the benzoic acid porogen. The influence of the crosslink density was investigated in detail. This basic pore interior can interact with various inorganic and organic acids leading to a cationic pore surface and a mobile anionic counter ion. By infiltrating phosphoric acid in the lamellar pores, proton conducting channels were obtained. The effect of loading and the pore orientation were studied. When an excess of phosphoric acid is present in the lamellae, the highest proton conductivity was obtained. While, when a stoichiometric amount of phosphoric acid was used, the highest anisotropic proton conduction was obtained.

The lamellar structure of the porous LCN containing a basic stilbazole pore surface can potentially be used as a nanoreactor in which inorganic nanoparticles can be synthesized. In Chapter 4, the infiltration and reduction of auric chloride inside the lamellar pores was studied. Auric chloride is a well-known precursor for the synthesis of gold nanoparticles. Acidic gold precursor binds strongly to the basic stilbazole interior forming small ionic clusters that are arranged in lamellae. By exposing the auric chloride infiltrated films to a sodium borohydride solution, gold nanoparticles were fabricated. The formation of the particles was studied by spectroscopy and microscopy techniques and a mechanism was postulated.

Responsive porous polymeric vesicles that change their properties upon an external trigger are of great interest in, for instance, the field medicine or heterogeneous catalysis. In Chapter 5, other geometries were explored by fabrication of elastomeric polymer shells is presented. The liquid crystal elastomer (LCE) shells were prepared from oligomeric liquid crystalline diacrylates by glass capillary microfluidics. After solvent extraction, alignment, and photo-crosslinking, homeotropic aligned LCE shells were obtained. The thermal properties of LCE in both free standing films and shells was studied. The LCE shells show a typical anisotropic expansion when heated. Because of the homeotropic alignment of the mesogens in the shell, an increase of the shell surface area is observed. Since the fluid inside the shell expanded significantly less than the shell itself, a dimple is formed to accommodate the excess surface area. The obtained thermal actuation might potentially be used as *e.g.* micropumps.

The possibilities of nanoporous LCNs is inexhaustible. However, there are many hurdles to be taken to reach any commercialization. In Chapter 6, the current limitations and possible solutions are discussed.

The overall research open new doors to the field of porous polymers where the versatility of the system and the dynamic character of the bonds make the system appealing for industrial use. Not to be neglected, this work put in perspective the multi usage of smectic nanoporous material. By looking at the pores created as nanoreactor or as catalytic sites, but also by moving away from conventional geometries of LC network, it is shown that the concept of LC-based polymers offer almost infinite possibilities.

Acknowledgements

Aan alle goede dingen komt een einde. Zo ook aan deze 4 geweldige jaren promotieonderzoek. Ik zou graag iedereen willen bedanken die, op welke manier dan ook, mij de afgelopen vier jaar heeft geholpen of ondersteund. Want het tot stand komen van dit proefschrift heeft niet kunnen geschieden zonder de hulp en steun van velen.

Als allereerste wil ik **Albert** bedanken voor het mogelijk maken dat ik mijn promotieonderzoek binnen de SFD-groep heb kunnen uitvoeren. Ik ben onder de indruk hoe de groep zich de afgelopen jaren heeft ontwikkeld onder jouw supervisie. Jouw enthousiasme en drive is besmettelijk, en je zal nog vele jonge onderzoekers aansteken. Onze tweewekelijkse meetings waren misschien niet altijd zo “tweewekelijkse”, desalniettemin, waren ze van ongekende waarde en had ik na iedere meeting weer een frisse blik en kon ik weer vooruit. **Dick** bedankt voor al je goede adviezen en je onuitputbare vloeibaar kristal kennis. Furthermore, I would like to thank **prof.dr. J.P.F Lagerwall, prof.dr. J.L. Serrano, dr. G. Portale, prof.dr.ir. D.C. Nijmeijer, and prof.dr. R.P. Sijbesma** for being part of my defense committee. Your advice, suggestions, and comments on my thesis were highly appreciated. **Michael**, thank you so much for helping me with the corrections of the chapters. **Tom en Marjolijn**, bedankt voor alle hulp de afgelopen jaren!

I would like to acknowledge all the people with whom I collaborated during by PhD research. **Huub**, ik wil je bedanken voor al de projecten waar we samen aan hebben gewerkt en de reizen die we hebben gemaakt... van de lange dagen in Grenoble, naar de witte kliffen van the Isle of Wight (nabij Southampton) en de hitte van Straatsburg. Het was altijd een plezier om met je samen te werken! Dear **Ting**, tingeling, it has been a year or so since you joined us, I really enjoyed working with you. I admire your energy and everlasting good spirits! Dear **Jan**, and the whole ESMP team, thank you for the collaborations we had and for the amazing time I had in Luxembourg. **JungHyun, Rao, and Kevin**, it was a pleasure working with you! **Giuseppe**, thank you for the great collaborations we had and helping me out with XRD issues! I would like to thank **Daniel** and **Giuseppe** for all the perfect support I had when I was at the DUBBLE beamline at the ESRF. Ghislaine, it was always really nice to work together and discuss science with you. I admire you gift to super-fast transform an idea into practice. **Tiny Verhoeven**, bedankt voor het helpen met de XPS-metingen! **Yifei**, thank you for helping me with the TEM measurements. I also would like to thank the students I have supervised. **Kim**, bedankt voor je inzet. Jouw resultaten gaven nieuwe inzichten die uiteindelijk hielpen tot de totstandkoming van hoofdstuk 3. **Bodine**, je hebt mij enorm geholpen met het ontwerp en syntheses van nieuwe reactieve vloeibare kristallen

die in het smectische vlak kunnen vernetten. **Marie**, also your achievements during your short internship were also of great value, merci.

I would like to thank the people from SFD and other groups, and visiting researchers, who made the past 4 years very pleasant during work and outside of it: **Alberto, Anping, Berry, Danqing, Davy, Ellen, Evelien, Fabian, Felix, Gilles, Ghislaine, Huub, Ivelina, Irén, Jeffrey, Jelle, Jeroen, Jurica, Koen, Laurens, Lihua, Marina, Marcos, Matthew (McBride), Matthew, My, Paul, Rob, Robert, Shaji, Stijn, Tom, Tim, Ties, Ting, Wei, Xiao, and Xiaohong**. Thank you! **Jody**, onze wetenschappelijke discussies waren altijd super waardevol en een bron van vele ideeën. Soms zeggen ze weleens: Beter een goede buur dan een verre vriend. Een goede buur én vriend zal je altijd blijven. Veel succes de komende maanden met afronden van je thesis! **Sander** en **Esther**, bedankt voor de vele diners, bike rides, en korte vakanties! Het was altijd enorm gezellig! **Hitesh** and **Monali**, the most welcoming people I have ever met. You guys made me a big fan of the Indian cuisine and culture! Thank you so much for inviting us to India and visiting you home town. It was amazing!

Ik wil mijn ouders bedanken voor alles steun afgelopen jaren. Iedere keer dat we op visite waren in Friesland was thuiskomen! **Heit** en **Mem** bedankt! **Alle, Bianca, Arnoud** en **Renske, Margaretha, Andries, Vera** en **Laura**, en **Doety, Ruurd** en **Jens**, ook bedankt voor jullie support en de vele fijne weekenden in Friesland.

Je voudrai aussi remercier **Jean Guillaume** et **Nicole**. Mis à part l'océan, les beaux étés Bretons et les hivers venteux, votre gentillesse et votre accueil ont fait de chaque visite des vacances géniales. **Jean Vincent, Laetitia, Marie Flavie** et **Anthony**, vous y avez aussi largement contribué, merci! Enfin, **Mathéo, Louane** et **Jade**, vous trois m'avez déjà conquis et j'attends chaque retour avec impatience pour pouvoir faire les fofous avec vous.

Of course, there is still one person who I did not thank yet. **Anne Hélène**, you have been so helpful and supporting at work and outside work. It truly were 4 wonderful years together and I am looking forward to the many many many years that will follow!

Curriculum Vitae

Dirk Jan Mulder was born on 22-02-1987 in Littenseradiel, the Netherlands. After finishing his preparatory middle-level vocational education in 2003 at the OSG Piter Jelles in Leeuwarden, the Netherlands, he started technical post-secondary college, at the Friesland College in Leeuwarden. In the last year of this study, he did two 5-month internships at Polymer Service Center Groningen (PSCG) and the Rijksuniversiteit Groningen on hybrid polymer synthesis and atom transfer radical polymerizations, respectively. In 2007 he started a bachelor in applied chemistry at the Van Hall Larenstein / Noordelijke Hogeschool Leeuwarden. In 2009 he did his graduated project within the laboratory of polymer chemistry at the Eindhoven University of Technology (TU/e) on the synthesis of thermoplastic poly(urethane/urea) elastomers from renewable resources via an isocyanate-free strategy, whereafter he studied molecular engineering (master) at the TU/e in Eindhoven, the Netherlands. In 2013 he graduated within the functional organic materials and devices group on the fabrication of chemical adjustable nanoporous polymers based on smectic liquid crystalline networks. The same year he started his PhD project in the same group under the supervision of Prof. Schenning. The main results are presented in this dissertation.

Publications

Publications related to this work

Fabrication and Post-Modification of Nanoporous Liquid Crystalline Networks via Dynamic Covalent Chemistry, D. J. Mulder, L. M. W. Scheres, D. J. Broer, A. P. H. J. Schenning *Chemistry of Materials* **2017**, 29(16), 6601–6605

Nanoporous smectic liquid crystalline polymers based on hydrogen bonded hetrodimers, D. J. Mulder, T. Liang, A. P. H. J. Schenning (in preparation)

Soft actuators based on liquid crystalline elastomer shells, V. S. R. Jampani*, D. J. Mulder*, K. Reguengo De Sousa, J. P. F. Lagerwall, A. P. H. J. Schenning (in Preparation)

Nanoporous polymers based on liquid crystalline monomers, Dirk Jan Mulder*, Jody A. M. Lugger*, Albert P. H. J. Schenning *Materials* **2018** (invited review, in preparation)

Publications related to this work but not included in this thesis

Photoresponsive nanoporous smectic liquid crystalline polymer networks: changing the number of binding sites and pore dimensions in polymer adsorbents by light H. P. C. van Kuringen, Z. J. W. A. Leijten, A. H. Gelebart, D. J. Mulder, G. Portale, D. J. Broer, A. P. H. J. Schenning, *Macromolecules* **2015** 48, 4073–4080

Nanoporous polymer particles made by suspension polymerization: spontaneous symmetry breaking in hydrogen bonded smectic liquid crystalline droplets and high adsorption characteristics, H. P. C. van Kuringen, D. J. Mulder, E. Beltran, D. J. Broer, A. P. H. J. Schenning, *Polymer Chemistry*, **2016** 7, 4712–4716

Smectic liquid crystal polymers as a template for ultrathin CaCO₃ nanolayers, Y. Xu, H. P. C. van Kuringen, D. J. Mulder, A. P. H. J. Schenning, N. A. J. M. Sommerdijk, *RSC Advances* **2016** 6, 13953–13956

Structural characterization of new fluorinated mesogens obtained through halogen-bond driven self-assembly. V. Kumar, D. J. Mulder, G. Cavallo, T. Pilati, G. Terraneo, G. Resnati, A. P. H. J. Schenning, P. Metrangolo, *Journal of Fluorine Chemistry* **2017**, 198, 54–60

On the Dimensional Control of 2D Hybrid Nanomaterials, A. Longo, D. J. Mulder, H. P. C. van Kuringen, D. Hermida-Merino, D. Banerjee, D. Dasgupta, I. K. Shishmanova, A. B. Spoelstra, D. J. Broer, A. P. H. J. Schenning, G. Portale *Chemistry – A European Journal* **2017**, *23*, 12534

Nanostructured membranes with adjustable rigidity, pore orientation and molecular order for adsorption and anhydrous proton conduction, T. Liang, H. P. C. van Kuringen, D. J. Mulder, D. J. Broer, A. P. H. J. Schenning, *ACS Appl. Mater. Interfaces*, **2017**, DOI: 10.1021/acsami.7b09386

Other publications

Well-defined Biobased Segmented Polyureas Synthesis via a TBD-catalyzed Isocyanate-free Route, D. Tang, D. J. Mulder, B. A. J. Noorder, C. E. Koning, *Macromolecular rapid communications* **2011**, *32*, 1379–1385

Chiral-nematic liquid crystals as one dimensional photonic materials in optical sensors, D. J. Mulder, A. P. H. J. Schenning, C. W. M. Bastiaansen, *Journal of Materials Chemistry C* **2014** *2*, 6695–6705

Making waves in a photoactive polymer film, A. H. Gelebart, D. J. Mulder, M. Varga, A. Konya, G. Vantomme, E.W. Meijer, R.L.B. Selinger, D. J. Broer, *Nature* **2017** *546*, 632–636

A Re-writable, Re-programmable, Dual Light-responsive Polymer Actuator. A. H. Gelebart*, D. J. Mulder*, A. P. H. J. Schenning, D. J. Broer *Angewandte Chemie International Edition* **2017**, DOI: 10.1002/anie.201706793

Photo-responsive sponge-like coating for on-demand liquid release, A. H. Gelebart, D. Liu, D. J. Mulder, K. H. J. Leunissen, J. van Gerven, A. P. H. J. Schenning, D. J. Broer (to be submitted)

Homeotropic Aligned Nanoporous Films Fabricated from Polymerizable Hydrogen bonded Hexagonal Columnar Discotic Liquid Crystals by Doping, J. A. M. Lugger, D. J. Mulder, Rint P. Sijbesma (to be submitted)